# Spontaneous parametric down-conversion sources for generation of atom-resonant quantum light

*Joanna A. Zielińska*
*thesis advisor: Prof. Dr. Morgan W. Mitchell*

*Dissertation*
*submitted for the degree of*
*Doctor of Philosophy*

ICFO - THE INSTITUTE OF PHOTONIC SCIENCES

26th January 2018

*Con el tiempo y un ganchito*

# Abstract

This thesis studies different designs of optical parametric oscillators as sources of atom-resonant quantum light at the rubidium $D_1$ line. We analyze the mode structure and present a technique for degenerate mode filtering in a conventional OPO based on a crystal inside a ring cavity. Nexy, we study in detail a first fully-tunable design of a monolithic doubly-resonant OPO.

The first part of this thesis presents the study of a multimode optical parametric oscillator from the theoretical point of view, calculating a multimode Bogoliubov transformation and a time-domain intensity correlation function of the output light. Next, we experimentally observe signatures of multi- and singlemode OPO output in pairwise time-of-arrival correlations of the generated photons, achieved thanks to Faraday anomalous dispersion filtering technique based on optical properties of atomic vapor in magnetic field.

The second, more extensive part of the thesis features a study of a new design of the OPO, a monolithic cavity (crystal polished and coated so that it forms a cavity) that allows full tunability even in a multiply-resonant configuration. The architecture we propose combines the advantages of a conventional ring cavity based OPO, with robustness, low-maintenance, compactness and stability characteristic of monolithic systems.

The tunability of the doubly-resonant monolithic OPO is realized by maintaining different sections of the crystal at different temperatures and pressing it with a piezoelectric actuator. The tuning method is tested when the system is employed as a second harmonic generator.

In addition, we describe a new nonlinear effect that comes into play when the monolithic cavity is pumped with 795 nm light. The phenomenon, that we call a *photo-Kerr* effect causes the cavity behavior resembling optical bistability due to Kerr nonlinearity, but with the magnitude (Kerr coefficient) dependent on the long-time average of intra-cavity power. The model we propose agrees well with the experimental results. The observed effect simplifies greatly the resonator stabilization, causing the cavity to maintain itself close to resonance even as the laser wavelength is changed by more than a free spectral range.

The thesis concludes with a study of suitability of the monolithic cavity affected by the photo-Kerr effect for squeezed light generation. We test the monolithic cavity as an OPO and demonstrate 1.6 dB of quadrature squeezing via homodyne detection.

# Resumen

Esta tesis estudia diferentes diseños de osciladores paramétricos (OPO, por sus signas en inglés) como fuentes de luz cuántica resonante con la línea $D_1$ de átomos de rubidio. Analizamos la estructura de modos y las técnicas de filtrado en un oscilador paramétrico convencional basado en un cristal no lineal dentro de una cavidad. También presentamos el primer diseño de un OPO monolítico con dos resonancias con frecuencias ajustables.

La primera parte de la tesis presenta el estudio de un oscilador paramétrico multimodo desde el punto de vista teórico, calculando una transformación de Bogoliubov multimodo y una función de correlación temporal de intensidad. A continuación, se observan experimentalmente las señales de la emisión de OPO multimodo o de un solo modo en correlaciones de tiempo de llegada de pares de los fotones generados, obtenidos gracias a la técnica de filtración de dispersión anómala de Faraday basada en las propiedades ópticas del vapor atómico en campo magnético.

La segunda y más extensa parte de la tesis presenta el estudio de un nuevo diseño del OPO: una cavidad monolítica (cristal pulido y recubierto de tal manera que forma una cavidad) que permite ajustar las frecuencias de resonancia, incluso en una configuración multi-resonante. La arquitectura que proponemos combina las ventajas de una OPO convencional basada en una cavidad afuera de cristal, con robustez, bajo mantenimiento, compacidad y estabilidad característica de los sistemas monolíticos.

La ajustibilidad del OPO monolítico con doble resonancia se realiza manteniendo diferentes secciones del cristal a diferentes temperaturas

y presionándolo con un elemento piezoeléctrico. El método de afinación es sometido a prueba cuando el sistema se emplea como generador de segundo armónico.

Además, describimos un nuevo efecto no lineal que entra en juego cuando la cavidad monolítica se bombea con luz 795 nm. El fenómeno que denominamos efecto *photo-Kerr* provoca que el comportamiento de la cavidad se asemeje a la biestabilidad óptica debido a la no linealidad de Kerr, pero con la magnitud (coeficiente de Kerr) dependiente del promedio de tiempo largo de la potencia de la luz dentro de la cavidad. El modelo numérico que proponemos coincide con los resultados experimentales. El efecto simplifica en gran medida la estabilización de la cavidad, haciendo que ésta se mantenga cerca de la resonancia incluso cuando la longitud de onda del láser cambia en más de la distancia entre dos resonancias consecutivas.

La tesis concluye estudiando la idoneidad de la cavidad monolítica con el efecto photo-Kerr para la generación de luz comprimida. Se emplea la cavidad monolítica como oscilador paramétrico, obteniendo luz comprimida y se demuestra 1.6 dB de squeezing mediante detección homodina.

# Acknowledgements

I would like to begin with expressing my deep gratitude and respect to my supervisor, Morgan Mitchell. I consider myself really lucky to learn from such a great scientist (I don't know how, but he was always right), counting on his patience and support in every situation.

Huge thanks are due to all the past and present members of the research group I had the pleasure to be a part of, particularly to my colleagues from the "Light Lab" (which probably needs a new name now). I owe thanks to Federica Beduini for being my companion during the hours of taking data in total darkness and Gianvito Lucivero for his great DJ skills, as well as to Ricardo Jimenez, with whom sharing the lab was always a pleasure, and to Florian Wolfgramm because although we did not coincide much, his well-built setups always remained an inspiration.

I am really grateful to our collaborators from KTH Stockholm, Carlota Canalias and Andrius Zukauskas for growing the RKTP crystals and sharing their knowledge about nonlinear materials on numerous ocasions. The help I received in the clean room from Alican Noyan and Johann Osmond is very much appreciated, as well as patient answers to all my questions about KTP provided by Fabian Steinlechner.

I would like to acknowledge the all the ICFO staff, who have always been friendly and helpful to me. I am grateful to Xavi and his team from mechanical workshop in particular, for building all the unusual and complex elements I needed with a smile. Without them I wouldn't stand a chance. Many thanks to Denis Guilhot for patiently guiding me through the complexities of patent-writing.

There's quite some people that made me feel at home at ICFO. I owe

thanks to Ferran, Roland, Gil and Pau for their sincere friendship, afternoon walks around the lake and food (and quality gossip) exchange group. Special thanks goes to Silvana for "adopting" me at the beginning and incessantly correcting my grammar. I would also like to acknowledge Naeimeh Behbood and Hara Troullinou for maintaining calm and positive atmosphere in the office 006. I had lot of fun working as a part of the YAO 2014 organising commitee thanks to Boris, Naeimeh, Giorgio, Emanuele, Gianvito and Daniel. Lastly, there are people who indirectly contributed to this thesis by maintaining its author happy outside the lab. To name a few, I owe thanks to to Pasqui, for her incredible energy, Marko and Bane for the laughs, to Khalil, for his advice "del barrio," to Bjoern for his hospitality in California and to Jaime (I still owe him one), Ana, Julien and Jordi together with his very catalan sailboat crew.

During four years I was supported by the FI-DGR PhD-fellowship program, for which I am sincerely grateful to the Generalitat of Catalonia and the Catalan citizens who funded my scholarship.

Of course, this work would not have been possible without moral support by my family. Thanks to messages, calls and frequent visits to Barcelona by my parents, Ewa and my sister Marta the two thousand kilometers separating me from home seemed like nothing.

I'm happy the last years, and the last months in particular, were everything but ordinary and predictable, and I owe Sergio thanks for these good times (and the well-written acknowledgements in his thesis that gave me something to look up to when writing this diffcult chapter).

# List of publications and patents

1. J. A. Zielińska, F. A. Beduini, N. Godbout, and M. W. Mitchell, *Ultranarrow Faraday rotation filter at the Rb $D_1$ line,* Optics Letters **37**, 524-526 (2012).
2. J. A. Zielińska, F. A. Beduini, V. G. Lucivero and M. W. Mitchell, *Atomic filtering for hybrid continuous-variable/discrete-variable quantum optics*, Optics Express **22**, 25307-25317 (2014).
3. F. A. Beduini, J. A. Zielińska, V. G. Lucivero, Y. A. de Icaza Astiz, and M. W. Mitchell, *Interferometric Measurement of the Biphoton Wave Function,* Physical Review Letters **113**, 183602 (2014).
4. J. A. Zielińska and M. W. Mitchell, *Theory of high gain cavity-enhanced spontaneous parametric down-conversion,* Physical Review A **90**, 063833 (2014).
5. F. A. Beduini, J. A. Zielińska, V. G. Lucivero, Y. A. de Icaza Astiz, and M. W. Mitchell, *Macroscopic Quantum State Analyzed Particle by Particle,* Physical Review Letters **114**, 120402 (2015).
6. J. A. Zielińska and M. W. Mitchell, *Monolithic frequency converter*, European patent application No.16382440.2-1556 (filing date 21/09/16), US patent applicaion No.151711,453 .
7. J. A. Zielińska, A. Zukauskas, C. Canalias, M. A. Noyan, and M. W. Mitchell, *Fully-resonant, tunable, monolithic frequency conversion as a coherent UVA source,* Optics Express **25**, 1142-1150 (2017).
8. J. A. Zielińska and M. W. Mitchell, *Self-tuning optical resonator* Optics Letters **42**, 5298-5301 (2017).
9. J. A. Zielińska and M. W. Mitchell, *Atom-resonant squeezed light from a tunable monolithic ppRKTP parametric amplifier* , accepted in Optics Letters

# Contents

# Chapter 1

# Introduction

The first optical parametric oscillator, in which an optical down-conversion process was resonantly enhanced by placing a $\chi^{(2)}$ medium inside an optical cavity was demonstrated at Bell Labs [1] in 1965, shortly after the invention of the laser. Optical parametric oscillators are used as coherent light sources for various purposes, as well as to generate non-classical light for quantum optics research.

The microscopic nature of the downconversion process, in which one pump photon produces two photons in signal and idler intracavity modes, underlies the quantum properties of the light generated by an OPO. The quantum correlations between the intensities of signal and idler fields, are manifest as a collective property of the emitted photons ("continuous-variable" regime) in the form of squeezing that can be exploited to reduce noise in metrology experiments. These quantum correlations also become evident as quantum entanglement of photon pairs extracted from the OPO output (in "discrete-variable" regime), which is a basic resource for quantum communication and quantum information science.

## OPOs in quantum optics

The first experiment involving squeezed light generated by spontaneous parametric down-conversion process in an OPO was demonstrated in 1986 [2], achieving almost 3 dB of noise reduction. However, since then the technique has come a long way, taking advantage of new nonlinear materials, better periodic poling techniques, low-loss coatings, and high quantum efficiency detectors. Squeezing is useful for sensing of delicate systems, because it offers an increase of the signal-to-noise ratio without increasing probe power, in order to, for example, reduce perturbation of quantum state of the probed system in atomic quantum metrology [3, 4, 5].

To date, the record 15 dB of squeezing (corresponding to factor of 32 in noise reduction) was reported in 2016 by Vahlbruch et. al. [6] at 1064 nm, with a view to feeding it to the interferometers of current gravitational wave observatories, which in the next upgrade are expected to have sensitivity enhanced by the application of the squeezing. An SPDC source that generated record squeezing before that, with 12.7 dB of noise reduction [7], was built as astep towards improving the future gravitational waves detectors as well.

Squeezed light from an OPO can, in principle, have noise reduced to arbitrarily low levels, but in practical scenarios, measurement scheme losses and readout noise are the limiting factors in the maximum achievable squeezing. Nevertheless, loss-tolerant quantum metrology schemes are also being developed, basing on correlated photon-number states generated by an SPDC source subject to photon-counting measurements [8].

Quantum entanglement of the photons in signal and idler modes was theoretically predicted in 1988 [9], only to be experimentally measured in a sub-threshold OPO four years later [10]. Since then, cavity-enhanced

spontaneous parametric down-conversion has been employed to make highly efficient photon pair sources [11] of interest for quantum networking with atomic quantum memories [12, 13].

Apart from that, SPDC sources in combination with coherent states have been proposed as extremely bright photon pair sources [14], as well as for generation of entangled multi-photon states [15, 16].

The applications of OPOs range from simple frequency converters to quantum simulators for Ising model [17], and each application requires an especially crafted system. However, in this thesis we mainly focus on selected aspects of OPOs optimized for interaction with atoms, which require high spectral brightness, precisely controlled wavelength, and narrow linewidths.

## Continuous/discrete variable regimes

Experimental and theoretical methods for studying quantum fields have traditionally been divided between the "continous-variable" and "discrete-variable" camps, each with distinct language and experimental techniques [18]. Recently this artificial division has begun to dissolve, and experiments combining continuous-variable and discrete-variable elements [19, 20, 21, 22] have proliferated. These hybrid methods create new possibilities, including optical entanglement between particle-like and wave-like states [22, 23], a form of micro-macro entanglement [24, 21] that puts to test conventional notions of the quantum/classical boundary.

Interfacing hybrid states to single atoms or atomic ensembles would further expand their power, offering synchronization in communications and computing protocols [25], quantum-enhanced probing of atomic sensors [3, 4], and tests of quantum non-locality with massive particles [26]. If optical hybrid states can be transferred to an atomic system, they can

be detected by quantum non-demolition measurement [27, 28, 29, 30, 31], allowing non-destructive characterization and repeated use. A major challenge for the interaction of non-classical states with atomic systems has been generating quantum light at the wavelengths and bandwidths of atomic transitions [32, 33, 34, 35]. The hybrid continuous-discrete variable approach offers still more challenges: the heralding process must be highly selective to avoid false heralding events, while the continuous-variable states must be protected against both dephasing and loss.

## High-gain CESPDC

In contemporary applications, there is a trend toward lower-finesse cavities in CESPDC [36]. The available single-pass gain has increased, due to periodically poled nonlinear materials and more powerful pump lasers, and lowering the finesse allows higher escape efficiencies at the same system gain level. At these lower finesses, the "tails" of the modes begin to overlap, and mode shapes deviate from the simple Lorentzian. At the same time, higher-gain applications, for example in generation of "Schrödinger kitten" [37] states and other highly non-classical time-domain states [23, 38, 39] by photon subtraction, are also becoming important. These higher-gain processes necessarily involve stimulated SPDC [40], in which a photon or a pair of photons induces the production of more pairs. These developments motivate the new calculation of CESPDC fields presented in chapter 3, beyond the low gain, single-longitudinal-mode, and high-finesse approximations.

## Monolithic cavities

A common approach to frequency conversion and squeezed light generation places a $\chi^{(2)}$ nonlinear medium, often a periodically poled crystal, within an external ring cavity that resonates the fundamental (pump) beam. The approach we start from in chapter 6, following [41] and [42], uses nonlinear crystals polished and coated to form a linear cavity, offering the advantages of stability, compactness and zero interface loss. The price for these advantages is the loss of tuning degrees of freedom available when using independent optical elements to define the cavity. To date, no demonstrated monolithic cavity has shown independent control of phase matching and double cavity resonance. In the case of [42], tuning the cavity compromising on the phase matching. Similarly, tunable double resonance (of the fundamental and second harmonic) has been demonstrated with external cavities but not yet with monolithic cavities. Both of these factors reduce the achievable conversion efficiency and motivate new approaches for tuning monolithic cavities. We present the design of a tunable doubly resonant monolithic device in Section 5.5, and subsequently experimentally show the concept works both when the device is employed as a frequency converter and as an squeezed light source.

## Thesis structure

This thesis is divided into two parts. First part is focused on theoretical analysis of the quantum properties of multimode light from cavity-enhanced spontaneous parametric down-conversion sources and an experimental method of filtering out only the degenerate mode using an atomic-vapour based filter. In the second part, we describe the monolithic tunable frequency converter, starting from the design, and followed by its

performance as a second harmonic generation device and as a squeezer (subthreshold OPO).

Part one "Multimode optical parametric oscillator" consists of three chapters. Chapter one contains general facts about second order nonlinear materials and an introductory description of spontaneous parametric down-conversion in a singlemode OPO, which later serves as a base to compare against the multimode case. Chapter two presents the properties of the quantum state calculated from first principles for a multimode OPO (published in [43]). In chapter three we describe an experiment in which such a multimode light emitted by the OPO is filtered with the use of a Faraday anomalous dispersion optical filter and the efficiency of the filtering procedure in selecting only the degenerate mode out of the multimode light is proven by the photon time-correlation measurements on the filtered and unfiltered OPO output (published in [44]).

Part two "Tunable monolithic frequency converter" consists of five chapters. Chapter four explains the concept of squeezed light and its utility for probing delicate systems, illustrating it on the example of the Faraday probing of the Bose Einstein condensate. Chapter five presents the design of the monolithic squeezed light source optimized for atomic physics applications. Chapter six describes experimental results on the tuning methods of the doubly resonant cavity as well as the second harmonic generation. Chapter seven describes a new nonlinear effect we observe in the monolithic RKTP crystal based cavities (the photo-Kerr effect). In chapter eight we experimentally test the monolithic device as an OPO and prove that it is useful for squeezed light generation.

# Chapter 2

# Optical Parametric Oscillator (OPO)

This chapter introduces basic concepts about optical parametric oscillators. We concentrate on the properties of nonlinear materials commonly used in the OPOs and explain the concept of quasi phase matching. Next, we outline how squeezing is generated in the $\chi^{(2)}$ material and how to calculate the output quantum state of light emitted by a single-mode OPO cavity.

The optical parametric oscillator is an optical resonator containing a $\chi^{(2)}$ nonlinear crystal. The resonator enhances a three-wave mixing process occurring in the crystal, which allows the conversion of input pump beam into "signal" and "idler" output beams. Although OPOs are a workhorse technique for frequency conversion that is useful for generating coherent light at wavelengths that are difficult to access via standard laser technologies, they are also remarkably effective as entangled or squeezed light sources in many quantum optics laboratories.

Cavity-enhanced conversion of pump into signal and idler occurring in the OPO is often referred to as "parametric downconversion". We talk about "degenerate" parametric downconversion when signal and idler are the same polarization and frequency (half of the frequency of the pump). Although degenerate OPO and a second harmonic generator can

be the same device (only with input and output reversed), there is a very important difference between these two processes, which has to do with the quantum state of the output. When pumped by a coherent beam, second harmonic generator will always give a coherent output state, whereas an OPO will give a squeezed output.

In this thesis we only consider OPOs pumped far below threshold. A threshold of an OPO is the pump power at which the system undergoes a critical point phase-transition [45], although it can yield non-classical light both below and above threshold [46]. This power limit is the minimum pump power for which signal (or idler) experiences more gain due to the downconversion than loss during the cavity roundtrip.

A subthreshold OPO is a very important tool in both discrete-variable and continuous-variable quantum optical experiments. It can generate correlated photon pairs consisting of one signal and one idler photon, that can be entangled in wavelength and/or polarization. Apart from that, OPOs are frequently used as sources of squeezed light, which take advantage of the fact that OPO can reduce the noise in one quadrature of the input field (at the cost of increasing it in the other), whether it is vacuum or a coherent state. In the case of coherent input in the signal/idler mode (a "seeded" OPO), the OPO acts like a phase sensitive amplifier, amplifying or deamplifying the seed power depending on the phase between seed and pump, which also determines for which quadrature the noise is amplified and for which it is deamplified. The output state of a seeded OPO is called a bright squeezed state. When the input is a vacuum state the OPO modifies its noise properties (according to the pump phase) to generate a "squeezed vacuum", an extremely important tool in quantum metrology. Throughout this thesis we sometimes refer to this case (an unseeded subthreshold OPO) as cavity-enhanced spontaneous parametric down-conversion (CESPDC) source.

## 2.1 Nonlinear medium

The second order nonlinear medium is the key element of an OPO. Second order nonlinearity (or $\chi^{(2)}$ nonlinearity) means that polarization of the material $\vec{P}$ induced by the electric field $\vec{E}$ is not proportional to the field, but also has a second order term

$$\vec{P} = \chi^{(1)}\vec{E} + \chi^{(2)}\vec{E}\vec{E} \equiv \chi^{(1)}\vec{E} + \vec{P}_{\mathrm{NL}} \tag{2.1}$$

where $\chi^{(1)}$ linear susceptibility is responsible for refractive index of the material $n = (1+\chi^{(1)})^{1/2}$. Second order nonlinearity can occur only in materials that do not show inversion symmetry i.e. noncentrosymmetric crystals, and vanishes identically is centrosymmetric crystals, amorphous solids, gases and liquids (although they display a $\chi^{(3)}$ nonlinearity) [47].

In general, taking into account a vector nature of the fields, second order susceptibility $\chi^{(2)}$ is a third rank tensor. Throughout this thesis we consider only the case when all beams, meaning pump, signal and idler, are of the same polarization (type-0 downconversion), so we treat $\chi^{(2)}$ as a scalar for simplicity.

We know from Maxwell equations that $E$ and $P$ evolve according to the following wave equation in the material [47]

$$\left(-\nabla^2 + \frac{n^2}{c^2}\partial_t^2\right)\vec{E} = -\frac{4\pi}{c^2}\partial_t^2\vec{P}_{\mathrm{NL}} \tag{2.2}$$

in which nonlinear response $P_{\mathrm{NL}}$ acts like driving term, causing the electric field at frequencies different from the input frequencies to appear. In the case of three wave mixing, $P$ gives source terms always when $\omega_{\mathrm{p}} = \omega_{\mathrm{s}} + \omega_{\mathrm{i}}$, where $\omega_{\mathrm{p}}$, $\omega_{\mathrm{s}}$ and $\omega_{\mathrm{i}}$ are respective pump, signal and idler frequencies. For example, if we apply an input electric field with nonzero components at two frequencies, second harmonic, sum and difference

frequencies generation is possible. However, there is one more condition that determines which frequencies, or whether any frequencies, can be produced.

When solving the equation (2.2) in simple case of sum frequency (SF) generation, where $E$ has frequency components at $\omega_\mathrm{s}$ and $\omega_\mathrm{i}$ and we generate $\omega_\mathrm{p} = \omega_\mathrm{s} + \omega_\mathrm{i}$, we find that the SF is generated most efficiently when

$$\vec{k}_\mathrm{p} = \vec{k}_\mathrm{s} + \vec{k}_\mathrm{i} \tag{2.3}$$

where $k_i = \frac{\omega_i}{c} n_i$ and $n_i$ are the respective refractive indices. The relation (2.3), which is a manifestation of conservation of momentum is known as the perfect phase matching condition. It means that generated wave is in phase with the nonlinear polarization and it can extract energy most efficiently from the incident light. Macroscopically, it means that fields emitted by dipoles constituting the material add coherently in forward direction. In practice, in presence of wavevector mismatch $\Delta k = k_\mathrm{s} + k_\mathrm{i} - k_\mathrm{p}$ the generated field amplitude oscillates, building up for the propagation length $L_C = \pi/\Delta k$ before it starts to decrease again [47].

There are several methods that allow us to ensure the condition (2.3) is fulfilled, for example taking advantage of the birefringence of the crystal. However, they require the fields involved in the three-wave mixing process to be non-collinear and/or polarized along different axes. In the case of the a colinear type-0 downconversion systems, which are the subject of this thesis, the appropriate method of avoiding momentum mismatch is the quasi phase-matching. This technique depends on periodic-poling of the material, that is inverting the orientation of one of the crystal axes periodically along the optical axis of the crystal with a period $\Lambda = 2L_C$ (or its odd multiple).

In the case of periodically poled material the phase matching condition

(2.3) is replaced by the quasi phase-matching condition

$$k_{\mathrm{p}} = k_{\mathrm{s}} + k_{\mathrm{i}} - m\frac{2\pi}{\Lambda} \tag{2.4}$$

where all wave-vectors are colinear, and $m$ is an odd integer. When the condition (2.4) is satisfied, the field grows monotonically with the length of interaction, although less rapidly than in case of perfect phase matching. The main drawback of the quasi phase matching is the technical difficulty in fabricating high-quality periodically poled crystals, in particular for wavelengths requiring short (few microns) poling periods. We return to this problem in chapter 6.

## 2.2 Squeezing in OPO cavity

As derived in many nonlinear optics textbooks, propagation of degenerate signal/idler field through a pumped, phase-matched $\chi^{(2)}$ medium is described by a linear transformation

$$\mathscr{E}(z) = \mathscr{E}(0)\cosh r + \mathscr{E}^{*}(0)\sinh r \tag{2.5}$$

where $r$ is the nonlinear coupling parameter proportional to the effective nonlinearity, pump power and length of the nonlinear medium.

In light of the unitary nature of parametric interactions, it is natural to assume the field operators similarly obey the Bogoliubov relation

$$a_{\mathrm{out}} = a_{\mathrm{in}}\cosh r + a_{\mathrm{in}}^{\dagger}\sinh r \tag{2.6}$$

which equivalently can be written as

$$a_{\mathrm{out}} = \hat{S}^{\dagger} a_{\mathrm{in}} \hat{S} \tag{2.7}$$

where $\hat{S} = e^{\frac{1}{2}(r(a^\dagger)^2 + r^* a^2)}$ is the squeeze operator and $r$ is squeezing amplitude.

For example, as a result of a spontaneous process (vacuum input) we obtain from a pumped nonlinear medium a quadrature-squeezed state:

$$\rho_{\mathrm{r}} = \hat{S}(r)|\mathrm{vac}\rangle\langle\mathrm{vac}|\hat{S}(r)^\dagger \tag{2.8}$$

Quadrature-squeezed means that for a certain quadrature operator:

$$q_\theta = \frac{1}{\sqrt{2}}(ae^{-i\theta} + a^\dagger e^{i\theta}) \tag{2.9}$$

the variance $\mathrm{var}(q_\theta) < 1/2$. Note that the Heisenberg uncertainty relation:

$$\mathrm{var}(q_\theta)\mathrm{var}(q_{\theta+\pi/2}) > 1/4 \tag{2.10}$$

requires that the variance of the orthogonal quadrature $q_{\theta+\pi/2}$ becomes anti-squeezed. For a coherent state (including the vacuum state) variances of both quadratures are independent of the phase and equal $1/2$.

Describing the squeezing transformation of the field occurring due to a $\chi^{(2)}$ medium inside of a cavity is a far more complex task. The quantum optical approach used in this thesis is based on so-called input-output relations, introduced by Collett and Gardiner in [48] to describe squeezing effects in OPOs. A basic challenge for the theoretical description of such systems is the interface between the cavity mode $a_0$ with its discrete frequency $\omega$ and the broadband field outside the cavity, which are connected by a partially-transparent mirror. Collett and Gardiner showed that, after making a Markoff approximation for the external fields, the dynamics of the cavity mode can be described as

$$\frac{d}{dt}a_0 = -i\omega a_0 + r a_0^\dagger e^{-i\omega_p t} - \frac{\Gamma}{2}a_0 + \sqrt{\Gamma}a_{in} \tag{2.11}$$

where $r$ is nonlinear coupling coefficient $\omega_p$ is pump frequency and $\Gamma = T\delta\omega$, with $T$ the being mirror transmission and $\delta\omega$ the cavity free spectral range (FSR). The output field $a_{\text{out}}$ is related to the input $a_{\text{in}}$ and cavity fields by

$$a_0 = (a_{in} + a_{out})/\sqrt{\Gamma} \tag{2.12}$$

Equations similar to Eq. (2.11) are of great utility in computing the properties of the quantum fields. Because they are linear, they can be solved algebraically in the Fourier domain.

Solving the Eq. (2.11) we arrive to Bogoliubov transformation in the form of Eq. (2.13), which allows us to calculate output field at a sideband frequency $\Omega$ (detuning from the degenerate mode) as a function of the input fields.

$$\begin{aligned} a_{\text{out}}(\omega+\Omega) &= A(\Omega)a_{\text{in}}(\omega+\Omega) + B(\Omega)a_{\text{in}}^{\dagger}(\omega-\Omega) \\ &\quad + C(\Omega)b_{\text{in}}(\omega+\Omega) + D(\Omega)b_{\text{in}}^{\dagger}(\omega-\Omega) \end{aligned} \tag{2.13}$$

where $a_{\text{in}}$ represents external field entering the cavity through the output coupler, and $b_{\text{in}}$ describes the reservoir field that is coupled to the cavity through the combined losses, including output coupler and other losses, and $A(\Omega)$, $B(\Omega)$, $C(\Omega)$ and $D(\Omega)$ are functions of detuning, gain, cavity loss and coupling parameters explicitly given as Eqs. (3.27) to (3.30) in chapter 3.

Note that output anihilation operator from the Bogoliubov transformation in Eq.(2.13) gives us complete information about the output quantum state, allowing us to calculate both noise properties (like squeezing) and correlation functions. For example, the noise power spectral density (which divided by standard quantum limit indicates squeezing) at a side-

band frequency of $\omega$ can be computed as

$$S(\Omega) = \langle [a_{\text{out}}(\Omega) + a_{\text{out}}^{\dagger}(-\Omega)]^2 \rangle, \tag{2.14}$$

where the expectation $\langle \cdot \rangle$ in the case of an unseeded OPO is taken with respect to vacuum in both the $a$ and $b$ modes. Moreover, intensity correlation function $G^{(2)}(T)$, which can be a signature of non-classicality of a quantum state [19], is computed as a normally-ordered expectation value of creation/anihilation operators with respect to the vacuum state in both input modes:

$$G^{(2)}(T) \equiv \langle a_{\text{out}}^{\dagger}(t) a_{\text{out}}^{\dagger}(t+T) a_{\text{out}}(t+T) a_{\text{out}}(t) \rangle. \tag{2.15}$$

Cavity mode FWHM (full-width half-maximum) determines the squeezing spectrum, as well as the width in time of the intensity correlation function. One inconvenience of the Collett and Gardiner method is that it focuses on a single mode of the cavity, and it is not *a priori* clear how to incorporate multiple modes. While in the case of squeezing measurement often it makes little difference since standard homodyne detection scheme acts as a frequency filter, the $G^{(2)}(T)$ correlation function shows interference effects from multiple cavity modes when they are present. Experimental measurements of the multimode and singlemode (only degenerate mode filtered out of the multimode output) intensity correlation functions are presented in chapter 4.

Another possible limitation is that this method treats as simultaneous the nonlinear effect due to the crystal and the cavity in- and out-coupling effects, when in fact they are sequential. For these reasons, we find it more convenient to take a slightly different starting point for our calculations in chapter 3.

# Chapter 3

# Theory of multimode OPO

In this chapter we compute the output of a multimode OPO for subthreshold, but otherwise arbitrary, gain. We find analytic Bogoliubov transformations in the form of Eq. (2.13) that allow us to calculate arbitrary field correlation functions, including the second-order intensity correlation function $G^{(2)}(T)$. The results show evidence of increased coherence due to stimulated spontaneous parametric down-conversion. We extend an earlier model developed by Lu and Ou [49] to arbitrary gain and finesse, and show the extension gives accurate results in most scenarios. The results presented in this chapter are adapted from [43].

Many calculations of the fields emitted by OPOs are based on techniques developed to calculate squeezing in parametric amplifiers [49, 50]. The cavity is described in a modal expansion and quantum reservoir theory [51] is used to derive dynamical relationships between cavity, input, and output fields. When these are solved, the resulting Bogoliubov transformation expresses the output fields as squeezed versions of the input fields [48, 52]. Using this approach, Lu and Ou [49] computed $G^{(2)}(T)$, the second-order intensity correlation function for type-0 multimode OPO. Reflecting experimental conditions of the time, that calculation remained in the low-gain limit and approximated the cavity lineshapes as Lorentzian, as appropriate to high finesse cavities.

Our method is similar to the classic works of Collett and Gardiner [48]

and Gardiner and Savage [52], in that we use input-output relations for squeezing and cavity in/out-coupling to obtain equations relating input, output, and intra-cavity fields. In contrast to those works, we avoid quantum reservoir theory by posing the problem directly in the time domain. As we describe below, narrow-band cavity-enhanced spontaneous parametric down-conversion (CESPDC) is more naturally and transparently described in this way.

We find difference equations describing the input, output, and cavity fields at consecutive round-trip times. Eliminating the cavity field from these equations, we find the Bogoliubov transformation expressing the output fields in terms of the input fields. To study the time-domain structure, we calculate the second-order intensity correlation function $G^{(2)}(T)$ for a type-0 multimode OPO, including arbitrary finesse and gain. We find an envelope well approximated by a double exponential with a gain-dependent decay constant, multiplied by a comb structure with a period equal to the cavity round trip time. At low gain and high finesse this agrees with the calculation of [49]. At higher gains we find coherence beyond the cavity ring-down time due to stimulated SPDC.

## 3.1 Bogoliubov transformations

Let us consider a two-sided ring cavity as in Fig. 3.1 with roundtrip time denoted as $\tau$. We characterize the cavity amplitude transmission and reflection coefficients with real numbers $t_i$ and $r_i$, where a subscript $i = 1,2$ indicates the output coupler and another mirror representing the collective cavity losses, respectively. For each of the beamsplitters, there are four numbers describing the input-ouput relation, the transmission from inside the cavity ('c') to the exterior ('e') $t_{i,ce}$, the transmission from the exterior to the interior of the cavity $t_{i,ec}$, the reflection from inside the cavity $r_{i,cc}$ and the reflection from the outside the cavity $r_{i,ee}$.

These coefficients are related by energy conservation: $|t_{i,ce}|^2 + |r_{i,ee}|^2 = |t_{i,ec}|^2 + |r_{i,cc}|^2 = 1$ and $t_{i,ce} r^*_{i,ec} + t_{i,ec} r^*_{i,cc} = 0$. We assume that all $t$ and $r$ coefficients are real, and $t_{i,ec} = t_{i,ce} \equiv t_i$, and $r_{i,cc} = -r_{i,ee} \equiv r_i$. The intracavity field annihilation operator just before reaching the output coupler is denoted as $a$, while the input fields just before reaching the cavity are $a_{\text{in}}$ and $b_{\text{in}}$. We denote the output field just after exiting the cavity as $a_{\text{out}}$.

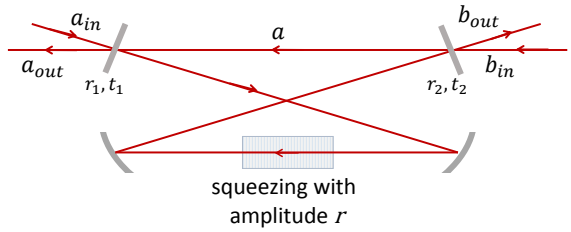


**Figure 3.1:** An OPO scheme with input, output and intracavity field operators for double-sided cavity with a nonlinear crystal inside.

The field experiences three relevant transformations during a round-trip of the cavity. Interaction with the output coupler produces

$$a \overset{\text{OC}}{\rightarrow} r_1 a + t_1 a_{\text{in}}, \tag{3.1}$$

where $a_{\text{in}}$ is the input field. Other losses (here lumped together in a single interaction) produce

$$a \overset{\text{loss}}{\rightarrow} r_2 a + t_2 b_{\text{in}}, \tag{3.2}$$

where $b_{\text{in}}$ is a bath mode assumed to be in vacuum. Finally there is the Bogoliubov transformation due to squeezing on a single pass through the

crystal

$$a \overset{\text{sq}}{\rightarrow} a\cosh(r) + a^\dagger \sinh(r), \tag{3.3}$$

where $r$ is the squeezing amplitude.

Applying these three transformations in sequence to $a(t-\tau)$ (understood to be the intra-cavity field at a location immediately before the output coupler), we have

$$\begin{aligned} a &\rightarrow r_1 a + t_1 a_{\text{in}} && (3.4)\\ &\rightarrow r_2(r_1 a + t_1 a_{\text{in}}) + t_2 b_{\text{in}} && (3.5)\\ &\rightarrow \cosh(r)[r_2(r_1 a + t_1 a_{\text{in}}) + t_2 b_{\text{in}}] \\ &\quad + \sinh(r)[r_2(r_1 a^\dagger + t_1 a_{\text{in}}^\dagger) + t_2 b_{\text{in}}^\dagger]. && (3.6) \end{aligned}$$

Considering that a round-trip takes time $\tau$ and the field $a(t)$ depends only on $a(t-\tau)$, which is true if we neglect the dispersion and finite bandwidth of the phase-matching (see below), we have

$$\begin{aligned} a(t) &= r_1 r_2 \cosh(r) a(t-\tau) + r_1 r_2 \sinh(r) a^\dagger(t-\tau) \\ &\quad + t_1 r_2 \cosh(r) a_{\text{in}}(t-\tau) + t_1 r_2 \sinh(r) a_{\text{in}}^\dagger(t-\tau) \\ &\quad + t_2 \cosh(r) b_{\text{in}}(t-\tau) + t_2 \sinh(r) b_{\text{in}}^\dagger(t-\tau) \end{aligned} \tag{3.7}$$

with the hermitian conjugate:

$$\begin{aligned} a^\dagger(t) &= r_1 r_2 \cosh(r) a^\dagger(t-\tau) + r_1 r_2 \sinh(r) a(t-\tau) \\ &\quad + t_1 r_2 \cosh(r) a_{\text{in}}^\dagger(t-\tau) + t_1 r_2 \sinh(r) a_{\text{in}}(t-\tau) \\ &\quad + t_2 \cosh(r) b_{\text{in}}^\dagger(t-\tau) + t_2 \sinh(r) b_{\text{in}}(t-\tau). \end{aligned} \tag{3.8}$$

The output field is given by

$$a_{\text{out}}(t) = -r_1 a_{\text{in}}(t) + t_1 a(t). \tag{3.9}$$

Writing

$$a(t) = \frac{1}{\sqrt{2\pi}} \int_{-\infty}^{\infty} a(\omega) e^{-i\omega t} d\omega$$
$$a^{\dagger}(t) = \frac{1}{\sqrt{2\pi}} \int_{-\infty}^{\infty} a^{\dagger}(\omega) e^{i\omega t} d\omega$$

and solving Eqs. (3.7),(3.8), (3.9) for $a_{\text{out}}$, we find the Bogoliubov transformation

$$\begin{aligned} a_{\text{out}}(\omega) = & A(\omega) a_{\text{in}}(\omega) + B(\omega) a_{\text{in}}^{\dagger}(-\omega) \\ & + C(\omega) b_{\text{in}}(\omega) + D(\omega) b_{\text{in}}^{\dagger}(-\omega) \end{aligned} \tag{3.10}$$

where

$$A(\omega) \equiv d(\omega) t_1^2 r_2 [e^{-i\omega\tau} \cosh(r) - r_1 r_2] - r_1 \tag{3.11}$$
$$B(\omega) \equiv d(\omega) \sinh(r) t_1^2 r_2 e^{-i\omega\tau} \tag{3.12}$$
$$C(\omega) \equiv d(\omega) t_2 t_1 [e^{-i\omega\tau} \cosh(r) - r_1 r_2] \tag{3.13}$$
$$D(\omega) \equiv d(\omega) \sinh(r) t_2 t_1 e^{-i\omega\tau} \tag{3.14}$$

and

$$d(\omega) \equiv \frac{1}{[e^{-i\omega\tau} - r_1 r_2 \cosh(r)]^2 - [r_1 r_2 \sinh(r)]^2}. \tag{3.15}$$

Eqs. (3.10) to (3.15) constitute a full description of the output of the OPO, in the sense that any correlation function of interest can be calculated by taking expectation values of products of $a_{\text{out}}$ and $a_{\text{out}}^{\dagger}$. For example, the degree of quadrature squeezing at a side-band frequency of $\Omega$ can be computed according to Eq. (9.5). $S(\Omega)$ is simply a polynomial in $A(\Omega)$ to $D(-\Omega)$, so analytical results are available for any gain level.

We have neglected dispersion in the cavity and the finite phase-matching

bandwidth of the crystal. These approximations are justified in typical narrow-band CESPDC scenarios [53], in which the phase matching bandwidth is several orders of magnitude larger than the free spectral range (FSR) of the cavity. Introducing a finite phase matching bandwidth would modify the shape of the peaks composing the multimode $G^{(2)}(T)$, but at a time-scale beyond the resolution of current electronics. As described in [53] the KTP nonlinear crystal introduces a dispersion of $dn/d\lambda = -0.06\ \mu\text{m}^{-1}$, which over a phase-matching bandwidth of 100 GHz ($\approx 0.2$ nm) changes the refractive index by $10^{-5}$, not shifting any of the resonances by more than $10^{-3}$ FSR. In contrast, broad-band CESPDC experiments are typically sensitive to the full output bandwidth of the OPO [54], and these approximations would not be justified.

## 3.2 Multimode $G^{(2)}(T)$

Time-domain correlation measurements on OPOs are an important diagnostic of the spectral content of the output [12, 13], and are often used to demonstrate the quantum nature of the generated fields [19, 11]. In this section we compute the intensity correlation function $G^{(2)}(T)$. As with the degree of squeezing, this can be computed analytically for any sub-threshold gain level and including all modes.

As described above, this correlation function is computed as a normally-ordered expectation value with respect to the vacuum state in both input modes:

$$G^{(2)}(T) \equiv \langle a^{\dagger}_{\text{out}}(t)a^{\dagger}_{\text{out}}(t+T)a_{\text{out}}(t+T)a_{\text{out}}(t)\rangle \tag{3.16}$$

$$= \int d^4\omega\, e^{-i(\omega_2+\omega_3)(t+T)}e^{-i(\omega_1+\omega_4)t}G^{(2)}(\vec{\omega}) \tag{3.17}$$

where $d^4\omega \equiv d\omega_1\, d\omega_2\, d\omega_3\, d\omega_4$ and

$$G^{(2)}(\vec{\omega}) \equiv \langle a^{\dagger}_{\text{out}}(-\omega_1)a^{\dagger}_{\text{out}}(-\omega_2)a_{\text{out}}(\omega_3)a_{\text{out}}(\omega_4)\rangle.$$

After the reduction of the operators using the commutation relation $[a(\omega), a^\dagger(\omega')] = \delta(\omega - \omega')$ and knowing that the coefficients $A(\omega)$, $B(\omega)$, $C(\omega)$ and $D(\omega)$ are hermitian functions, e.g. $A(-\omega) = A^*(\omega)$, we find the expression under the Fourier transform

$$\begin{aligned} G^{(2)}(\vec{\omega}) &= \delta(\omega_1+\omega_2)\delta(\omega_3+\omega_4)\Gamma(\omega_2,-\omega_1)\Gamma(\omega_3,-\omega_4) \\ &\quad +\delta(\omega_2+\omega_3)\delta(\omega_1+\omega_4)\Upsilon(\omega_1,-\omega_4)\Upsilon(\omega_2,-\omega_3) \\ &\quad +\delta(\omega_1+\omega_3)\delta(\omega_2+\omega_4)\Upsilon(\omega_1,-\omega_3)\Upsilon(\omega_2,-\omega_4) \quad (3.18) \end{aligned}$$

where

$$\Gamma(\omega,\omega') \equiv A(\omega)B(-\omega') + C(\omega)D(-\omega') \quad (3.19)$$

$$\Upsilon(\omega,\omega') \equiv B(\omega)B(-\omega') + D(\omega)D(-\omega'). \quad (3.20)$$

Performing one integral for each delta function, we arrive to an expression that is $t$-independent

$$G^{(2)}(T) = \{\mathscr{F}[\Gamma](T)\}^2 + \{\mathscr{F}[\Upsilon](T)\}^2 + \{\mathscr{F}[\Upsilon](0)\}^2 \quad (3.21)$$

where $\Gamma(\omega) \equiv \Gamma(\omega,\omega)$ and $\Upsilon(\omega) \equiv \Upsilon(\omega,\omega)$. Knowing that $r_1^2 + t_1^2 = 1$ and $r_2^2 + t_2^2 = 1$, from Eqs. (3.11)–(3.14) we find

$$\begin{aligned} \Gamma(\omega) &= d(\omega)d(-\omega)t_1^2\sinh(r)\left[(1+r_1^2r_2^2)\cosh(r)\right. \\ &\quad \left. -r_1r_2e^{i\omega\tau} - r_1r_2e^{-i\omega\tau}\right], \quad (3.22) \\ \Upsilon(\omega) &= d(\omega)d(-\omega)t_1^2\sinh(r)^2(1-r_1^2r_2^2). \quad (3.23) \end{aligned}$$

The necessary Fourier transforms are computed in the Appendix A, see Eqs. (A.19) and (A.17), in terms of a function $F(k)$, defined in Eq. (A.5).

We find

$$\{\mathscr{F}[\Gamma](T)\}^2 = t_1^4 \sinh(r)^2 \sum_{k=-\infty}^{\infty} \delta(T-k\tau) \times \left[(1+r_1^2 r_2^2)\cosh(r)F(|k|) - r_1 r_2 F(|k|+1) - r_1 r_2 F(|k|-1)\right]^2 \quad (3.24)$$

$$\{\mathscr{F}[\Upsilon](T)\}^2 = t_1^4 \sinh(r)^4 (1-r_1^2 r_2^2)^2 \times \sum_{k=-\infty}^{\infty} \delta(T-k\tau)F(|k|)^2 \quad (3.25)$$

$$\{\mathscr{F}[\Upsilon](0)\}^2 = t_1^4 \sinh(r)^4 (1-r_1^2 r_2^2)^2 F(0)^2, \quad (3.26)$$

the three terms necessary to calculate $G^{(2)}(T)$. As shown in Fig. 3.2, $G^{(2)}(T)$ of the multimode cavity output has an envelope similar to the shape of double falling exponential and peaks every cavity roundtrip time, resulting from the interference between the modes. In contrast, the single mode $G^{(2)}(T)$ would also have a double exponential decay, but without the comb structure [49].

## 3.3 Comparison with earlier work

The $G^{(2)}(T)$ calculation of Lu and Ou [49] found the multimode $G^{(2)}(T)$ to be a comb of (approximate) Dirac delta functions spaced by the cavity round-trip time, multiplied by an envelope given by the single-mode $G^{(2)}(T)$. This result has an appealing simplicity, and is intuitive in the time-domain picture in which photon pairs are produced simultaneously but may spend a different number of round trips in the cavity before escaping. It is interesting to ask whether the same behaviour persists also at higher gains, i.e. in the presence of stimulated SPDC.

We compare our $G^{(2)}(T)$, Eq. (3.21), against the natural extension of the Lu and Ou model for arbitrary gain, but still within the high-finesse

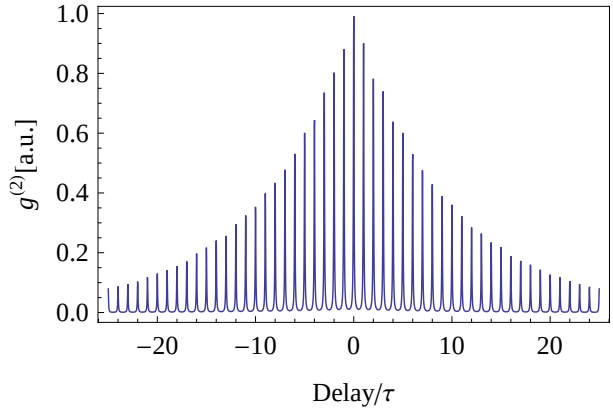


**Figure 3.2:** A graph showing the theoretical $G^{(2)}(T)$ calculated for cavity parameters as for the source presented in [53] with gain equal to 1% of the OPO threshold. The envelope of the $G^{(2)}(T)$ is calculated from Eqs. (3.21), (3.24) and (3.25), and normalized to unity at $T = 0$. For the purpose of plotting, the peaks, which in the model are Dirac delta functions, have been replaced with finite-width Lorentzians.

approximation. In this section we follow the notation of Refs. [49] and [48], and write $\exp[-\gamma_i\tau] = r_i$ to describe losses and $2\varepsilon = r$ to describe gain. The single mode Bogoliubov transformations from [48], without the low-gain approximation, are

$$A_{\text{single}}(\omega) \equiv \frac{(\gamma_1/2)^2 - (\gamma_2/2 - i\omega)^2 + |\varepsilon|^2}{(\gamma_1/2 + \gamma_2/2 - i\omega)^2 - |\varepsilon|^2} \tag{3.27}$$

$$B_{\text{single}}(\omega) \equiv \frac{\gamma_1\varepsilon}{(\gamma_1/2 + \gamma_2/2 - i\omega)^2 - |\varepsilon|^2} \tag{3.28}$$

$$C_{\text{single}}(\omega) \equiv \frac{\sqrt{\gamma_1\gamma_2}(\gamma_1/2 + \gamma_2/2 - i\omega)}{(\gamma_1/2 + \gamma_2/2 - i\omega)^2 - |\varepsilon|^2} \tag{3.29}$$

$$D_{\text{single}}(\omega) \equiv \frac{\sqrt{\gamma_1\gamma_2}\varepsilon}{(\gamma_1/2 + \gamma_2/2 - i\omega)^2 - |\varepsilon|^2}. \tag{3.30}$$

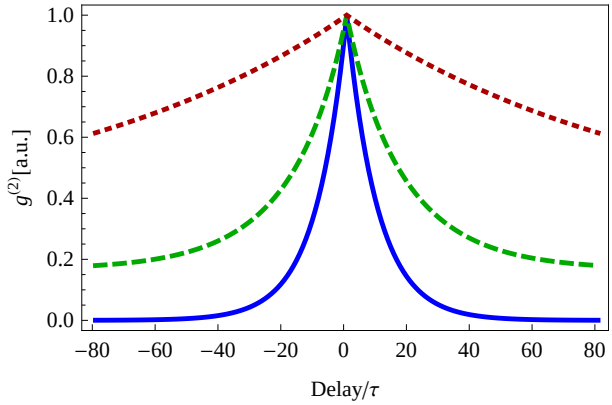


**Figure 3.3:** Three envelopes of multimode $G^{(2)}(T)$, computed from Eqs. (3.21), (3.24) and (3.25) and normalized to unity at $T = 0$. Curves show $G^{(2)}(T)$ for the gain $r$ equal to 1% (blue), 50% (green, dashed), 90% (red, dotted) of the threshold gain $r_{th}$. Cavity parameters are as for the source presented in [53].

We follow the same steps as from Eq. (3.16) to Eq. (3.21), to find

$$\begin{aligned} G^{(2)}_{\text{single}}(T) &= \{\mathscr{F}_{\text{single}}[\Gamma](T)\}^2 + \{\mathscr{F}_{\text{single}}[\Upsilon](T)\}^2 \\ &\quad + \{\mathscr{F}_{\text{single}}[\Upsilon](0)\}^2 \end{aligned} \tag{3.31}$$

where

$$\{\mathscr{F}_{\text{single}}[\Gamma](T)\}^2 = \frac{\pi}{2}\gamma_1^2\varepsilon^2\,(f_- + f_+)^2 \tag{3.32}$$

$$\{\mathscr{F}_{\text{single}}[\Upsilon](T)\}^2 = \frac{\pi}{2}\gamma_1^2\varepsilon^2\,(f_- - f_+)^2 \tag{3.33}$$

$$f_\pm \equiv \frac{e^{-\frac{1}{2}|T|(\gamma_1+\gamma_2\pm 2\varepsilon)}}{\gamma_1+\gamma_2\pm 2\varepsilon} \tag{3.34}$$

Finally, we multiply by a comb of (approximate) delta functions. Again following [49], for a multimode cavity with $2N+1$ modes we have:

$$G^{(2)}_{\text{multi}}(T) \propto G^{(2)}_{\text{single}}(T)\frac{\sin^2[(2N+1)\pi T/\tau]}{\sin^2[\pi T/\tau]} \tag{3.35}$$

$$\lim_{N\to\infty} G^{(2)}_{\text{multi}}(T) \propto G^{(2)}_{\text{single}}(T)\sum_{n=-\infty}^{\infty}\delta(T-n\tau). \tag{3.36}$$

Eq. (3.31), computed by extension of [49], agrees very closely with our multimode result Eq. (3.21), shown in Fig. 3.3. The only situation for which the two approaches give significantly different results is when the output coupler has high transmission $t_1$. Even so, the difference between the two calculations does not exceed 7.5% of the value of $G^{(2)}(T)$, for $r_1, r_2 > 0.5$ and for any sub-threshold gain. We conclude that for many purposes the very simple results of Eq. (3.31) can be used, backed by the more accurate calculation given in Section 3.2.

Fig. 3.3 shows the computed shape of the $G^{(2)}(T)$ envelope as a function of gain parameter $r$. This clearly shows a broadening of the correlations, along with a raising of the background level, which persists to arbitrarily large $|T|$. The background can be understood as a result of "accidental" coincidences, i.e. correlations among photons that were not produced in the same SPDC event. The broadening is the time-domain manifestation of the narrowing of the resonances with increasing $r$, visible e.g. in $d(\omega)$. Physically, it can be understood as the coherent amplification of SPDC photons already inside the cavity, i.e., stimulated SPDC. This change in photon temporal distributions is of potential interest in wavefunction matching for non-classical interference [55], matching to quantum memories [56], and detection of "Schrödinger kittens" and other time-localized non-classical fields [57].

## 3.4 Summary

We have computed the output of a multimode cavity-enhanced spontaneous parametric down-conversion source, including realistic mode structure and sub-threshold but otherwise arbitrary gain. Using time-domain difference equations describing field operators at consecutive roundtrips, we find multimode Bogoliubov transformations that describe the output field. This analytic solution provides a basis for calculations of any correlation function describing the multimode output. We compute the two-time intensity correlation function $G^{(2)}(T)$, and find increased temporal coherence due to stimulated SPDC in both single and multimode cases. We extend a calculation by Lu and Ou [49] to arbitrary gain, and find that it agrees well with our more exact calculation. The results will be useful in describing high-gain spontaneous parametric down-conversion.

# Chapter 4

# Singlemode and multimode OPO: Experiment

In this chapter we demonstrate atomic filtering of frequency-degenerate photon pairs from a sub-threshold OPO. The filter, a modified Faraday anomalous dispersion optical filter (FADOF), achieves 70% peak transmission simultaneous with 57 dB out-of-band rejection and a 445 MHz transmission bandwidth. When applied to the OPO output, only the degenerate mode, containing one-mode squeezed vacuum, falls in the filter pass-band; all other modes are strongly suppressed. The high transmission preserves non-classical continuous-variable features, e.g. squeezing or non-gaussianity, while the high spectral purity allows reliable discrete-variable detection and heralding. Correlation and atomic absorption measurements indicate a spectral purity of 96% for the individual photons, and 98% for the photon pairs. The results presented in this chapter are adapted from [44].

The concept of the experiment presented in this chapter is shown in Fig. 4.1. The squeezed vacuum at the $D_1$ line of atomic rubidium is generated by a sub-threshold OPO consisting of an optical resonator with a blue-light-pumped $\chi^{(2)}$ nonlinear medium inside. The OPO generates narrowband near atom-resonant squeezed vacuum in the degenerate cavity mode, i.e., the longitudinal mode with half the pump frequency, but also a

far larger number of two-mode squeezed states in other modes. We use a modified Faraday rotation anomalous-dispersion optical filter (FADOF) [58] to separate the single-mode squeezed vacuum from these other, co-propagating, modes. Previously, atomic filters have been used to filter single photons [59] and polarization-distinguishable photon pairs [4], but with lower efficiencies (up to 14%), incompatible with non-classical continuous-variable states.

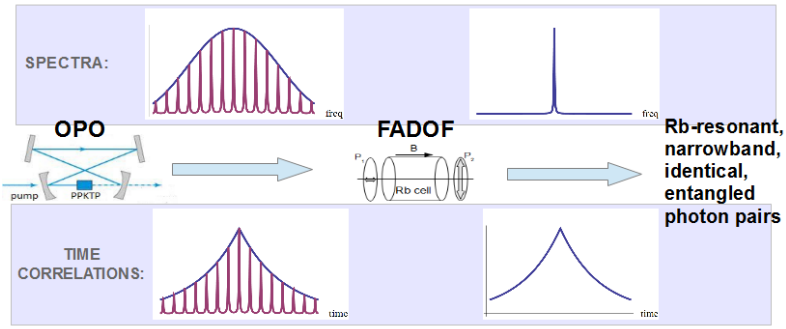


**Figure 4.1:** The concept of the OPO filtering experiment, showing the effect of selecting only a degenerate mode in spectral domain and in time domain. The unfiltered intensity correlation function displays a comb structure (as calculated in the previous chapter), as opposed to the single-mode case.

With this new FADOF we observe 70% transmission of the degenerate mode through the filter, compatible with 5 dB of squeezing, simultaneous with out-of-band rejection by 57 dB, sufficient to reduce the combined non-degenerate emission to a small fraction of the desired, degenerate mode emission. In comparison, a recently-described monolithic filter cavity achieved 60% transmission and 45 dB out-of-band rejection [60]. We test the filter by coincidence detection of photon pairs from the squeezed vacuum, which provides a stringent test of the suitability for use at the single-photon level. We observe for the first time fully-degenerate, near atom-resonant photon pairs, as evidenced by correlation

functions and atomic absorption measurements. The 96% spectral purity we observe is the highest yet reported for photon pairs, surpassing the previous record of 94% [59], and in agreement with theoretical predictions.

## 4.1 Experimental setup

### 4.1.1 Source of photon pairs

In our experiment, a doubly-resonant degenerate OPO [53] featuring a type-0 PPKTP crystal produces single-mode squeezed vacuum at 794.7 nm. A continuous wave external cavity diode laser is stabilised at the frequency $\omega_0$ of maximum transmission of the FADOF (2.7 GHz to the red of the Rb $D_1$ line centre, as in [58]): an electro-optic modulator (EOM) adds sidebands to the saturated spectroscopy absorption signal in order to get an error signal at the right frequency. In order to generate pairs at $\omega_0$, we double the laser frequency, via cavity-enhanced second harmonic generation in a LBO crystal, generating the 397.4 nm pump beam for the OPO.

With this configuration, photon pairs are generated at the resonance frequencies of the OPO cavity that fall inside the 150 GHz-wide phase matching envelope of the PPKTP crystal. Hence, the OPO output is composed by hundreds of frequency modes, each of 8.4 MHz bandwidth, separated by the 501 MHz free spectral range. This means that the FADOF - with its 445 MHz bandwidth - can successfully filter all the nondegenerate modes, leaving only the photons in the degenerate mode, which are then fully indistinguishable, as they share the same spatial mode, frequency and polarization.

The light generated by the OPO is then sent through a polarization-maintaining fiber to the filter setup, filtered by the FADOF described

in the next subsection, and coupled to a fiber beamsplitter. The detection scheme is described in the subsection 4.1.3.

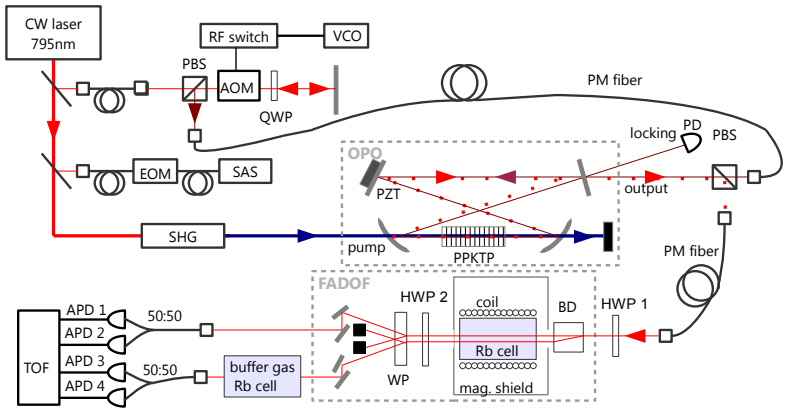


**Figure 4.2:** Experimental setup of the OPO, the FADOF filter and detection system. Symbols: PBS: polarizing beam splitter, AOM: acousto-optic modulator, EOM: electro-optic modulator, APD: avalanche photodiode, BD: calcite beam displacer, WP: Wollaston prism, TOF: time-of-flight analyzer, SAS: saturated absorption spectroscopy, VCO: voltage controlled oscillator, PM: polarization maintaining fiber, HWP: half-wave plate, QWP: quarter-wave plate, PD: photodiode

### 4.1.2 Faraday Anomalous Dispersion Optical Filter

The FADOF consists of a hot atomic vapor cell between two crossed polarizers (see Fig.4.3) that block transmission away from the absorption line, while the absorption itself blocks resonant light. A homogeneous magnetic field along the propagation direction induces circular birefringence in the vapor, so that the Faraday rotation just outside the Doppler profiles of the absorption lines can give high transmission for a narrow range of frequencies.

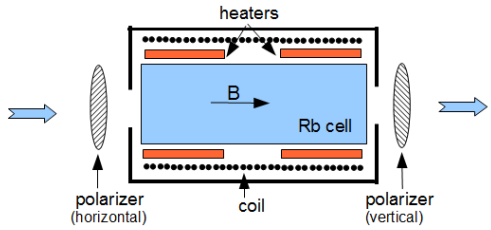


**Figure 4.3:** The elements of the FADOF filter. The light that has the polarization rotated by the Rb vapour and passes through the filter belongs to the region close to the atomic resonance.

In my previous (pre-PhD) work the FADOF filter on the $D_1$ line in Rb was studied in detail [58]. The filter used in this experiment is the same as in the cited paper, except it has been modified to work for two orthogonal polarizations: instead of the crossed polarizers, we use a beam displacer before the cell, so that the two orthogonal polarizations travel along independent parallel paths in the cell. After the cell we use a Wollaston prism to separate the near-resonant filtered light from the unrotated one. The optical axes of the two polarizing elements are oriented with precision mounts, and an extinction ratio of $1.8 \times 10^{-6}$ is reached. This strategy exploits the imaging capability of the filter.

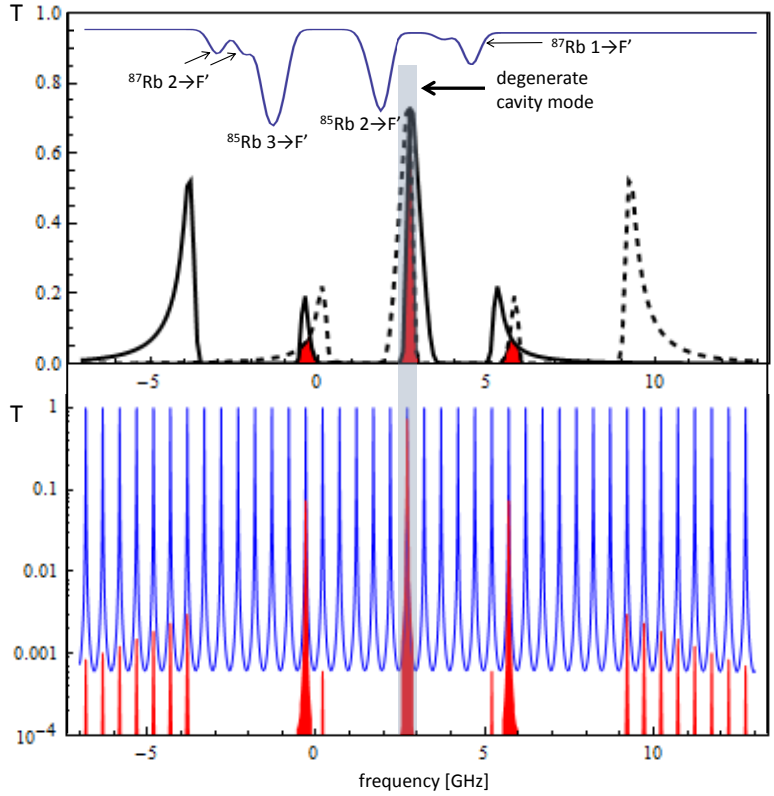


**Figure 4.4:** A scheme illustrating filtering of the photon pairs. Upper plot: reference transmission spectrum of room temperature natural abundance Rb (blue), filter spectrum (black) and a mirror filter spectrum with respect to the degenerate cavity mode (black dashed). Red shaded regions indicate transmission of correlated photon pairs. Lower plot: cavity output spectrum (blue) and FADOF-filtered cavity spectrum (red). The degenerate cavity mode coincides with the FADOF peak. Both figures have the same frequency scale.

Additionally, the setup has been supplemented with a half-waveplate placed before the Wollaston prism (HWP 2 in Fig. 5.4), which enables us to, in effect, turn on and off the filter. In the "FADOF on" condition,

the waveplate axis is set parallel to the Wollaston axis (and thus the waveplate has no effect on the filter behaviour), the magnetic field is 4.5 mT and the temperature is 365 K. In the "FADOF off" condition, no magnetic field is applied, the temperature of the cell is also 365 K and HWP 2 is set to rotate the polarization by 90 degrees, in effect swapping the outputs, so that almost all the light is transmitted through the setup without being filtered.

The FADOF filters reported in literature are normally optimized for peak transmission and low total transmitted background [61]. However, here we are using a common criterion for experiments with photon pairs: we maximize the ratio of coincidences due to photon pairs belonging to the degenerate mode to coincidences due to other photon pairs. Because of energy conservation, the two photons in any SPDC pair will have frequencies symmetrically placed with respect to the degenerate mode; to prevent the pair from reaching the detectors, it suffices to block at least one of the photons. In terms of filter performance, this means that it is possible to have near-perfect filtering even with transmission in some spectral windows away from the degenerate mode, provided the transmission is asymmetrical (Fig. 4.4). Using this criterion we find the optimal conditions for the filter performance in our experiment to be 4.5 mT of magnetic field and the cell temperature of 365 K. The optimum filter performance requires the degenerate mode that should be filtered to coincide with the FADOF transmission peak at a fixed frequency (2.7 GHz to the red from the center of the Rb $D_1$ line).

### 4.1.3 Detection

The distribution of arrival times of photons in a Hanbury-Brown-Twiss configuration is useful to check that the filter effectively suppresses the non-degenerate modes of the type-0 OPO described in the previous section. We collect the OPO output in a polarization maintaining fiber and send it through the filter setup. The filtered light is then coupled into balanced fiber beam splitters that send the photons to avalanche photodetectors (APDs), connected to a time-of-flight analyzer (TOF) that allows us to measure the second order correlation function $G^{(2)}(T)$ (see Fig. 5.4).

Since we are using single photon detectors, we need to reduce as much as possible the background due to stray light sources in the setup. The main source of background light is the counter-propagating beam that we inject in the OPO in order to lock the cavity length to be resonating at $\omega_0$. We tackle this problem using a chopped lock: the experiment switches at 85 Hz between periods of data acquisition and periods of stabilization. During periods of data acquisition, the AOM is off, and thus no locking beam is present. During periods of stabilization, the AOM is on, and an electronic gate circuit is used to block electronic signals from the APDs, preventing recording of detections due to the locking beam photons. In addition, the polarization of the locking beam is orthogonal to that of the OPO output.

### 4.1.4 Filter non-degenerate modes

In this section we consider the second order correlation function of the field operators $a_{\text{out}}$ in a form:

$$G^{(2)}(T) \propto \langle a^{\dagger}_{\text{out}}(t) a^{\dagger}_{\text{out}}(t+T) a_{\text{out}}(t+T) a_{\text{out}}(t) \rangle \tag{4.1}$$

for multimode (unfiltered) and single-mode (filtered) output of the OPO.

As shown in Lu et al. [49], $G^{(2)}(T)$ describing the output of a single-mode, far-below-threshold OPO has the form of double exponential decay

$$G^{(2)}_{\text{single}}(T) \propto e^{-|T|(\gamma_1+\gamma_2)}, \tag{4.2}$$

where the reflectivity of the output coupler is $r_1 = \exp[-\gamma_1\tau]$, the effective reflectivity resulting from intracavity losses is $r_2 = \exp[-\gamma_2\tau]$ and $\tau$ is the cavity round-trip time. An ideal narrowband filter would remove all the nondegenerate cavity-enhanced spontaneous down-conversion modes, reducing the $G^{(2)}(T)$ to $G^{(2)}_{\text{single}}(T)$. This filtering effect was demonstrated in [59] for a type-II OPO and an induced dichroism atomic filter.

In the previous chapter we explain that when the filter is off, so that the output consists of $N$ cavity modes, $G^{(2)}(T)$ takes the form

$$G^{(2)}_{\text{multi}}(T) \propto G^{(2)}_{\text{single}}(T)\frac{\sin^2[(2N+1)\pi T/\tau]}{(2N+1)\sin^2[\pi T/\tau]} \tag{4.3}$$

$$\approx G^{(2)}_{\text{single}}(T)\sum_{n=-\infty}^{\infty}\delta(T-n\tau), \tag{4.4}$$

i.e., with the same double exponential decay but modulated by a comb with a period equal to the cavity round-trip time $\tau$. In our case the bandwidth of the output contains more than 200 cavity modes, and the fraction in Eq. (4.3) is well approximated by a comb of Dirac delta functions.

The comb period of $\tau = 1.99$ ns is comparable to the $t_{\text{bin}} = 1$ ns resolution of our counting electronics, a digital time-of-flight counter (Fast ComTec P7888). This counter assigns arrival times to the signal and idler arrivals relative to an internal clock. We take the "window function" for the $i$th bin, i.e., the probability of an arrival at time $T$ being assigned to that bin, to be

$$f^{(i)}(T) = \begin{cases} 1, & \text{if } T \in [it_{bin}, (i+1)t_{bin}], \\ 0, & \text{otherwise}. \end{cases} \tag{4.5}$$

Without loss of generality we assign the signal photon's bin as $i = 0$, and we include an unknown relative delay $T_0$ between signal and idler due to path length, electronics, cabling, and so forth. For a given signal arrival time $t_s$, the rate of idler arrivals in the $i$th bin is $\int dt_i\, f^{(i)}(t_i) G^{(2)}_{\text{multi}}(t_i - t_s - T_0)$ ($t_i$ is the idler arrival time). This expression must be averaged over the possible $t_s$ within bin $i = 0$. We also include the "accidental" coincidence rate $G^{(2)}_{\text{acc}} = t_{\text{bin}} R_1 R_2$, where $R_1, R_2$ are the singles detection rates at detectors $1, 2$, respectively. The rate at which coincidence events are registered with $i$ bins of separation is then

$$\begin{aligned} G^{(2)}_{\text{multi,det}}(i) &= \frac{1}{t_{\text{bin}}} \int dt_s\, f^{(0)}(t_s) \int dt_i\, f^{(i)}(t_i) G^{(2)}_{\text{multi}}(t_i - t_s - T_0) \\ &\quad + G^{(2)}_{\text{acc}} \qquad (4.6) \\ &= \sum_{n=-\infty}^{\infty} G^{(2)}_{\text{single}}(n\tau) \frac{1}{t_{\text{bin}}} \int_0^{t_{\text{bin}}} dt_s\, f^{(i)}(t_s + T_0 + n\tau) \\ &\quad + G^{(2)}_{\text{acc}}. \qquad (4.7) \end{aligned}$$

We take $T_0$ is a free parameter in fitting to the data. Note that if we write $T_0 = k t_{\text{bin}} + \delta$ then the simultaneous events fall into $k$th bin and $\delta \in [-t_{\text{bin}}/2, t_{\text{bin}}/2]$ determines where the histogram has the maximum visibility due to the beating between the 1 ns sampling frequency of the detection system and the 1.99 ns comb period. APD time resolution is estimated to be 350 ps FWHM (manufacturer's specification), i.e. significantly less than the TOF uncertainty, and is not included here.

Histograms of photon arrival time differences for the "FADOF off" and "FADOF on" configurations are shown in Figs. 4.5 and 4.6, respectively. We observe that the double exponential full-width at half-maximum corresponds to the predicted one of 26 ns. Moreover, we notice how the comb structure is not present in the "filter on" data, as expected if the filter blocks all pairs not in the degenerate mode.

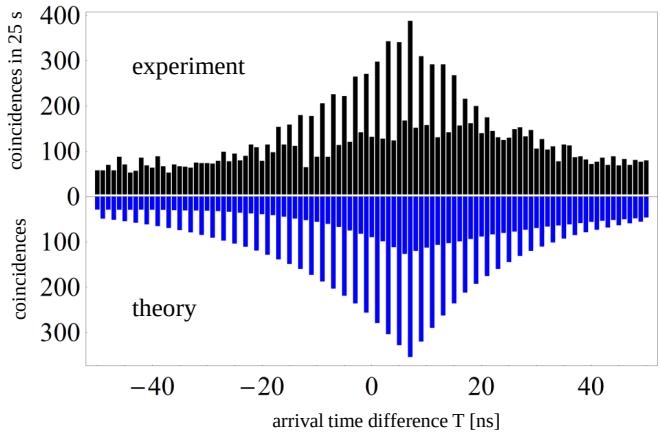


**Figure 4.5:** Histograms of arrival time differences for FADOF off compared to theoretical model (both include the background due to accidental coincidences and the artefacts resulting from 1 ns resolution of the counting electronics).

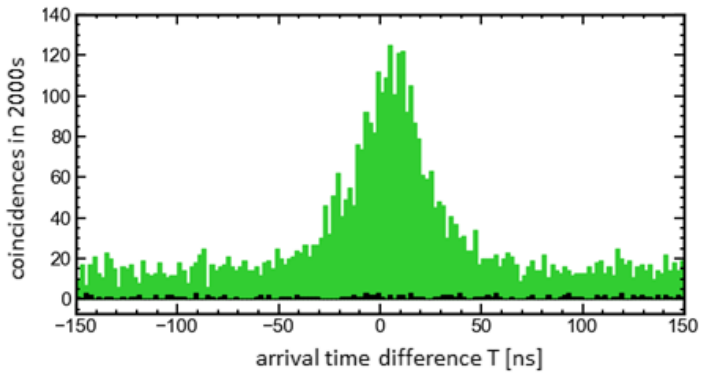


**Figure 4.6:** Histograms of the differences of arrival times of the photon pairs for FADOF on (green) and FADOF on with hot cell on the path (black). No background has been subtracted.

### 4.1.5 Spectral purity

According to the theoretical filter spectrum from [58], we estimate that 98% of the atom-resonant photon pairs come from degenerate mode (see Fig. 4.4). In order to test how much light outside the Rubidium $D_1$ line can pass through our FADOF, we split the light equally between the two different polarization paths of the filter setup by means of a half-wave plate put before the beam displacer (HWP 1 in Fig.5.4). A natural-abundance Rb vapor cell, with 10 Torr of $N_2$ buffer gas and heated until it is opaque for resonant light, is inserted in one of the paths after the filter. The collisionally-broadened absorption from this cell blocks the entire FADOF transmission window, allowing us to compare the arrival time histograms with and without the resonant component.

The number of photons detected after passing through the hot Rb cell is comparable to dark counts, meaning that most of the filtered light is at the chosen frequency $\omega_0$. We define the spectral purity $P_S$ of the FADOF as $P_S \equiv 1 - c_{HC}/c_F$, where $c_{HC}$ ($c_F$) is the number of photon pairs which were recorded within a coincidence windows of 50 ns in the path with (without) the hot cell. Considering raw coincidences (no background subtraction), we obtain $P_S = 0.98$, meaning that the filtered signal is remarkably pure, as only the 2% of the recorded pairs are out of the filter spectrum. This 2% agrees with measurements of the polarization extinction ratio with the FADOF off, i.e., it is due to technical limitations of the polarization optics and could in principle be improved. Knowing that 98% of the photon pairs transmitted through the filter within the Rb resonance come from the degenerate cavity mode (due to filter spectrum), we conclude that 96% of the pairs exiting the filter come from the degenerate mode.

## 4.2 Continuous-variable measurement

In this section we describe a noise contribution that in principle the FADOF filter might add to the filtered beam. Since the filter is a passive, linear device, the transformation that the anihilation operator undergoes when passing the filter is unitary:

$$a_{\text{out}} \to ta + rb \tag{4.8}$$

where $r^*t + rt^* = 0$, $|r|^2 + |t|^2 = 1$, operator $a$ represents the probe field and operator $b$ the vacuum field. Let us assume that filter transmission $t = \bar{t} + \delta t$ randomly fluctuates around mean value $\bar{t}$ with an amplitude $\delta t$.

In order to estimate the effect such a device would have on the probe beam, we calculate the variance of the detected quadrature operator $\hat{X}_\theta = a\exp[i\theta] + a^\dagger \exp[-i\theta]$ averaged over the angle $\theta$ on the input state being a mixture of coherent states $\rho = \int d^2\alpha P(\alpha)|\alpha\rangle\langle\alpha|$ with a mean value $\bar{\alpha}$ fluctuating with an amplitude $\delta\alpha$. We find the quadrature noise has a form

$$\begin{aligned} \langle \text{var}(\hat{X}_\theta)\rangle_\theta &= 1 + 2\text{Re}(\bar{t}\bar{\alpha})\text{Re}(\bar{\alpha}\delta t + \bar{t}\delta\alpha) \\ &\quad + 2\text{Im}(\bar{t}\bar{\alpha})\text{Im}(\bar{\alpha}\delta t + \bar{t}\delta\alpha) + O(\delta\alpha\delta t) \end{aligned} \tag{4.9}$$

Attenuation of the input probe intensity by a factor of $T_{\text{ND}}$ with a neutral-density filter effects the changes $t \to t$, $\alpha \to t_{\text{ND}}\alpha$, $\delta\alpha \to t_{\text{ND}}\delta\alpha$, where $t_{\text{ND}} \equiv \sqrt{T_{\text{ND}}}$ is the amplitude transmission. Scaling with $t_{\text{ND}}$ allows us to separate the different contributions: The first term is the SQL, and scales as $t_{\text{ND}}^0$. The second term is noise introduced by the filter, and scales as $t_{\text{ND}}^2$. The last term vanishes if $\delta\alpha$ and $\delta t$ are uncorrelated, and even without this assumption can be assumed much smaller than

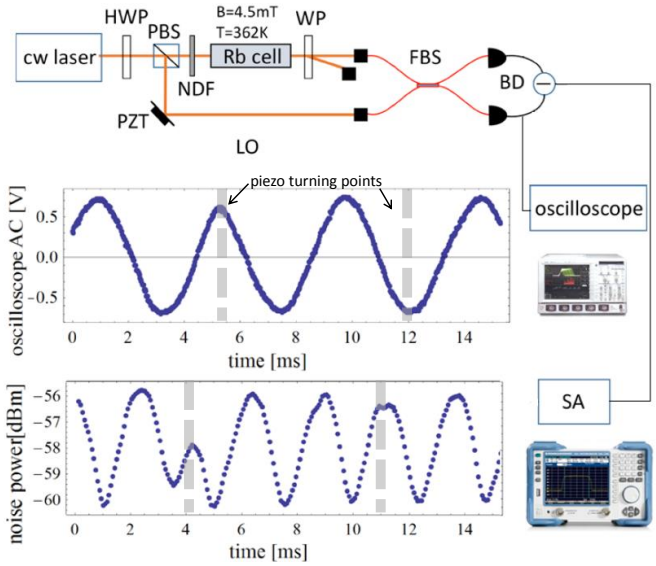


**Figure 4.7:** Experimental setup and traces from the oscilloscope and the spectrum analyzer. HWP- half-wave plate, PBS- polarization beam-splitter, WP - Wollaston prism, FBS- 50/50 fiber beam-splitter, BD - balanced detector, PZT - piezoelectric actuator, SA - spectrum analyzer.

the other terms. The average signal $\langle \hat{X}_{\text{out}} \rangle$ scales as $t_{\text{ND}}$, providing a convenient measure of the input power. We perform an experiment in order to estimate the filter technical noise at the probe power similar to the intensity of non-classical light from our source.

The experimental setup is shown in Fig. 4.7. A continuous wave laser, stabilized at the FADOF peak frequency (as described in the section 4.1) is split into a strong (1 mW) local oscillator beam (LO) and a weak (1 $\mu$W) probe beam passing through the FADOF. The relative phase $\theta$ of the two beams is controlled by a mirror mounted on the piezo-electric actuator driven with a triangle wave at approximately 70 Hz. The two beams are coupled into single-mode fibers and combined on a

fiber beamsplitter, the outputs of which are fed to the balanced detector (Thorlabs PDB450A) with a gain of $10^5$ over a bandwidth of 4.5 MHz. The difference output of the balanced detector is recorded by a spectrum analyzer in a zero-span mode with center frequency of 2 MHz, resolution bandwidth of 300 kHz and video bandwidth of 100 Hz. The monitor output of one of the two photodiodes comprising the balanced detector is simultaneously recorded on an AC-coupled oscilloscope (SC).

As shown in Fig. 4.7, we observe oscillations in both the SA and SC signals versus $\theta$. The SC signal indicates the mean detected quadrature. We keep the peak-to-peak variation as a convenient measure of the field strength. The SA signal indicates the noise of the detected quadrature. This oscillates with $\theta$, presumably because of excess laser phase noise leading to extra variance in the phase quadrature. As seen in the figure, it oscillates at twice the rate of the SC oscillations, as expected for a noise measurement.

In Fig. 4.8 we plot the mean, and the maximum and minimum, averaged over a few cycles, of the noise oscillations on the SA as a function of the probe power (proportional to the variance of the oscilloscope signal). The measurement runs from zero probe power to 1 $\mu$W. The power at 1 $\mu$W is measured with a power meter, which provides a calibration for the SC measurements. As seen in the figure, below about 10 nW of probe the mean noise level drops to the shot noise level and the oscillations disappear. 10 nW corresponds to a photon flux of $4 \times 10^{10}$ photons per second, much larger than typical photon fluxes for our OPO with 8 MHz bandwidth, e.g. $\approx 10^7$ photons/s at 3 dB of squeezing. A dependence of mean noise power on the probe power (constant and linear term) is fitted according to the model of Eq. (4.9) and represented in the Fig. 4.8. Extrapolating the contribution of noise from the filter (linear term) we estimate that at the power level of $10^7$ photons/s, the filter would introduce approximately $-150$ dBm of electronic noise, corresponding

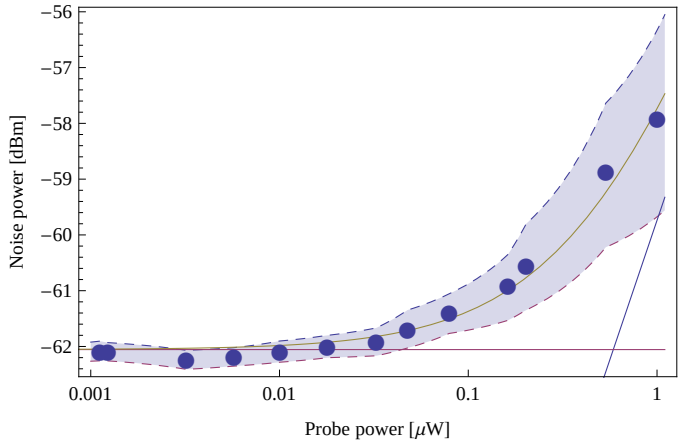


**Figure 4.8:** Average maxima and minima (dashed lines) and mean value (blue circles) of the noise oscillations detected on the SA due to the laser phase noise, as a function of the variance of the oscilloscope signal proportional to the probe power. The solid lines represent the fitted noise model (brown), a sum of a term linear with power (blue) and shot noise (red).

to −88 dB of noise with respect to the shot noise level.

The measurement we performed shows that the FADOF does not add significant amount of noise to the coherent probe, which in turn indicates that it is possible to send through a squeezed state without destroying it. For example, input squeezing of 6 dB, after passing through the filter would be reduced to 3.2 dB due to the filter's 70% transmission.

## 4.3 Summary

We have demonstrated the use of a high-performance atomic filter to separate fully degenerate photon pairs from the broadband emission of a sub-threshold OPO, or equivalently a CESPDC source. The filter, based on the FADOF principle, achieves simultaneously sufficient out-of-band

rejection to allow accurate photon-counting detection and sufficient transmission to preserve continuous-variable characteristics such as squeezing. Combining these properties in the narrow-band regime is critical to generation of hybrid continuous-variable/discrete-variable states compatible with atomic systems, e.g. quantum memories.

# Chapter 5

# Squeezed light source for interaction with atoms

This chapter explains the motivation behind developing the monolithic optical parametric oscillator, described in the remainder of this thesis. The source is optimized for interaction of the atom-resonant squeezed light it emits with the cold atomic ensemble, in particular a spinor Bose-Einstein condensate of $^{87}$Rb atoms. First we describe the benefits of Faraday probing the atoms with the polarization squeezed light, then compare different OPO architectures with this particular application in mind.

The concept of squeezed light and the advantage it offers in interferometric measurements that use only one quadrature for detection dates back to Carl Caves' work in the 1980s [62], which points out that squeezed light fed into a Mach-Zender interferometer can improve its sensitivity to below the standard quantum limit. This strategy is analogous to sending polarization-squeezed probe light through an atomic ensemble and detecting Faraday rotation it acquires because of the interaction with the atoms.

We describe polarization squeezed light in terms of Stokes operators $\hat{S}_i$ that couple to the operators $\hat{J}_i$ describing collective spin of the atoms. Performing a measurement of squeezed Stokes variable will allow us

to observe polarization rotation because of interaction with atoms with sensitivity below shot-noise limit.

If we denote a light-atoms interaction hamiltonian as $\hat{H}_{\text{int}}$, the evolution of a Stokes operator $\hat{S}_i$ in the first order yields:

$$\hat{S}_i^{(\text{out})} = \hat{S}_i^{(\text{in})} + \frac{\tau}{i\hbar}[\hat{S}_i^{(\text{in})}, \hat{H}_{\text{int}}] \tag{5.1}$$

where $\tau$ is the interaction time. This relation allows us to identify the sources of the unwanted noise in the measurement, knowing that the second term is the signal. Using a classical probe light the measurement is limited by probe shot noise introduced by $\hat{S}_i^{\text{in}}$. In case this is the main source of measurement noise, employing a squeezed probe can offer significant improvement in sensitivity without increasing the probe power (which is proportional to back-action of the light on the atoms that we want to avoid). The aim is to use polarization squeezed probe to decrease this noise below the standard quantum limit and use this technique for Faraday-rotation imaging of the spinor Bose-Einstein condensate of $^{87}$Rb atoms. The spinor condensate is an ensamble of $f = 1$ spin atoms, which means it has three $m_F = 0, \pm 1$ magnetic sublevels. The population of this levels determines the overall magnetization of the ensemble, that is mapped into the polarization of the Faraday probe.

The possibilities that open in Faraday probing of the BEC are the motivation for developing a squeezed light source consisting of a monolithic optical parametric oscillator with characteristics optimized for the experiment and a compact, stable and robust design that will facilitate incorporating it into already complex atom-trapping experiment.

## 5.1 Faraday probing of the BEC

Faraday rotation based techniques have been used to measure magnetization (population of spin states) of a spinor Bose-Einstein condensate [63, 64]. The advantage of this approach is that by measuring Faraday rotation of the probe beam (proportional to $\vec{F}$ component along the beam) one can retrieve the information about both phase and population of the $m_F$ sublevels, as opposed to direct population measurement by Stern-Gerlach separation followed by absorption imaging. Additionally, Faraday rotation measurement does not destroy he magnetization or the ensemble [65].

To date, experiments aimed at investigating BEC physics with Faraday rotation include the experiment in Jacob Sherson's group that uses dark field imaging of spatially resolved Faraday rotation on electron-multiplying CCD (EMCCD) to invesigate dynamic behavior of their system [63]. They report that the sensitivity they can achieve is limited by the shot noise of the probe beam, additionally amplified by the EM gain. Kaminski et. al. [66] demonstrate also a spatially-resolved Faraday rotation as a method of imaging the end plane of the ensemble on a CCD.

Faraday probing can potentially be useful in investigating certain aspects of spinor dynamics in BEC, like spin mixing described in [67] and [68]. These processes are an analogue of four wave mixing in optics - a populations of $m = \pm 1$ are transferred into $m = 0$ states and oscillations between these populations can be observed. The system shows interesting non-classical properties like quantum noise reduction below the standard quantum limit for the corresponding coherent spin states [68] that imply underlying phenomena of spin squeezing and entanglement [67]. Applying sub shot-noise Faraday rotation spectroscopy could increase signal to noise ratio of the observed spin fluctuations opening new possibilities in the area.

Moreover, interesting spin-related phenomena arise in BEC phase transitions. Kawaguchi et. al. [69] reports that spin coherences between thermal atoms in different magnetic sublevels develops via coherent collisions with the condensed atoms and determines the phase diagram. Another technique that benefits from applying squeezed light is Faraday rotation spectroscopy, which can be applied for cold-atoms magnetometry [70].

## 5.2 Sub-shot noise magnetization measurement

The objective is to measure the magnetization of the BEC, which we define as the projection of the total angular momentum operator $\hat{F}$ of the atomic ensemble (sum of contributions from all the atoms $\Sigma_{i=1}^{\infty} f_i$) on the quantization axis $z$. Let's introduce the set of pseudo-spin operators that describe the $|m_F\rangle = |\pm 1\rangle$ states:

$$\hat{J}_x = \frac{1}{2}\Sigma_{i=1}^{\infty}[|-1\rangle\langle 1| + |1\rangle\langle -1|]_i \tag{5.2}$$

$$\hat{J}_y = \frac{1}{2}\Sigma_{i=1}^{\infty}[|-1\rangle\langle 1| - |1\rangle\langle -1|]_i \tag{5.3}$$

$$\hat{J}_z = \frac{1}{2}\Sigma_{i=1}^{\infty}[|1\rangle\langle 1| - |-1\rangle\langle -1|]_i \tag{5.4}$$

We do not include in this description the states with $|m_F\rangle = |0\rangle$, since they do not contribute any magnetization along z axis $\langle \hat{F}_z \rangle$. Note that $\hat{F}_z = 2\hat{J}_z$. This description is analogous to Stokes operators $\hat{S}$ that we use to describe polarization of light, and will later facilitate pointing out the symmetry of the light-atoms interaction.

The Stokes operators are defined in terms of creation/anihilation operators in vertically and horizontally polarized mode $a_V$ and $a_H$:

$$\hat{S}_0 = (a_H^{\dagger} a_H + a_V^{\dagger} a_V)/2 \tag{5.5}$$

$$\hat{S}_x = (a_H^\dagger a_H - a_V^\dagger a_V)/2 \tag{5.6}$$

$$\hat{S}_y = (a_H^\dagger a_V + a_V^\dagger a_H)/2 \tag{5.7}$$

$$\hat{S}_z = -i[\hat{S}_x, \hat{S}_y] \tag{5.8}$$

The hamiltonian of the off-resonant interaction of light with the atomic ensemble can be described by the following expression derived in [71]:

$$\hat{H}_{\text{int}} = a\hat{J}_z\hat{S}_z + b(\hat{J}_x\hat{S}_x + \hat{J}_y\hat{S}_y) \tag{5.9}$$

where $a$ and $b$ are constants. The evolution of any operator concerning light or atoms because of $\hat{H}_{\text{int}}$ (to first order in evolution time $\tau$) in the interaction picture has the form:

$$\hat{O}^{(\text{out})} = \hat{O}^{(\text{in})} + \frac{\tau}{i\hbar}[\hat{O}^{(\text{out})}, \hat{H}_{\text{int}}] \tag{5.10}$$

Note this implies the equation (5.1). We obtain input-output relation for the relevant operators:

$$\begin{pmatrix} \hat{S}_x^{(\text{out})} \\ \hat{S}_y^{(\text{out})} \\ \hat{S}_z^{(\text{out})} \end{pmatrix} = \begin{pmatrix} 1 & -a\hat{J}_z^{(\text{in})} & b\hat{J}_y^{(\text{in})} \\ a\hat{J}_z^{(\text{in})} & 1 & -b\hat{J}_x^{(\text{in})} \\ -b\hat{J}_y^{(\text{in})} & b\hat{J}_x^{(\text{in})} & 1 \end{pmatrix} \begin{pmatrix} \hat{S}_x^{(\text{in})} \\ \hat{S}_y^{(\text{in})} \\ \hat{S}_z^{(\text{in})} \end{pmatrix} \tag{5.11}$$

$$\begin{pmatrix} \hat{J}_x^{(\text{out})} \\ \hat{J}_y^{(\text{out})} \\ \hat{J}_z^{(\text{out})} \end{pmatrix} = \begin{pmatrix} 1 & -a\hat{S}_z^{(\text{in})} & b\hat{S}_y^{(\text{in})} \\ a\hat{S}_z^{(\text{in})} & 1 & -b\hat{S}_x^{(\text{in})} \\ -b\hat{S}_y^{(\text{in})} & b\hat{S}_x^{(\text{in})} & 1 \end{pmatrix} \begin{pmatrix} \hat{J}_x^{(\text{in})} \\ \hat{J}_y^{(\text{in})} \\ \hat{J}_z^{(\text{in})} \end{pmatrix} \tag{5.12}$$

We propose to send through the atomic cloud $N_L$ photons of horizontally polarized light (see Fig. 5.1):

$$\langle[\hat{S}_x^{(\text{in})}, \hat{S}_y^{(\text{in})}, \hat{S}_z^{(\text{in})}]\rangle = [N_L/2, 0, 0] \tag{5.13}$$

squeezed in $\hat{S}_y$ so that $\text{var}\big(\hat{S}_y^{(in)}\big) < \frac{1}{2}\langle\hat{S}_x^{(\text{in})}\rangle$ [72]. The interaction with

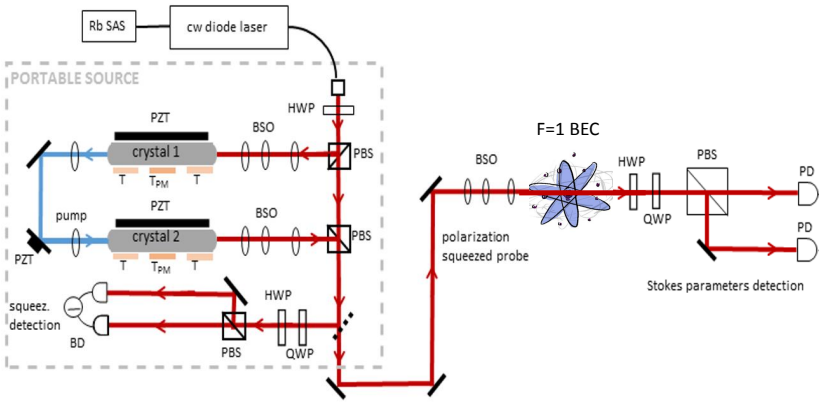


**Figure 5.1:** A portable squeezed light source applied to Faraday probing of a BEC. PBS - polarization beam splitter, BSO - beam shaping optics, BD - balanced detector, HWP (QWP)- half (quarter) waveplate, PZT - piezoelectrical element, PD - photodetector. The squeezed light source is a monolithic OPO as described in 5.5. In addition, the same device with input and output reversed is used as an upconverter to generate pump beam for the OPO.

atoms rotates the polarization about the $z$ axis (first term of the hamiltonian in eq. (5.9), so that it acquires a small nonzero $\hat{S}_y$ component. In order to determine the magnetization, a measurement of Stokes parameter $\hat{S}_y^{(\mathrm{out})}$ is performed.

$$\langle \hat{S}_y^{(\mathrm{out})} \rangle = \frac{aN_L}{2} \langle \hat{J}_z^{(\mathrm{in})} \rangle \tag{5.14}$$

Noise of the measured variable:

$$\mathrm{var}\left(\hat{S}_y^{(\mathrm{out})}\right) = \mathrm{var}\left(\hat{S}_y^{(\mathrm{in})}\right) + a^2 \mathrm{var}\left(\hat{J}_z^{(\mathrm{in})} \hat{S}_x^{(\mathrm{in})}\right) + b^2 \langle \hat{J}_x^{(\mathrm{in})} \rangle^2 \mathrm{var}\left(\hat{S}_z^{(\mathrm{in})}\right) \tag{5.15}$$

It is evident that application of squeezed light improves signal to noise ratio, reducing the noise component $\mathrm{var}\left(\hat{S}_y^{(\mathrm{in})}\right)$, which is the largest noise

contribution in Eq. (9.4) if small spin rotations are considered.

Because of the symmetry of the hamiltonian, the interaction with light also modifies the state of the atoms, causing the rotation of the spins about the $x$ axis.

$$\langle \hat{J}_z^{(\mathrm{out})} \rangle = \frac{bN_L}{2} \langle \hat{J}_y^{(\mathrm{in})} \rangle \tag{5.16}$$

With the application of squeezed light this effect is reduced as well, since we can use fewer photons $N_L$ than we would need to use with a coherent probe in order to achieve the same signal to noise ratio.

The scheme described above can be applied to measure an external magnetic field $B_x$ perpendicular to the probe beam that causes the spins prepared initially to point along $x$ axis to precess and acquire small component along $z$ (magnetization). This value can be measured with high sensitivity with the strategy described above and used to retrieve the amplitude of the magnetic field.

## 5.3 Polarization squeezing

An essential part of the proposed experiment is a robust, stable, high-purity, and strongly-squeezed in polarization quantum light source. One can achieve this combining a quadrature-squeezed vertically-polarized light (output of type-0 OPO) with a horizontally-polarized coherent state to achieve a state squeezed in one of the Stokes parameters.

An OPO pumped below threshold with a coherent beam generates a vertically-polarized state $\rho_{\mathrm{r}}$ quadrature-squeezed with amplitude $r$ in the form of Eq. (2.8) described in section 9.5. It can be converted into a polarization-squeezed state $\rho_{\mathrm{PS}}$ by combining it with a horizontally polarized coherent state $\rho_\alpha$ on a polarization beam splitter [73] (Figure 5.2):

$$\rho_{\mathrm{PS}} = \rho_\alpha \otimes \rho_{\mathrm{r}} \tag{5.17}$$

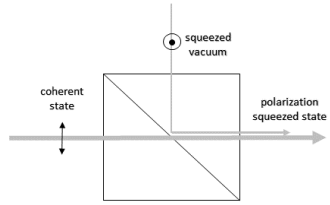


**Figure 5.2:** Generating polarization-squeezed light with the use of a polarizing beam splitter.

where the first subspace describes horizontal polarization and the second vertical.

$$\rho_\alpha = |\alpha\rangle\langle\alpha| \tag{5.18}$$

The Stokes parameter definitions in Eqs. (5.6) to (5.8) imply uncertainty relations for the Stokes operators

$$\mathrm{var}(\hat{S}_i^2)\mathrm{var}(\hat{S}_j^2) \geq \frac{1}{4}\langle\hat{S}_k^2\rangle \tag{5.19}$$

where $i, j, k$ are permutations of $x, y, z$. Expectation values and variances of Stokes parameters for the state $\rho_{\mathrm{PS}}$ are found in [74]. The variance of the lower-noise variable ($\hat{S}_y$ in our case) yields $\mathrm{var}(\hat{S}_y) < \frac{1}{2}\langle\hat{S}_x\rangle$, so by Wineland criterion [75] the state is squeezed for $r > 0$.

## 5.4 Comparison of different squeezer designs

The OPO cavity parameters are a crucial when designing a squeezer, as they determine mode structure of the output, as well as bandwidth and magnitude of squeezing. One important consideration is which beams are resonated. For degenerate OPOs as we discuss here, it is possible to resonate one or both of the pump and the degenerate signal/idler beams. Additionally, different designs determine tunability of the wavelength of

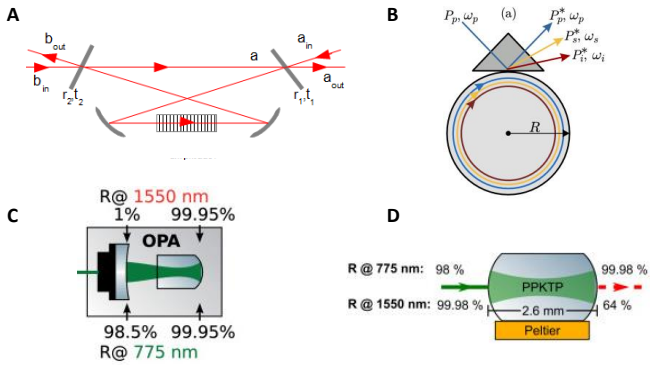


**Figure 5.3:** Different OPO architectures: A - external cavity OPO, B-whispering gallery resonator based OPO (picture adapted from [76]), C-semi-monolithic OPO (picture adapted from [77]) and D - monolithic OPO (picture from [78])

the OPO output (very important for atomic experiments), as well as differ in size, robustness and amount of maintenance they require.

One common design uses an OPO based on external ring cavity around a nonlinear crystal (as in [53]) is shown in Fig. 5.3A. The main disadvantage of this design is high intracavity loss, caused by the interfaces (crystal and mirrors) inside the cavity that always have imperfect coatings. Moreover, it is more sensitive to vibration and unstable compared to monolithic designs. Ring cavity design implies that the downconversion occurs only once per roundtrip, not twice like in Fabry-Perot cavities, which is both disadvantage (lower gain per roundtrip) and advantage (no need of controlling phase between light downconverted on two consecutive passes through the nonlinear medium, see section 7.1). What is more, ring cavity allows us to have an auxiliary locking beam conterpropagating with respect to downconverted light, convenient for cavity stabilization. Another advantage of external ring cavity is tunability to atomic resonance, which requires only mounting one of the mirrors on

the piezoelectric actuator in order to be able to adjust cavity length.

Whispering gallery resonators (Fig. 5.3 B) offer very low intracavity loss due to lack of interfaces [79], but they tend to be high-maintenance due to in and out coupling mechanism requiring precision of positioning the prism relative to the cavity. What is more, they are very sensitive to dirt, which causes light to leak out of the cavity.

Monolithic cavities (Fig. 5.3 D) are nonlinear crystals polished and coated so that it form a linear cavity. This design has the advantage of being stable, robust, compact and insensitive to vibration. Since coatings on the crystal are not exposed to focused high power pump light inside of the cavity, they do not deteriorate due to dirt as in the external cavities case. However, it is impossible to choose the optimum spot on the crystal where the downconversion occurs which might play a role for some wavelengths for which fabricating high-quality poling difficult. Monolithic designs are also more challenging to tune, because the cavity-length cannot simply be controlled with a piezo-element. Temperature tuning can play this role, but may simultaneously affect phase matching, which also depends on the crystal temperature.

Semi-monolithic designs (Fig. 5.3 C) are a trade-off between external cavity and monolithic designs, in which a Fabry-Perot cavity is formed between a spherical mirror and plano-convex polished nonlinear material. Sensitivity to vibration and intracavity loss are increased in exchange for possibility of tuning the cavity via the external mirror. This is the design that produces the most squeezing (it is to be incorporated in the GEO600 gravitational wave detector [80]).

The OPO design we propose is a monolithic design with three separately-controlled temperature sections, allowing independent control of phase matching as well as double resonance.

## 5.5 A tunable doubly-resonant monolithic squeezer

Employing squeezed light in metrology enables us to perform sub shot-noise measurements using the variable with reduced (squeezed) noise. However, conventional squeezed light sources are complex, unstable and hard to use, as opposed to monolithic squeezers, which are more robust, compact and easy to incorporate into more sophisticated experiments. A monolithic OPO was first demonstrated in Roman Schnabel's group in 2007, with a purpose to suppress the shot noise for an interferometric gravitational wave detector GEO600. They developed a monolithic source without wavelength tunability producing 10 dB-squeezed vacuum at 1550 nm [81, 78]. Another realisation of the idea was implemented by the group of Akira Furusawa [42], with a view to use it in continuous-variable quantum information experiments that require simultaneously a large number of highly squeezed beams. Their design was a resonator tunable at the cost of compromising the phase matching and they achieved 8 dB of squeezing at 860 nm.

However, neither of these sources has been designed with a purpose of applying it for probing atomic ensembles, since the emitted squeezed light was not resonant with any transitions of alkali atoms, as opposed to the design we propose. What is more, our source will be also enhanced by double resonance and offer wavelength tunability within the Rb $D_1$ resonance.

The OPO design we propose consists of a crystal of Rb-doped potassium titanyl phosphate (RKTP), spherically polished and coated at the ends, so that it forms a Fabry-Perot cavity as shown in figure 5.4. The crystal is divided into three sections (see Fig. 5.4): two non-poled (linear) sections and the periodically-poled central part. The pump is focused in central section (maintained in the phase-matching temperature) where the parametric interaction occurs, whereas the linear sections of the crystal are used for tuning the cavity.

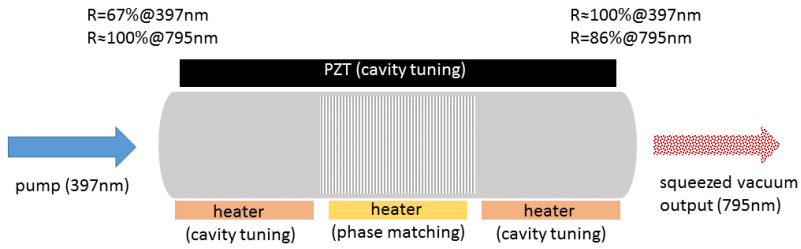


**Figure 5.4:** A doubly resonant monolithic squeezer, tunable using three temperatures and one strain degrees of freedom.

The objective is to have the cavity resonant not only for the squeezed vacuum beam (at half of the pump frequency), but also for the pump beam. We also need to be able to tune the squeezed beam frequency. Therefore, since we need to have the cavity resonant for two different arbitrary wavelengths, we need to use two independent degrees of freedom. In addition to that, the phase between forward and backward interacting light needs to be controlled to ensure constructive interference, and quasi phase matching condition needs to be fulfilled. All of the above mentioned amount to four conditions, and we are able to control them independently using three temperature and one pressure controls.

Although monolithic sources have already been reported [81, 42], the design we propose is the first one with pump resonance and that will offer wavalength tunablility.

# Chapter 6

# Monolithic cavity design

This chapter describes the material and geometry of the monolithic cavity, designed to enhance conversion between rubidium $D_1$ resonant light at 795 nm and near UV-wavelength of 397 nm with high efficiency and fine-tuning capabilities. For simplicity, we refer to 795 nm and 397 nm light as red and blue respectively. The geometric design is a trade-off between mode shape that is optimal for the downconversion efficiency and technical limitations in polishing the cavity. We also present the detailed design of the cavity holder that enables us to independently stabilize the temperatures of the three sections of the crystal while pressing it with the piezoelectric actuator for the purpose of cavity tuning.

Here we take advantage of the quasi-phase matching (QPM) technique, which allows us to exploit the highest nonlinearity available in the material in a non-critical phase-matching scheme, achieving higher conversion efficiencies, compared to birefringent phase matching setups. The crystal is fabricated out of a material best-suited for short-period periodic poling, Rb-doped potassium titanyl phosphate (RKTP), engineered by our collaborators at KTH Royal Institute of Technology in Stockholm.

After fabrication and periodic poling, the crystal was spherically polished and coated by Photon Laseroptik GmBH. The geometrical dimensions (cavity length 16 mm, active section length 7 mm and curvature radii of 10.7 mm) were designed as a trade-off between optimal nonlin-

ear interaction [82] and technical ease of spherical polishing of the facets of the crystal, the main practical limitation being avoiding the possibility of misaligned cavity due to the error in the position of the centers of the spherical surfaces which form the mirrors of the sides of the crystal.

The oven that holds the crystal, described in Section 6.4 requires an apparatus that allows applying large pressure to the crystal without damaging it, simultaneously with precise heating of its sections. Since using the dimension perpendicular to the force applied to the crystal by the piezo actuator proved impossible (due to large thermal gradients inside the crystal), the heating devices we use need to be very flat, in order not to cause the crystal pressed against it to break.

## 6.1 Material

Frequency conversion between near-IR and near-UV spectral ranges requires QPM structures with periodicities of the order of few micrometers, which still remains challenging. Although periodically-poled KTP displays one of the highest nonlinear coefficients via noncritical quasi phase-matching, and has been successfully employed to build highly efficient SPDC pair sources at 810 nm [83], the periodic poling quality necessary to generate photons at 795 nm is often not satisfactory. Bulk Rb-doped KTP is an ideal candidate for production of such fine-pitch QPM structures. A low Rb+ dopant concentration (typically below 1%) essentially guarantees same RKTP optical properties as those of regular flux-grown KTP, however, two orders of magnitude lower ionic conductivity mitigates the domain broadening problem and allows us to achieve periodic poling of high-quality ferroelectric domain structures [84]. In addition, this material exhibits lower susceptibility to gray-tracking benefiting the applications in near-UV spectral region. For our experiment we have used periodically poled RKTP (PPRKTP) crystals

with the QPM period of $\Lambda = 3.16$ μm, fabricated by our collaborators Carlota Canalias and Andrius Zukauskas at KTH Stockholm.

High-quality periodic poling of the active section located in the central part of the crystals (approx. poling volume: 7 mm × 3.5 mm × 1 mm along the a, b, and c axes, respectively) was achieved using the short-pulse electric field poling technique [85].

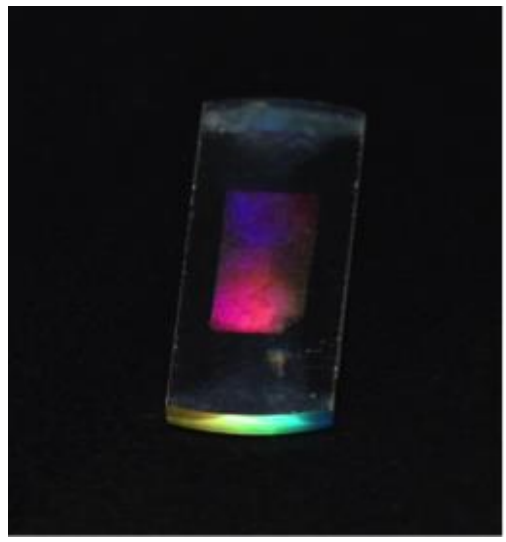

**Figure 6.1:** A photo (by K.Kutluer) of the crystal used in the experiment with the periodically-poled section visible.

## 6.2 Cavity design

### 6.2.1 Dimensions

The maximum crystal thickness ($d = 1$ mm) is limited by the periodic poling, which was not technically possible for thicker crystals. The other

dimensions, being the length $L = 16$ mm and the width (6mm) of the crystal were chosen for convenient fabrication and handling.

The lengths of non-poled sections are important, as they determine the cavity tuning capabilities. Since we maintain these sections at a temperature different from the poled section (which is always at the phase matching temperature), the objective is to have the side sections long enough, so that we can tune the cavity by at least one FSR without causing significant temperature gradient in the crystal, which could compromise the frequency conversion efficiency. We estimated that for the side section of the length 3.5 mm the necessary temperature tuning range would require less than 1K difference between central and side sections of the crystal, which is not expected to cause thermal gradient problems.

The crucial part of the cavity design was selecting the radii of curvature of the sides of the crystal, which determine the beam waist inside of the crystal. We decided to use a symmetrical cavity design, as we need two equal length non-poled sections on the sides of the central active section. For the gaussian beam, the waist of the mode supported by the cavity can be calculated from the curvature of the mirrors, as this curvature is equal to the curvature of the waveform of the gaussian mode supported by the cavity.

### 6.2.2 Formulas describing a gaussian beam

In this subsection we enumerate the basic formulas necessary the design, that describe a Gaussian beam in a dielectric medium with refractive index $n = 1.85$ and vacuum wavelength $\lambda = 795$ nm.

The radius of curvature of the gaussian beam characterized by a Rayleigh range $z_R$ as a function of distance $z$ from waist has the following form:

$$R(z) = z\left(1 + \left(\frac{z_R}{z}\right)^2\right). \tag{6.1}$$

The Rayleigh range in turn is related to the beam waist $w_0$ as follows:

$$z_R = \frac{w_0^2 \pi n}{\lambda}. \tag{6.2}$$

The beam width $w(z)$ changes with distance according to

$$w(z) = w_0 \sqrt{1 + \left(\frac{z}{z_R}\right)^2}. \tag{6.3}$$

We can calculate the beam size on the side of the crystal from the above formula taking $z = L/2$.

### 6.2.3 Optimum focusing

Boyd and Kleinmann [82] calculate the efficiency of the frequency conversion for a gaussian beam in the $\chi^{(2)}$ medium to be proportional to the function

$$h(\xi, \sigma) = \frac{1}{2\sqrt{\pi}\xi} \int_{-\infty}^{\infty} e^{4s^2} \left| \int_{-\xi}^{\xi} \frac{e^{i\sigma\tau}}{1 + i\tau} d\tau \right|^2 ds \tag{6.4}$$

where $\sigma$ is proportional to phase mismatch $\Delta k$, and

$$\xi = \frac{L_a}{b} \tag{6.5}$$

where $b = 2z_R$ is the confocal parameter of the gaussian beam. The function $h(\xi, \sigma)$ reflects the trade-off between the two factors that become more prominent with tighter focusing, namely high intensity in the focus beneficial for the nonlinear process, and large divergence which causes

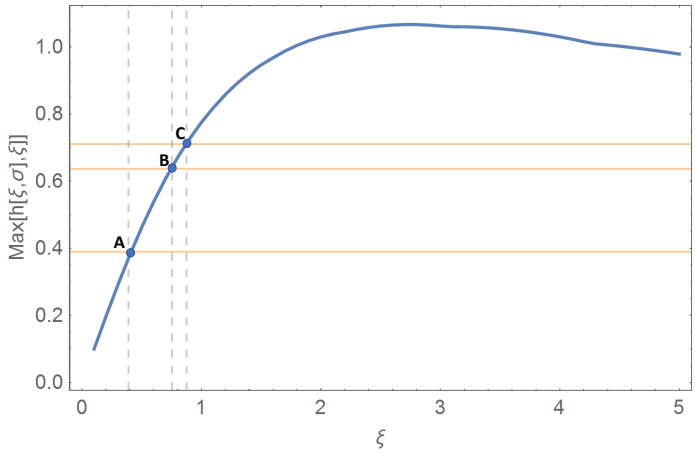


**Figure 6.2:** Plot of function $h(\xi,\sigma)$ maximized over phase mismatch $\sigma$. Point A corresponds to external-cavity OPO described in [53], point B with $\xi = 0.752$ represents our design of a monolithic cavity, and point C the scenario described in the section 6.2.4.

the inefficient use of the crystal. They find an optimum ratio between a confocal parameter $b$ of the beam and the length of the active section of the crystal $L_a$ to be $\xi = 2.84$ (see Fig. 6.2), which corresponds to the waist in the crystal equal to:

$$w_{\text{opt}} = \sqrt{\frac{L_a \lambda}{(2.84)2\pi n}}. \tag{6.6}$$

For our monolithic cavity characterized by the poled section length $L_a =$ 7 mm the optimum waist equals to 13 µm. However, the maximum of $h(\xi,\sigma)$ is rather broad and in consequence, other factors come into play when determining the appropriate focusing, such as thermal lensing and damage that might be caused to the crystal exposed to high intensity, like gray-tracking or BLIIRA (blue light induced infrared absorption) [86]. Apart from that, in case of a monolithic cavity there is a technical

limitation that impedes strong focusing, which is described in the next subsection.

### 6.2.4 Polishing limitations

An external-cavity based OPO offers the possibility of adjusting the tilt and the position of the mirrors in order to ensure the cavity is well-aligned. However, when monolithic cavities are considered the task of cavity alignment falls entirely into the hands of the polisher.

The most important issue in our case was an error in the position of the centers of spherical surfaces that constitute the mirrors at the sides of the crystal, which was guaranteed to be below 0.1 mm. From simple geometric considerations we know that propagation direction of the gaussian mode supported by the cavity coincides with the line connecting the two centres of the spheres (green and blue point in Fig. 6.3). If these centres are off the axis of the crystal, it is possible that part of the beam does not hit the facet of the crystal (that is 1 mm $\times$ 6 mm).

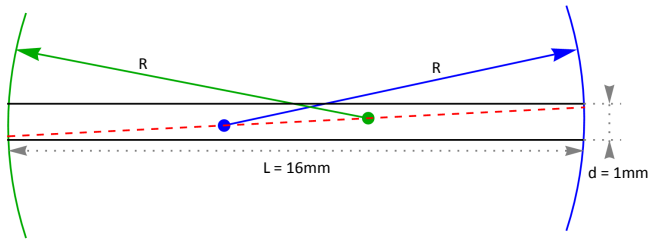


**Figure 6.3:** Scheme of the geometry of the cavity in the worst case scenario when the centres of the spherical surfaces of radius $R$ are displaced in opposite directions.

Let us consider the worst scenario when two centres of mirror curvatures

are off by 0.1 mm in opposite directions, shown in Fig. 6.3. The propagation direction of the gaussian mode supported by the cavity is set by these two curvature centre points (red dashed line). The displacement (with respect to the centre of the facet of the crystal) of the beam centre on the mirror for crystal length $L = 16$ mm and radius of curvature $R = 10.7$ mm yields 0.3 mm.

Beam waist at $z = 8$ mm (at the mirror) is equal to 50 μm, so even in the worst case the beam is still not touching the edge of the crystal (being closer than 0.5 mm from the centre of the facet).

If we decrease the radius of curvature to 10 mm the displacement of the beam centre and beam waist are 0.4 mm and 52 μm respectively. This scenario is more risky, especially if we consider that the edges of the crystals after polishing tend to have small chips. This radius change would give us tighter focusing ($\xi$ would be equal to 0.875 instead of 0.752, see point C in Fig. 6.2), which means that we would get a small advantage (11% more) in the nonlinear efficiency due to being closer to the optimal focusing, but at the cost of risking that the cavity is misaligned.

To summarize, we choose to polish the mirrors with the radius of 10.7 mm in order to be as close as possible to optimum focusing without compromising the cavity alignment due to geometric errors in polishing.

### 6.2.5 Coatings

The coating of the input of the monolithic OPO (or output of the SHG device) is almost totally reflective ($R > 99.99\%$) for the fundamental wavelength of 795 nm, and partially reflective for the 397 nm pump. As we estimate the pump roundtrip loss to be 31%, the pump reflectivity is equal to 69% to achieve critical coupling, which corresponds to maximum power build-up in the cavity.

The OPO output (SHG input), in turn, is almost completely reflective for the pump, and has a reflectivity of 84% for 795 nm. The red reflectivity is selected so that to ensure a high cavity escape efficiency (close to 95%), which increases the amount of squeezing achievable with the system. The roundtrip loss for the red is estimated to be less than 1%.

The cavity finesse yields 20.5 for the red and 8.4 for the blue.

## 6.3 Degenerate cavities

In this section we describe an interesting property of our monolithic cavity, which is a consequence the fact that the ratio between the radius of the mirrors and cavity length is almost exactly $\frac{2}{3}$.

Ray transfer matrix analysis (ABCD matrices) is a ray tracing technique used to design optical systems to which paraxial approximation can be applied (all rays are at a small angle and small distance relative to the optical axis of the system). In addition, the same formalism can also be used to calculate the propagation of gaussian beams through a similar system. Propagation of the beam through a two-mirror cavity roundtrip in terms of ABCD matrices yields:

$$M_{\mathrm{ABCD}}(L,R) = \begin{pmatrix} 1 & L \\ 0 & 1 \end{pmatrix} \begin{pmatrix} 1 & 0 \\ -2R^{-1} & 1 \end{pmatrix} \begin{pmatrix} 1 & L \\ 0 & 1 \end{pmatrix} \begin{pmatrix} 1 & 0 \\ -2R^{-1} & 1 \end{pmatrix} \quad (6.7)$$

Where $L$ is the cavity length and $R$ is the radius of both mirrors.

Calculating the roundtrip matrix $M_{\mathrm{ABCD}}$ for a confocal cavity (when $L = R$) we arrive to

$$M_{\mathrm{ABCD}}(L,L) = \begin{pmatrix} -1 & 0 \\ 0 & -1 \end{pmatrix}. \quad (6.8)$$

Note that the square of $M_{\mathrm{ABCD}}(L,L)$ is an identity matrix. The consequence of this fact is that any beam (also not mode-matched to cavity)

after two roundtrips has the same angle and position relative to cavity optical axis as when entering the cavity, and therefore it interferes with itself.

Accidentally, in our cavity we have $R = \frac{2}{3}L$, and for these values

$$\left[M_{\mathrm{ABCD}}\left(L, \frac{2}{3}L\right)\right]^3 = \begin{pmatrix} 1 & 0 \\ 0 & 1 \end{pmatrix} \tag{6.9}$$

It means that the a ray injected into a cavity no matter at what angle and position reproduces itself after three cavity roundtrips, provided that the angle is not too big (so that the beam reaches the output facet of the crystal). After initial confusion, this property turned out to be useful in cavity alignment with the help of a CCD camera imaging the cavity output plane. The image for misaligned cavity consists of three spots, and the right alignment of angle and position of the input beam is obtained when the three spots join into one, whereas the beam size and focusing is matched the the cavity mode when the three spots are the same size.

## 6.4 Oven design

In this section we describe the design of the crystal holder (oven), responsible for applying the pressure to the crystal as well as maintaining its three sections in their respective temperatures.

The schematic drawing of the oven is shown in Fig. 6.4. The inner oven consists of two polished glass plates (marked as elements 4 and 5 in Fig. 6.4A) pressed together by a piezoelectric actuator; the crystal is placed in between them. The lower plate rests on an aluminum support (element 2) which is rigidly connected to also aluminum upper support (element 1) that allows the piezoelectric actuator to apply pressure to the crystal and upper and lower plates. The lower plate (see Fig. 6.5 A and B and 6.6)

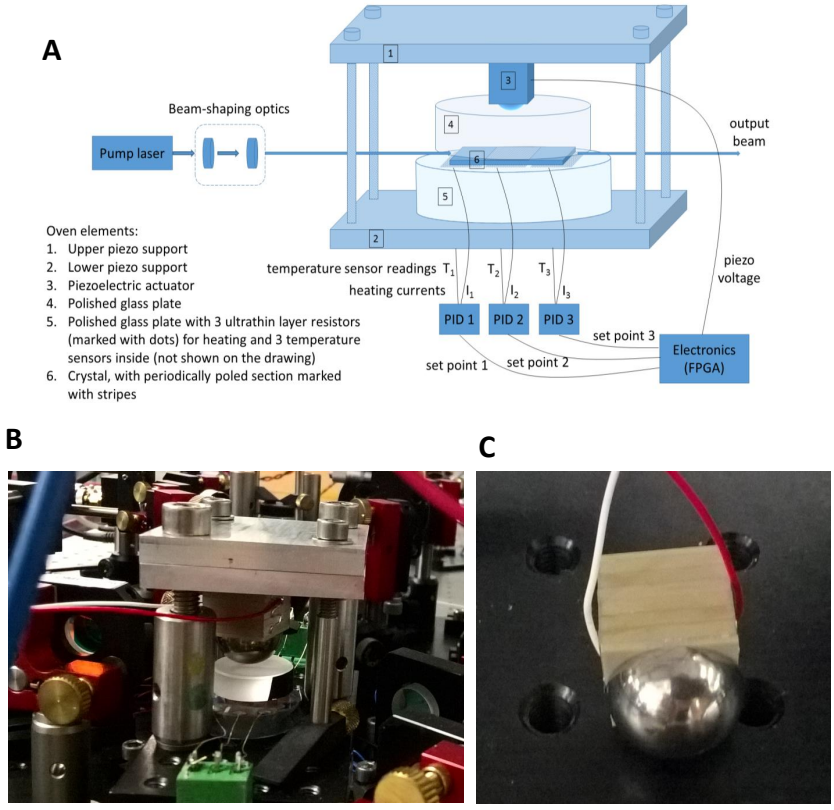


**Figure 6.4:** An illustration of the oven design. **A:** Oven with marked elements described in the figure. **B:** A photo of the assembled oven. **C:** A photo of the piezoelectric actuator (Noliac NA2023) with half-sphere end piece.

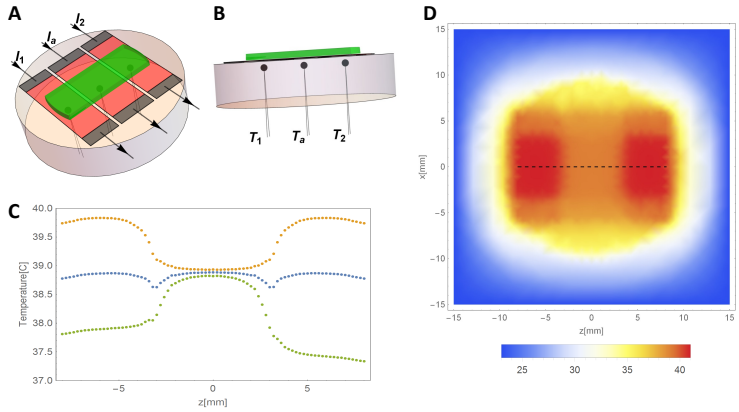


**Figure 6.5:** An analysis of the thermal gradients inside the crystal. **A:** The lower plate with crystal (green) resting on top of it. $I_1$, $I_2$ and $I_a$ denominate currents flowing through the corresponding ITO heaters (red) and nickel electrodes (black) **B:** Side view of the lower plate, showing temperature sensors **C:** Typical temperature distributions an the crystal axis calculated from FEM model for sensor temperatures $T_1 =$ 38C and $T_2 = 37.5$C (green), $T_1 = T_2 = 40$C (orange), $T_1 = T_2 = 39$C (blue). For all three $T_a = 39$C. **D:** Example temperature distribution on the plane containing the crystal optical axis (dashed line) from FEM.

is responsible for maintaining each of the three sections of the crystal in its respective temperatures, whereas the upper plate is used for evenly distributing the stress from the piezoelectric actuator that presses the crystal from above.

The lower plate is a 25.4 mm diameter and 6 mm thick mirror blank, with three 100 nm thick ITO (indium tin oxide) stripes deposited using sputtering (AJA International ATC Orion 8 HV). Substrate-target distance was set to 30 cm, Ar (20 sccm) and $O_2$ (1 sccm) were used for sputtering with a pressure of 2 mTorr. The crystal, resting on polished glass with thin film ITO stripes, is heated when current is applied to the stripes through nickel electrical contacts deposited on each stripe.

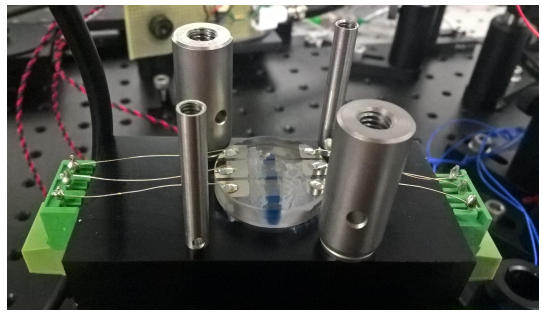

**Figure 6.6:** A photo of the oven. The crystals (not present in the photo) rests on top of the glass plate, and the three semi-transparent stripes are responsible for heating its three sections.

Measurement of the temperature is performed using thermistor sensors, placed inside the lower plate 1mm from the surface with ITO heaters in small holes drilled in the lower plate from the side opposite the crystal. The temperature of each section of the crystal is PID stabilized by feeding back from the sensor to the heater current. To understand the thermal conditions, a finite element method (FEM) model was developed in Mathematica, solving the 3D heat diffusion equation. The temperatures of the ITO stripes (Dirichlet condition) are varied and for each case the relation between temperatures of the sensors inside the lower plate and temperature of the optical axis of the crystal $T(z)$ is found (see Figs. 6.5C and 6.5D). The theory results compared against the experiment in the next chapter use the temperature distribution from this model and the measured temperatures $T_1$ and $T_2$ are treated as sensor temperatures.

The upper plate is a 19 mm diameter and 6 mm thick mirror blank, pressed by a piezeoelectric actuator terminated in a steel half-sphere (see Fig. 6.4C), to simplify alignment and prevent strain concentration due to tilt of the actuator relative to the crystal. Using thin heaters (100 nm, comparable to the $\sim \lambda/10$ surface flatness of the mirror substrates upon which they are deposited) is necessary to minimize shear stresses on the

crystal under compression, which otherwise can break.

# Chapter 7

# Second harmonic generation with the monolith

In this chapter we demonstrate tunability features of our monolithic device, which include up to four tuning degrees of freedom, three temperature and one strain, allowing resonance of pump and generated wavelengths simultaneous with optimal phase-matching. We test the performance of the monolithic device as an upconverter, demonstrating efficient continuous-wave second harmonic generation from 795 nm to 397 nm, with low-power efficiency of 72 %/W and high-power slope efficiency of 4.5 %. We observe optical bistability effects, and show how they can be used to improve the stability of the output against pump frequency and amplitude variations.

We dedicate this entire chapter to second harmonic generation, because apart from being for a useful step for learning how to drive the monolithic device, it is also important as technological advance. The near-UV or UVA wavelengths 315 nm to 400 nm have numerous applications, for example in biology, where fluorescent bio-markers are excited at short wavelengths, often below the range of diode lasers. Although gas lasers can directly generate UVA at selected wavelengths, compact and efficient sources require frequency up-conversion, for example by intra-cavity doubling in diode-pumped solid-state (DPSS) lasers. Due

to the high intra-cavity intensities and sensitivity of laser resonators to intra-cavity losses, such systems are sensitive to degradation of bulk crystal properties and surface properties under intense UV illumination. Here we explore an alternative route to compact, stable UVA generation, using diode-pumped monolithic frequency converters. This approach is attractive for a number of reasons, not least the absence of intra-cavity interfaces and the stability against environmental perturbations including vibration, pressure and temperature fluctuations, and chemical or physical contamination.

We present a monolithic frequency converter with temperature control of the periodically-poled central region of the crystal, and additionally independent temperature control of two end sections, as well as strain tuning by compressing the cavity/crystal with a piezo-electric element. We observe that thermo-optical tuning can cover multiple cavity free spectral ranges (FSR) without compromising the phase matching due to thermal gradients in the poled section, and moreover the ratios between elastooptical and thermooptical coefficients for 795 nm and 397 nm differ enough that we can independently control the fundamental and SHG resonances. Together, these provide four independent controls, allowing us to optimize the pump resonance, phase matching, second harmonic resonance, and phase relation between forward- and backward-propagating SHG, without using the pump wavelength as a degree of freedom.

## 7.1 SHG efficiency in the cavity

In this section we describe second harmonic generated in a doubly-resonant, lossy, linear cavity, and identify the cavity tuning controls and degrees of freedom that need to be controlled so as to double resonance is maintained.

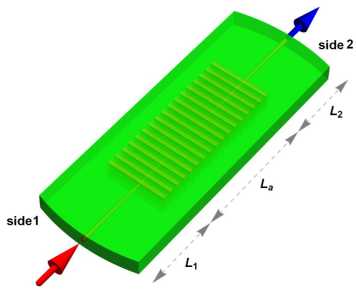


**Figure 7.1:** A crystal with active section with length $L_a$ periodically poled and maintained in phase-matching temperature $T_a$, while sides 1 and 2 with lengths $L_1$ and $L_2$ are in temperatures $T_1$ and $T_2$ respectively. Side 1 has reflection and transmission amplitude coefficients $r_1$ and $t_1$ and side 2 $r_2$ and $t_2$ for the red pump light. Side 1 is assumed to be completely reflective for the blue second harmonic, and $r$ and $t$ stand for the second harmonic reflection and transmission coefficients for side 2.

Following a simple steady-state calculation found in [87] adapted to a cavity design with one active and two side sections as in Fig. 7.1 we obtain the expression for the output SH field $\mathscr{E}_{\text{out}}^{(2\omega)}$ as a function of temperatures $T_1, T_a, T_2$, voltage $V$ and pump amplitude $\mathscr{E}_{\text{in}}^{(\omega)}$.

$$\mathscr{E}_{\text{out}}^{(2\omega)} = \chi_{\text{eff}}^{(2)} J_{\text{blue}} J_{\text{pm}} J_{\text{phase}} J_{\text{red}}^2 (\mathscr{E}_{\text{in}}^{(\omega)})^2 \tag{7.1}$$

where

$$J_{\text{red}} = \frac{t_1}{1 - r_1 r_2 e^{2i(\phi_1^{(\omega)} + \phi_a^{(\omega)} + \phi_2^{(\omega)})}}, \tag{7.2}$$

$$J_{\text{blue}} = \frac{t}{1 - r e^{-2\alpha L} e^{2i(\phi_1^{(2\omega)} + \phi_a^{(2\omega)} + \phi_2^{(2\omega)})}}, \tag{7.3}$$

$$J_{\text{pm}} = e^{i(\phi_a^{(\omega)} - \frac{1}{2}\phi_a^{(2\omega)} - \frac{q}{2})} \text{sinc}\left(\phi_{\text{a}}^{(\omega)} - \frac{1}{2}\phi_{\text{a}}^{(2\omega)} - \frac{1}{2}\text{q}\right), \tag{7.4}$$

$$\chi_{\text{eff}}^{(2)} = \chi^{(2)} e^{-\alpha(L_a + L_2)}, \tag{7.5}$$

$$J_{\text{phase}} = 1 + r_2^2 r e^{-\alpha L} e^{i(2\phi_1^{(2\omega)} + \phi_a^{(2\omega)})} e^{2i(\phi_a^{(\omega)} + 2\phi_2^{(\omega)})}, \tag{7.6}$$

and $J_{\text{red}}$, $J_{\text{blue}}$ are resonance terms with blue absorption coefficient $\alpha$, total cavity length $L$ and $\phi_i^{(\omega)} = \frac{\omega}{c}\int_{L_i} n(\omega, T_i, V)dl$ are the phases accumulated by the field of frequency $\omega$ after passing through each section of the crystal uniformly pressed by applying voltage $V$ to the piezo element, with $i = a$ corresponding to the active, i.e. poled, section and $i = 1,2$ to the side sections 1 and 2. The factor $J_{\text{pm}}$ is a phase matching profile with poling period $\Lambda$, $q \equiv \frac{2\pi}{\Lambda}$, and $\chi^{(2)}$ is the single-pass efficiency. Finally, the factor $J_{\text{phase}}$ describes the effect of interference between the blue field created in backward and forward passes of the pump beam through the active section. Fig. 7.2 shows how the factors behave when the temperature of the entire crystal (all the sections together) is changed.

The phase matching is affected only by the temperature of the active section $T_a$ and voltage $V$, whereas side temperatures $T_1 = T_S + T_D$ and $T_2 = T_S - T_D$ affect both resonances and the interference phase factor. However, the phase degree of freedom can be separated, since changing $T_D$ does not affect to first order the blue and red resonance.

To summarize, in order to maximize the emission from the cavity, in addition to maintaining the active section at the phase matching temperature, we need to have three degrees of freedom to control red and blue resonance and relative phase. We use $T_D$ to control the relative phase, and $T_S$ and the elastooptic effect to control red and blue resonance, taking advantage of the fact that both thermooptic and elastooptic coefficients are different for red and blue.

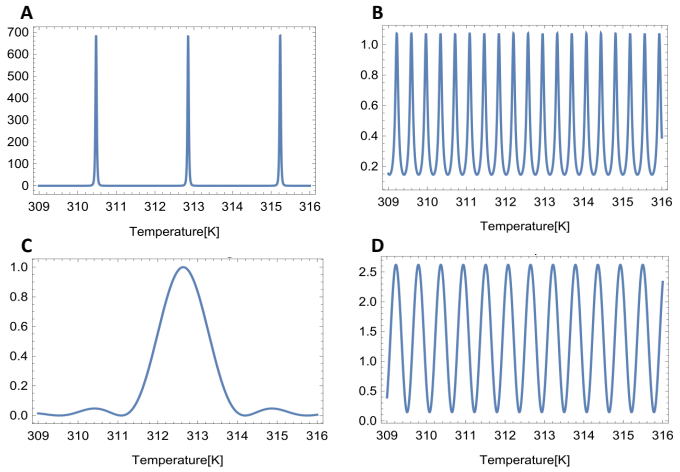


**Figure 7.2:** Factors determining efficiency of SHG, plotted as a functions of the entire crystal temperature (all three sections at the same temperature). **A:** Red resonance factor $J_{\text{red}}$, **B:** Blue resonance factor $J_{\text{blue}}$, **C:** Phase matching factor $J_{\text{pm}}$, **D:** Backward/forward phase factor $J_{\text{phase}}$.

## 7.2 Experimental characterization

The experimental results presented in this section are obtained for a cavity as in as in Fig. 7.1, pumped by a DBR laser at 795 nm, amplified by a tapered amplifier (see Appendix C for details), spatially filtered by a single-mode fiber, and mode matched to the cavity with a set of lenses and mirrors. The signal from the cavity output is split by a dichroic mirror and sent to two detectors recording the power of the red transmitted though the cavity and blue power exiting the cavity (as in Fig. 8.1).

### 7.2.1 Red resonance control via temperature and pressure

In the method we propose, we keep the temperature gradients as small as possible, since they can cause the efficiency to drop because the entire active section is not maintained in the phase matching temperature. Therefore, we start with the entire crystal set to phase matching temperature, and then slightly vary the side temperatures to satisfy the remaining resonance conditions. Red resonance can be controlled using the temperature of the sides of the crystal $T_S$ (it is not sensitive to $T_D$) and pressure. A simple test of tuning red resonance by changing the temperature of one of the sides while the rest of the crystal is maintained at the phase matching temperature showed that the cavity resonance shift is a linear function of the side temperature over a range of a few FSR (more than necessary for the purpose of tuning the cavity), which indicates that the regime where temperature gradients become a limiting factor is not reached. Linear fits with respect to sensor temperature and crystal temperature (from FEM model) give 0.603 $\pm$0.002 FSR/K and 0.442 $\pm$0.001 FSR/K, respectively, where FSR is a cavity free spectral range (5.2 GHz). Straightforward calculation from the Sellmeier equation given in [88] and assuming no thermal gradients predicts 0.416 FSR/K. The possible causes of the small discrepancy are the fact that neither the length of the section nor the sensor location is precisely known, and the FEM model does not include the thermal contact between the crystal and the heaters and the temperature sensor and lower glass plate.

A similar measurement has been performed varying the voltage applied to the piezo actuator (pressing the crystal) while scanning the laser through the cavity spectrum and observing the shift of the cavity resonance frequency. The results are presented in the Fig. 7.3A. This tuning method shows a small hysteresis. The piezo actuator used in the experiment allows us to tune the cavity by an FSR, with the rate of $0.0049 \pm 0.0001$ FSR/V (linear fit), although the precise rate changes each time the piezo

is mounted. We observed that refractive index change due to elastooptical effect can be described as $n_e(\omega,V) = \beta V$ for the fundamental field and $n_e(\omega,V) = (1.75 \pm 0.05)\beta V$ for the second harmonic, where the common factor $\beta$ depends on how the piezo actuator is held and changes from mounting to mounting.

The temperature $T_D$ does not affect the blue and red resonance conditions, therefore we use the $T_S$ and pressure to control them and then adjust the relative phase factor $J_{\text{phase}}$ by $T_D$. Since the red resonance is the most sensitive (narrowband) condition in the experiment, and the elastooptical tuning is the fastest degree of freedom, our strategy is first to lock the red resonance using a feedback from the red transmission signal and then to adjust $T_S$ and $T_D$ until blue resonance is achieved and $J_{\text{phase}}$ optimized while the piezo actuator follows the red resonance.

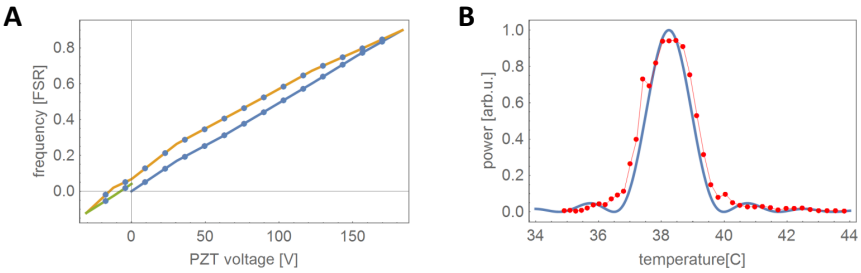


**Figure 7.3: A:** Elastooptic effect based tuning, each data point is the cavity resonance shift recorded from the cavity scan for a given piezo voltage. **B:** Phase matching curve, experimental data and fitted $d_{\text{pm}}(T)$, with the center temperature as a free parameter.

### 7.2.2 Phase matching temperature measurement

The phase matching temperature of the crystal has been experimentally measured by varying temperature of the active section of the crystal and recording the maximum blue power exiting the cavity (separated from the red cavity transmission signal by the dichroic mirror). At each active section temperature corresponding to one data point at Fig.7.3B, the blue power was optimized by two side temperatures adjusted within $\pm 1.5K$ in 10 steps from the center temperature and a laser scanned over 1.5 FSR of the red resonance (replacing elastooptic effect as a control to tune the cavity). Temperatures in this experiment are calculated by FEM model from the sensor temperatures.

### 7.2.3 Controlling blue via temperature

The monolithic frequency converter can be doubly resonant without compromising phase-matching, only by changing independently the temperatures of the sides of the crystal. The figure 7.4 shows SHG power obtained from the cavity as a function of two temperatures of the sides of the crystal $T_1$ and $T_2$ while the central active section is maintained in phase matching temperature of 39°C. It is evident that several maxima are present, so the tuning range offered by our temperature tuning method is more than sufficient to achieve double resonance.

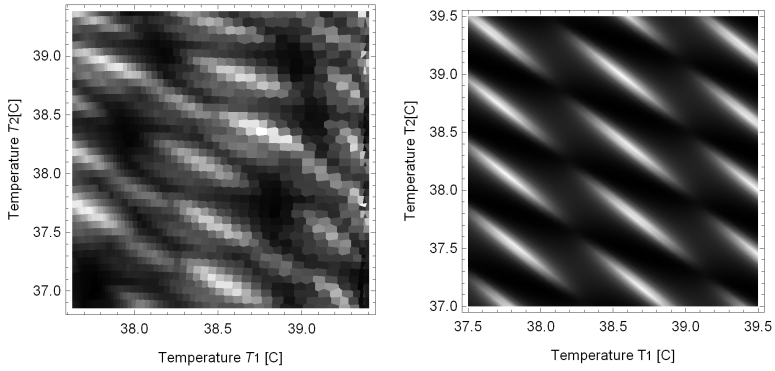


**Figure 7.4:** Blue power for different settings of the side temperatures. Experiment (left) is compared to theory (right) from the first section. Temperature in both plots is sensor temperature (in case of theory calculated from FEM model). Reason for discrepancies is principally that lengths of the side sections are not controlled, and not known precisely.

### 7.2.4 Kerr effect, bistability, and red stabilization

We observe a Kerr effect for the red light, which manifests as a characteristic optical bistability or asymmetric, hysteretic cavity resonance shape. Red resonance shapes as scanned by the piezoelement are shown in the figure 7.5A. The magnitude of the asymmetry increases with the fundamental beam power and the scanning speed, indicating a slow Kerr nonlinearity that will be analyzed in detail in the next chapter. For pump powers of 50mW and higher the observed resonance shapes are independent of the blue resonance condition, suggesting that blue light absorption does not play a significant role in the effect.

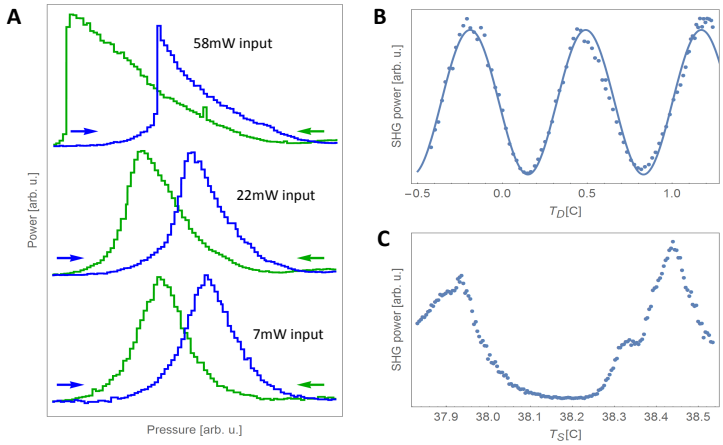


**Figure 7.5:** A bistable resonator behaviour. **A:** Scans by the piezo (15s long) through red resonance for different input power levels. Each plot shows scan decreasing and increasing pressure, according to the arrows. **B:** Measurement of SH power when slowly sweeping $T_D$ and keeping the piezo-based lock running, along with a sinusoidal fit. **C:** Measurement of SH power when slowly sweeping $T_S$ and keeping the piezo-based lock running.

Optical bistability makes it impossible to stabilize the red resonance precisely at the maximum, which occurs adjacent to the transition to the low cavity power condition. On the other hand, by broadening the resonance, the Kerr effect facilitates stabilization near the maximum, and in practice we can easily stabilize the cavity length for the red at least 97% of the maximum power of the transmission with output power fluctuations of less than 1% and stability of several hours using a simple side-of-fringe stabilization of the piezo voltage, provided the temperatures of the three sections of the crystal are stabilized with mK precision by the PID controllers

The stability of red resonance when operating above 50mW of power is good enough so that the side temperatures can be slowly changed

with the Kerr-based piezo-controlled lock following the red resonance. The measurements shown in Fig. 7.5B and 7.5C were performed in the regime in which the slow change of the sides temperatures inside the cavity does not cause disturbance big enough to lose the lock. The scan of $T_D$ presented in the picture 7.5B is done with only minimal adjustment of the piezo because $T_D$ does not significantly affect the resonances $J_{\text{red}}$ and $J_{\text{blue}}$, therefore the curve we obtain should correspond to $J_{\text{phase}}$. Theoretical relative phase visibility VIS $= \frac{2r_2{}^2re^{-\alpha L}}{1+(r_2{}^2re^{-\alpha L})^2}$ yields 94%, which is with very good agreement with experimental result that gives 96% from the sinusoidal fit presented on Fig. 7.5B as a solid line.

Similarly, Fig. 7.5C, which shows a slow sweep of $T_S$ while red resonance is maintained by feedback to the piezo element, shows that there is sufficient pressure and $T_S$ temperature range that it is always possible to tune the cavity into blue resonance while maintaining red resonance. Equivalently, that the blue resonance factor $J_{\text{blue}}$ and the red resonance factor $J_{\text{red}}$ can be simultaneously maximized.

### 7.2.5 Power measurement

The dependence of the power of the second harmonic with respect to the pump power is presented in the Fig. 7.6, along with a quadratic fit to the data points below 50 mW of pump power, since in this regime the pump depletion effect is not yet significant. For each data point the piezo and the side temperatures were optimized to achieve maximum second harmonic power. The resulting low-power efficiency is $0.72/W$, while in the high-power regime when pump depletion comes into play the conversion efficiency yields 4.5%.

The black curve on the inset of Fig.7.6, represents the dependence of the generated SH power on the fundamental power with all three degrees of freedom and phase matching optimized, while the red curve shows the same relationship of SH power to input fundamental power,

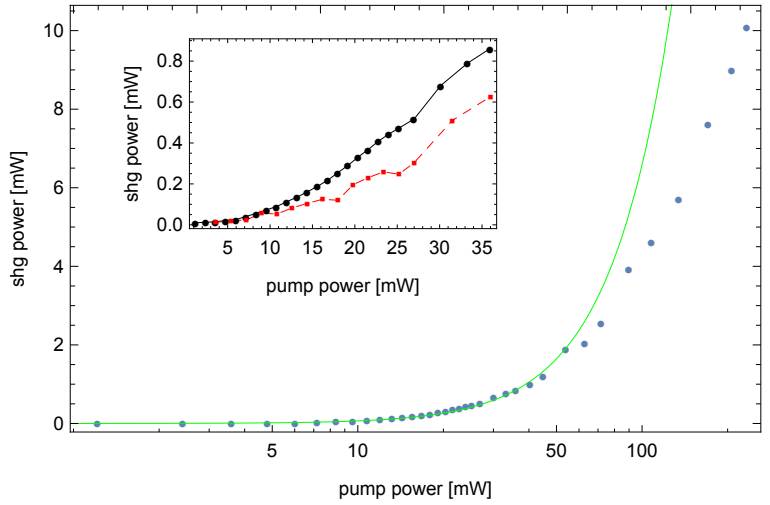


**Figure 7.6:** Blue points represent SH power measured as function of a pump power and green curve represents a cuadratic fit to the measurements below 50mW of pump power. The inset shows comparison between two cavity and phase matching optimization methods, the full independent optimization we propose (black curve), and optimization of 4 degrees of freedom with just crystal temperature (red curve).

with optimization of only the piezo voltage and the temperature of the entire crystal, thereby trying to achieve resonances at the cost of phase matching (a strategy similar to that employed by Yonezawa et. al [42]). This comparison shows that using full-crystal temperature as a degree of freedom to achieve cavity resonance(s) yields less conversion efficiency than does employing multiple independent temperature controls of the phase matching temperature. The exact advantage of full optimization depends on the crystal and vary according to the overlap of the phase matching curve with the cavity resonance(s) dependence on the crystal temperature [42].

## 7.3 Summary

We experimentally showed that the concept of a tunable second harmonic generation monolithic device described in Section 5.5 works in practice. Double resonance-enhanced SHG can be achieved for an arbitrary wavelength within the range allowed by the properties of the material via independent control of the temperature in three different sections of the crystal, as well as a pressure applied to the crystal using a piezoelectric actuator. We tested the performance of the monolith as a second harmonic generation device.

# Chapter 8

# The Photo-Kerr effect

In this chapter we describe a previously unreported optical nonlinearity and demonstrate its application in self-stabilization of the monolithic frequency converter. The new effect appears as an optical Kerr nonlinearity whose strength reflects the intra-cavity pump power over long time-scales, even though the Kerr effect it produces is fast. We find good agreement between a simple model of the new nonlinearity and observed nonlinear behavior. We show that this effect induces self-stabilization of the frequency converter, which remains in resonance despite pump frequency changes of multiple free spectral ranges.

Dispersive optical nonlinearities underlie a great variety of nonlinear phenomena and optical technologies, including optical memories [89, 90], optical solitons [91], squeezing of light [92], and entangled photon generation [93]. Two broad classes of refractive optical nonlinearities can be identified, fast nonlinearities in which the refractive index depends on the instantaneous intensity, and slow nonlinearities such as the photorefractive effect [94] in which the index depends on the history of intensity over a longer time. Here we observe a new kind of refractive nonlinearity in which the refractive index is linear in the instantaneous field, with a slope that reflects the intensity history of the material. We call this the *photo-Kerr effect* as it shares some characteristics of photorefractive effects. The effect combines both the strength of slow nonlinearities and speed of fast ones.

## 8.1 Experimental evidence

The experimental setup is shown in Fig. 8.1. The monolithic upconverter is pumped with up to 250 mW red light. The wavelength of the pump light is scanned through several cavity free spectral ranges while both pump and its second harmonic are separately collected at the output. As shown in Fig. 8.2, optical bistability is clearly seen when scanning the pump wavelength, evidenced by asymmetrical deformation of the cavity resonance, hysteresis, and abrupt transitions from high- to low-power stable points, with all these effects growing with pump power. Kerr bistability is well known to produce such effects, but what we observe here cannot be explained with a simple Kerr nonlinearity.

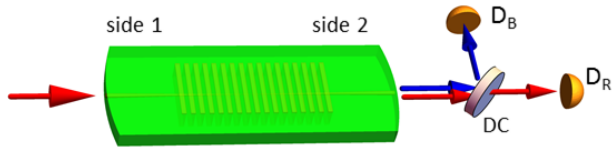


**Figure 8.1:** Experimental setup. The abbreviation DC means dichroic mirror, and detectors $D_R$ and $D_B$ collect 795 nm (red) and 397 nm (blue) light.

As shown in Fig. 8.3, the observed effects depend strongly on the speed of the scan, continuing to increase in prominence on long time-scales: We can deduce from Fig. 8.3 that the timescale of the resonance-dragging effect is $\sim 10$ s, much longer than any optical time-scale in the system. At the same time, the jumps from one stable point to another, visible in Fig. 8.3, appear to be very fast, suggesting the deformation of cavity spectrum depends on the instantaneous power in the cavity as well as its long-time average, indicating a refractive index depending in (at least) second order on the intensity.

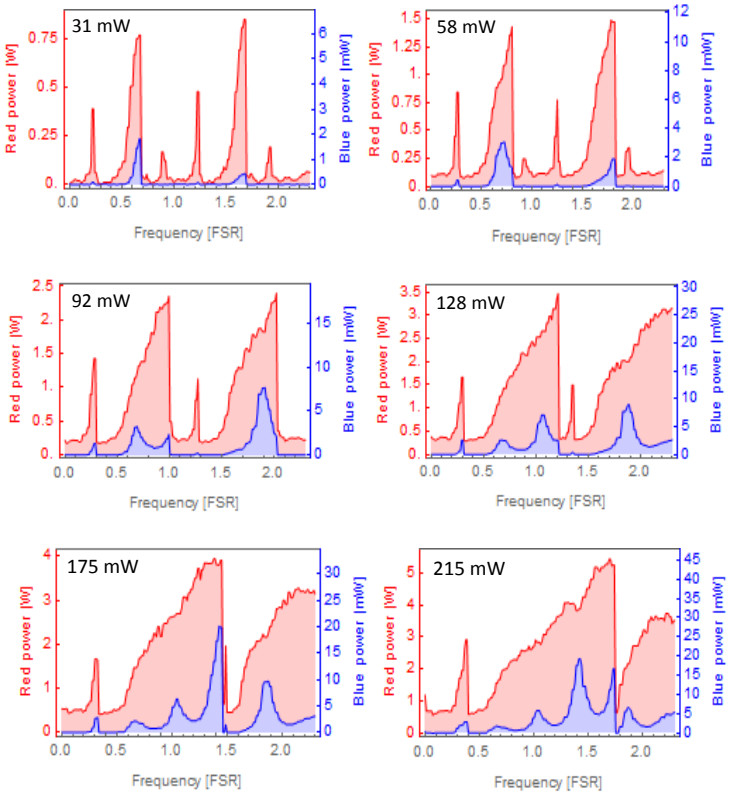


**Figure 8.2:** Red and blue curves show fundamental and second harmonic intracavity power vs pump laser frequency which is scanned over 2.5 cavity FSR for 795 nm . The scan speed is 10s per FSR, and each graph corresponds to a different pump power as indicated. Both red and blue intracavity powers are estimated from the respective output power and output coupler transmission values. The red output coupler is calibrated by measuring output at resonance for known input power and finesse.

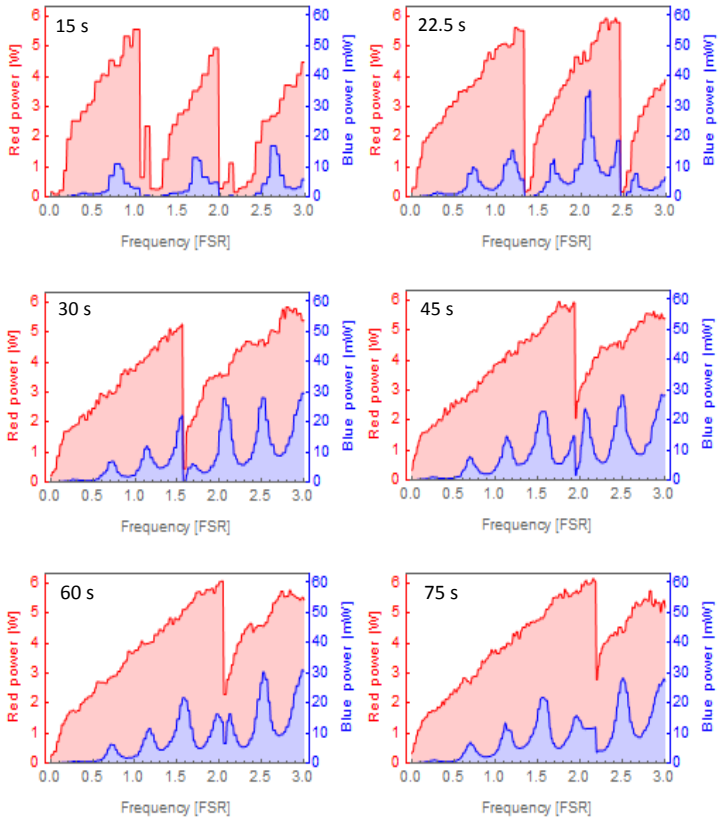


**Figure 8.3:** Red and blue curves show fundamental and second harmonic intracavity power vs pump laser frequency which is scanned over 3 cavity FSR for 795 nm . The pump power is set to 250mW, the graphs correpond to different scan speeds (a total duration of the 3 FSR scan is indicated on each graph). Both red and blue intracavity powers are estimated from the respective output power and output coupler transmission values.

### 8.1.1 Remarks on possible explanation

The effect does not appear to depend on the presence of the SH - the bistability occurs also when the SH is not generated, either because it is not resonant, the fundamental pump polarization is rotated, or because the poled section is far from the phase-matching temperature (we observe similar behaviour is the same for temperatures ranging from room to 55°C). The variations of the power of the SH light when pump wavelength is scanned depicted in Figs. 8.2 and 8.3 are determined by combination of pump power in the cavity, SH cavity resonance and interference between light generated forward and backward directions in the cavity, and appear not to be affected by the new nonlinear effect we observe in fundamental light.

While a thermal effect involving the temperature of the whole device could in principle operate on the $\sim 10$ s timescale, this explanation appears implausible: because RKTP is highly transparent at 795 nm , optical heating of the crystal is mostly due to absorption of the SH light, since the roundtrip loss is estimated to be 30%. Thermal changes in the cavity due to presence of fundamental light are hardly noticeable on the crystal temperature sensors, which is not the case with SH light. Moreover, thermooptical effect would affect SH light stronger than fundamental [95], and the photo-Kerr does not seem to deform the shape of SH resonances at all.

Although we rule out the blue-light-induced infra-red absorption (BLIIRA) as an explanation despite its long timescale [86] as the absorption alone cannot cause the cavity peak deformation we detect, it is possible that color-centers that underlie the BLIIRA are somehow related to the phenomenon.

The effect most closely resembles photorefractive effects, in which optically excited carriers become trapped for long times in impurity levels [96] and thereby contribute to the linear refractive index in function

of the intensity history of the material. Here, in contrast, what appears to depend on the intensity history is the nonlinear refractive index, or optical Kerr coefficient for the 795 nm wavelength.

The effect is present in all three RKTP monolithic cavities we tested (although in one of them it is $\sim 15\%$ weaker than in the other two), but we do not know whether this effect is characteristic for this particular material, or it is caused by some alteration of the fabrication or handling process of this particular batch of crystals.

### 8.1.2 Advantage for cavity stabilization

The observed nonlinearity has an evident benefit in maintaining resonance in the system: due to the strong nonlinearity, at higher powers the cavity line is pulled by more than a FSR. As a result, when the system jumps from a resonant stable point, it drops to another stable point that is also nearly resonant. As seen in Fig. 8.3, at the highest power and slowest scan, the system maintains $> 50\%$ of the intra-cavity pump power after such a jump and then rises toward full power. Resonant behavior can thus be maintained even without frequency stabilization. By setting the frequency to achieve a desired power (up to 95% of the maximum transmission), we have observed that the intra-cavity power is stable over hours, without any active frequency control. This moreover permits slow adjustment of the temperatures of the various crystal sections to achieve blue resonance.

## 8.2 Model

The bistability effects described above clearly show two time-scales, notable in the fast change from one stable state to another, and in the $\sim 10$ s accumulation time. We find the behaviour can be reproduced by a

model in which a fast Kerr nonlinearity is present, with a Kerr coefficient that grows at a rate proportional to the intra-cavity red power, and decays on a $\sim 10$ s time-scale.

### 8.2.1 Cavity roundtrip operator

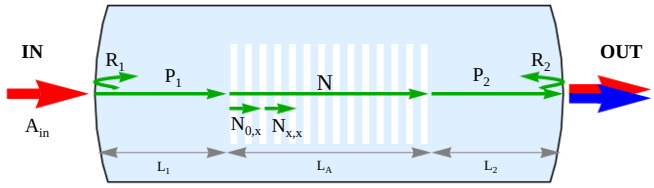


**Figure 8.4:** The lengths of the three sections of the crystal are denoted as $L_1$, $L_2$ and $L_A$. The propagation of the pump light with amplitude $A_{\text{in}}$ is described in terms of operators displayed in the figure.

To describe a frequency converter with refractive optical bistability, we must assume include second- and third-order nonlinear susceptibility, for the SHG and Kerr effects, respectively. In the resonator under consideration, only the middle section, where the fundamental and SH beams are focused, is periodically poled, and since the intensity is also highest in this region, we treat only the nonlinear effects for this part of the crystal. The material polarization is

$$P = \chi^{(1)}E + \chi^{(2)}E^2 + \chi^{(3)}E^3 \equiv \chi^{(1)}E + P_{NL} \tag{8.1}$$

We know from Maxwell equations that E and P evolve according to the wave equation [47] in the form of Eq. (2.2). For $X \in \{E, P, P_{NL}\}$, we can decompose it into a series $X(\vec{r},t) = \sum_m X_m(\vec{r})e^{i\omega_m t} + c.c.$, and Eq. 2.2 is then satisfied in particular for each frequency component

$$(\nabla^2 + \frac{n(\omega_m)^2}{c^2}\omega_m^2)E_m(\vec{r}) = -\frac{4\pi}{c^2}\omega_m^2 P_{NL,m}(\vec{r}) \tag{8.2}$$

where the refractive index $n(\omega_m) = \sqrt{1+4\pi\chi^{(1)}(\omega_m)} \approx 1+2\pi\chi^{(1)}(\omega_m)$. In what follows we suppress the frequency dependence of $\chi^{(i)}$ and assume that $\chi^{(3)}(\omega_2)$ is negligible. Let us consider the field in the following form

$$E(\vec{r}) = E_1(\vec{r})e^{i\omega_1 t} + E_2(\vec{r})e^{i\omega_2 t} + c.c. \tag{8.3}$$

where $\omega_2 = 2\omega_1$. From the experimental observations we expect that the following nonlinear polarization components are of greatest importance

$$P_{NL,1} = 2\chi^{(2)*}E_2E_1^* + \frac{3}{4}\chi^{(3)}E_1E_1^*E_1 \tag{8.4}$$

$$P_{NL,2} = \chi^{(2)}E_1^2 \tag{8.5}$$

We make the plane-wave approximation, and thus put $\nabla \to \partial_z$ in Eq. 8.2, and combining with Eqs. 8.4 and 8.5 we find the coupled wave equations

$$(\partial_z^2 + \frac{(n(\omega_1)+\kappa|E_1|^2)^2}{c^2}\omega_1^2)E_1 = -\frac{8\pi}{c^2}\omega_1^2\chi^{(2)*}E_2E_1^* \tag{8.6}$$

$$(\partial_z^2 + \frac{n(\omega_2)^2}{c^2}\omega_2^2)E_2 = -\frac{4\pi}{c^2}\omega_2^2\chi^{(2)}E_1^2 \tag{8.7}$$

where the Kerr coefficient is $\kappa = \frac{3\pi}{2}\chi^{(3)}$ and for clarity we have suppressed the $z$-dependence of $E_{1,2}(z)$. Now let us assume that $P_{NL}$ is small, so the solution is a plane wave in the form $E_m(z) = A_m(z)e^{ik_m z}$ where $k_m = n(\omega_m)\omega_m/c$. We also assume the envelope $A_m$ is slowly varying, i.e. $\partial_z^2 A_m << k_m\partial_z A_m$ and simplify $\partial_z^2 E_m$ as

$$\partial_z^2 E_m \to [2ik_m\partial_z A_m(z) - k_i^2 A_m(z)]e^{ik_m z} \tag{8.8}$$

In particular we have $k_1(z) = (n(\omega_1)+\kappa|A_1(z)|^2)\omega_1/c$ and we similarly

take $\partial_z e^{ik_1(z)z} \rightarrow ik_1(z)e^{ik_1(z)z}$ to obtain

$$\partial_z A_1(z) = i\frac{4\pi\chi^{(2)*}\omega_1^2}{k_1(z)c}A_2(z)A_1(z)^* e^{ik_2 z - 2ik_1(z)z} \tag{8.9}$$

$$\partial_z A_2(z) = i\frac{2\pi\chi^{(2)}\omega_2^2}{k_2 c}A_1(z)^2 e^{-ik_2 z + 2ik_1(z)z} \tag{8.10}$$

Now let's consider a slice of active section with small length $x$ (small enough to assume $k_1(z)$ constant), located at a distance $l$ from the beginning. The envelopes change as follows

$$A_1(l+x) = A_1(l) + i\frac{4\pi\chi^{(2)*}\omega_1^2}{k_1(l)c}A_2(l)A_1(l)^* J_{pm}(l,x)^* \tag{8.11}$$

$$A_2(l+x) = A_2(l)e^{-\alpha x} + i\frac{2\pi\chi^{(2)}\omega_2^2}{k_2 c}A_1(l)^2 J_{pm}(l,x) \tag{8.12}$$

where

$$J_{pm}(l,x) \equiv \int_l^{l+x} e^{-ik_2 z + 2ik_1(l)z} dz. \tag{8.13}$$

The fields $E_1$ and $E_2$ while passing through the slice acquire propagation phases of $\phi_x^{(\omega)} = (n(\omega_1, T_A) + \kappa|A_1(l)|^2)\omega_1 x/c$ and $\phi_x^{(\omega_2)} = n(\omega_2, T_A)\omega_2 x/c$, respectively. Refractive index $n(\omega, T)$ in addition to wavelength, depends also on the temperature of the active section of the crystal $T_A$ (the Sellmeier equation can be found in [95]). Additionally, SH light undergoes losses by a factor of $e^{-\alpha x}$ where $\alpha$ is the absorption coefficient. The operator that propagates the fields through the slice $N_{x,l}$ thus has the form

$$\begin{pmatrix} E_1 \\ E_2 \end{pmatrix} \xrightarrow{N_{x,l}} \begin{pmatrix} (E_1 + i\chi_{\text{eff}}^{(2)} E_1^* E_2 J_{pm}(l,x)^*)e^{i\phi_x^{(\omega)}} \\ (E_2 + i\chi_{\text{eff}}^{(2)} E_1^2 J_{pm}(l,x))e^{-\alpha x} e^{i\phi_x^{(\omega_2)}} \end{pmatrix} \tag{8.14}$$

For notational simplicity we define combining operators $S_1(S_2(A,B)) = S_1 \circ S_2(A,B)$. Then $N = N_{x,L_A - x} \circ \cdots \circ N_{x,x} \circ N_{x,0}$ is the operator that de-

scribes to fields passing through the whole active section of the length $L_A$.

The propagation through non-poled sections of the crystal of lengths $L_1$ and $L_2$ can be expressed as

$$\begin{pmatrix} E_1 \\ E_2 \end{pmatrix} \xrightarrow{P_j} \begin{pmatrix} E_1 e^{i\phi_j^{(\omega)}} \\ E_2 e^{-\alpha L_j} e^{i\phi_j^{(\omega_2)}} \end{pmatrix}, \tag{8.15}$$

where $\phi_j^{(\nu)} \equiv n(\nu, T_j)\nu L_j/c$ $\nu \in \{\omega_1, \omega_2\}$,for $j \in \{1,2\}$ and $P_i$ for $i = 1,2$ correspond to propagation through the cavity non-poled side sections 1 and 2 (see Fig. 5.1) maintained in their respective temperatures $T_1$ and $T_2$.

The reflection from the cavity sides is described using the operators

$$\begin{pmatrix} E_1 \\ E_2 \end{pmatrix} \xrightarrow{R_1} \begin{pmatrix} r_1 E_1 + t_1 A_{in} \\ E_2 \end{pmatrix} \tag{8.16}$$

and

$$\begin{pmatrix} E_1 \\ E_2 \end{pmatrix} \xrightarrow{R_2} \begin{pmatrix} r_2 E_1 \\ r E_2 \end{pmatrix} \tag{8.17}$$

where $r_1$ and $t_1$ are reflection and transmission coefficients for the fundamental light at side 1, and $r_2$ is the reflection at side 2. $r$ and $t$ describe reflection and transmission for the second harmonic at side 2 (side 1 is assumed completely reflective). The input fundamental pump amplitude is denoted as $A_{in}$.

The operator propagating the fields through the complete cavity roundtrip with Kerr coefficient $\kappa$ can be expressed as:

$$C_\kappa = P_1 \circ N_\kappa \circ P_2 \circ R_2 \circ P_2 \circ N_\kappa \circ P_1 \circ R_1 \tag{8.18}$$

### 8.2.2 Wavelength scan

We can find steady state fields $(E_1^{(s)}, E_2^{(s)})$ for the Kerr coefficient $\kappa$ after switching on the pump by propagating initial fields through $m$ roundtrips, where $m$ is chosen to be significantly larger than the cavity finesse, i.e.,

$$\begin{pmatrix} E_1^{(s)} \\ E_2^{(s)} \end{pmatrix} = C_\kappa^{\circ m} \begin{pmatrix} E_1^{(\mathrm{ini})} \\ E_2^{(\mathrm{ini})} \end{pmatrix} \tag{8.19}$$

where $C_\kappa^{\circ m}$ indicates $m$-fold composition of the operator $C_\kappa$. We note that this calculation method allows for hysteresis and multi-stability, because different initial conditions can lead to different steady-state conditions. The slow accumulation and decay of the Kerr coefficient $\kappa(t)$ is modeled by the

$$\partial_t \kappa = -\Gamma\kappa + f|E_1|^2 \tag{8.20}$$

where $\Gamma$ is the decay rate and $f$ is a coupling constant. Since the intracavity power is the variable accessible in the experiment, let us substitute $P_1 = \beta|E_1|^2$ where $\beta$ is a mode-shape dependent constant with the units of $\mathrm{Wm}^2/\mathrm{V}^2$. To simulate a scan, as in Figs. 8.2 and 8.3, we define a small time step $\tau$ and update $\kappa_j \equiv \kappa(j\tau)$ as

$$\kappa_{j+1} = M\kappa_j + FP_1^{(j)} \tag{8.21}$$

where $M = \exp[-\tau\Gamma]$, $F = \tau f \beta^{-1}$ and update the fields as

$$\begin{pmatrix} E_1^{(j+1)} \\ E_2^{(j+1)} \end{pmatrix} = C_{\kappa_j}^{\circ m} \begin{pmatrix} E_1^{(j)} \\ E_2^{(j)} \end{pmatrix}, \tag{8.22}$$

while the frequency of the input field changes with each step in time according to different scan speeds.

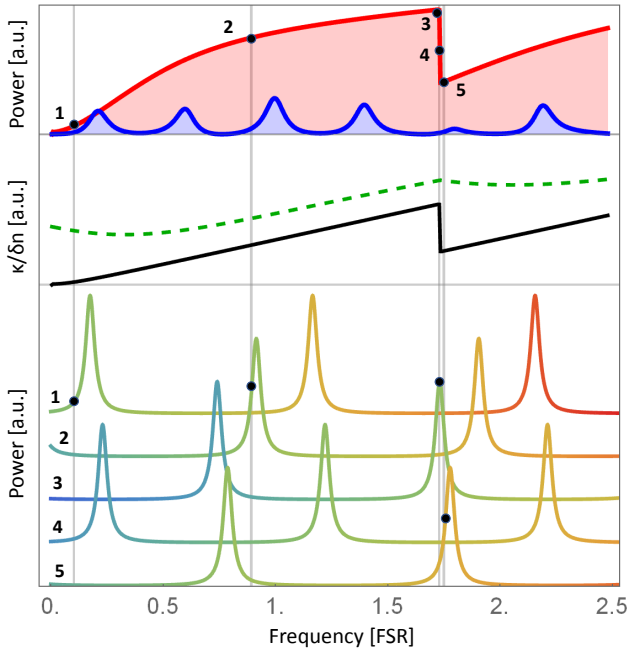


**Figure 8.5:** Model results illustrating cavity behaviour due to photo-Kerr effect. Upper part: Intracavity power of fundamental (red) and SH (blue) wavelengths as the fundamental pump wavelength is scanned. Conditions: scan rate 10 s per FSR, 250 mW input power, active section at the phase matching temperature. Middle part: Kerr coefficient $\kappa$ (green dashed curve) and refractive index change $\delta n = \kappa |A_1|^2$ (black curve). The cavity spectrum shift is proportional to $\delta n$. Lower part: cavity transmission for the fundamental at five representative points of the scan (marked in upper part): at point 1, the red field encounters a resonance. At point 2, the side-of-resonance condition is maintained by the combined effects of resonance and nonlinear refractive index. $\kappa$ accumulates, allowing the resonance to shift by more than one FSR. When the top of the resonance peak is reached (point 3), the resonance cannot shift anymore and the system becomes unstable. The power starts to drop and cavity resonance quickly retreats (point 4). Because the peak was shifted by more than one FSR, the system encounters another stable side-of-resonance condition (orange in the figure) as the nonlinear shift reduces (point five). As the scan proceeds the resonances once again shift and the process repeats.

### 8.2.3 Results

Model parameters that give reasonable agreement with observation are decay time $\Gamma^{-1} = 15.13$ s (corresponding to $M = 0.9967$), $\beta^{-1}F = 1.53 \times 10^{-8}$ W$^{-2}$, the initial Kerr coefficient multiplied by the inverse of geometry constant $\beta^{-1}\kappa_0 = 4 \times 10^{-6}$ W$^{-1}$, and time step $\tau = 50$ ms. The same $M$, $F$, $\kappa_0$ and $\tau$ parameters are used for results in Figures 8.5, 8.6 and 8.7.

Results from the model are shown in Figs. 8.5, 8.6 and 8.7. Fig. 8.5 illustrates the bistability mechanism and shows how the photo-Kerr effect produces self-stabilization near a cavity resonance, presenting results calculated at the phase-matching temperature. The dependence of cavity peak deformation on the power calculated from the theoretical model is presented in Fig. 8.6. For simplicity, the calculation is performed out of phase matching temperature and only the fundamental light power is shown in Figs. 8.6 and 8.7. Similar dependence on the scan speed can be found in the Fig. 8.7. The model reproduces qualitatively the behaviour of the cavity.

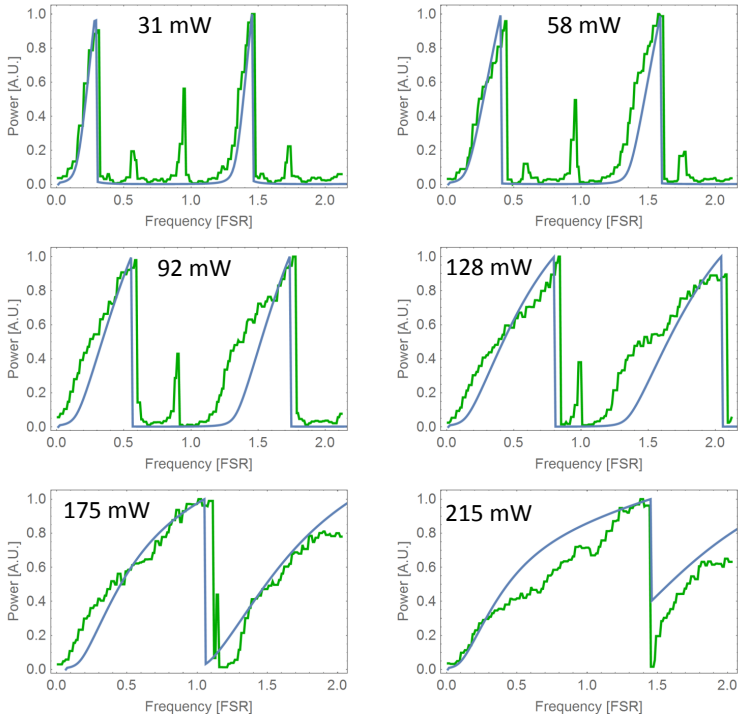


**Figure 8.6:** Blue curves represent cavity scans calculated from the model for powers 31 mW, 58 mW, 92 mW, 128 mW, 175 mW, 215 mW and 250 mW and scan speeds of 10 s per FSR, compared to corresponding experimental data (green).

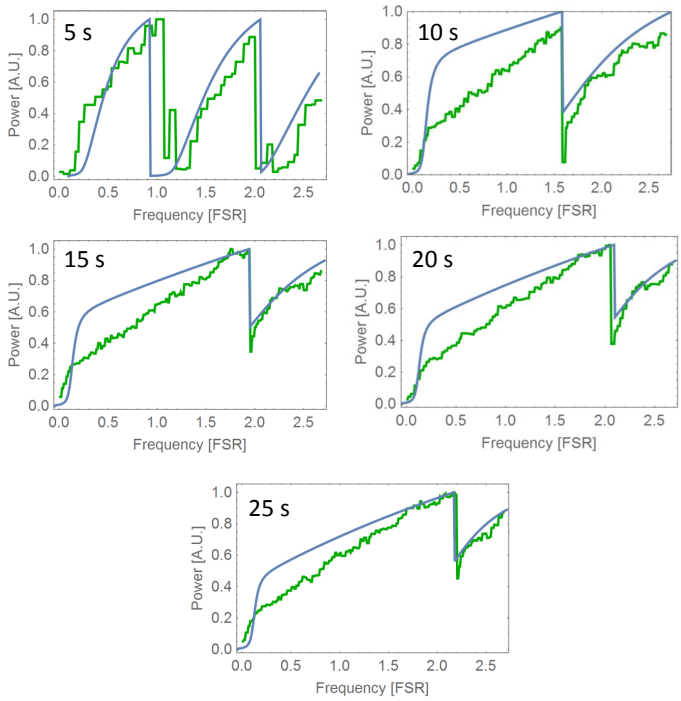


**Figure 8.7:** Blue curves represent cavity scans calculated from the model for scan speeds 5s, 10s, 15s, 20s and 25s per FSR for pump input power of 250mW, compared to corresponding experimental data (green).

## 8.3 Summary

We report on the observation of a previously unreported optical nonlinearity, in which the optical Kerr coefficient of a material strongly depends on the long-time average of the intensity in the material. The effect is clearly observed in our RKTP monolithic optical resonator, through dispersive optical bistability features that depend on long-time average of intra-cavity power. Modeling with nonlinear optical propagation equa-

tions well reproduces the observed behavior, and indicates that the new effect is far stronger than the ordinary Kerr effect in this scenario. At moderate input powers, the effect is sufficiently strong as to produce cavity mode-pulling that maintains the cavity near peak resonance even as the laser frequency changes by more than a FSR, greatly simplifying the stabilization of the cavity used as a frequency converter.

# Chapter 9

# Squeezing generation with the monolith

Optical parametric oscillators (OPOs) consisting of a second-order optical nonlinearity in a resonator, pumped below threshold by the second harmonic of the optical frequency to be squeezed, are a versatile source of squeezed light. Monolithic OPOs [42, 41], in which a single crystal acts as both nonlinear material and optical resonator, offer important advantages in stability, size, and efficiency. More fundamentally, the absence of air-crystal interfaces in these devices reduces losses and the potential for damage by strong pump intensities, key factors in the achievable squeezing. Indeed, monolithic devices hold records for optical squeezing up to 15 dB at wavelengths beyond 1 μm [36, 41, 6].

Realizing high squeezing levels at atomic wavelengths remains an open challenge. The relatively short wavelengths affect the technologies used for pumping and coating, the nonlinear material itself, and phase-matching. A promising new material is periodically-poled Rb-doped potassium titanyl phosphate (ppRKTP) which is only weakly absorptive at the second harmonic of the Rb $D_1$ and $D_2$ lines, and has poling advantages relative to undoped KTP [97]. Incorporation of this material in a monolithic OPO is promising for atomic quantum optics.

Prior work with monolithic KTP devices [42] demonstrated some of

these advantages but was not fully tunable. We have built and tested a doubly-resonant monolithic frequency converter in ppRKTP, with three thermal degrees of freedom enabling full tunability (see chapter 7). In this chapter we study the suitability of such devices for quantum optical applications. When used as a frequency doubler, the ppRKTP device showed an as-yet-unexplained optical nonlinearity producing strong optical bistability features described in chapter 8 . While advantageous for the tuning of the frequency doubler, the effect of this nonlinearity on quantum noise properties is unknown. Here we demonstrate quadrature squeezing from this device, confirming its suitability for quantum optical experiments.

## 9.1 Experimental setup

The experimental setup is shown schematically in Fig. 9.1. An external-cavity diode laser (ECDL) and tapered amplifier (TA) produce the fundamental light at 795nm. Most of the TA power is frequency doubled to 397 nm in order to generate a pump beam for the OPO, while a fraction is reserved for the local oscillator (LO) in homodyne detection and a seed beam to study the classical amplification properties of the device. A spectrum analyzer (SA) analyzes the homodyne detection output.

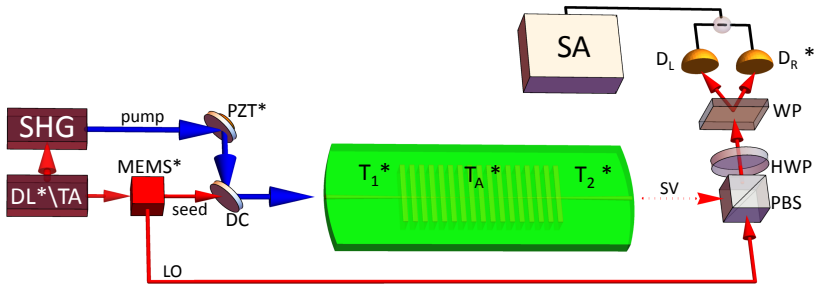


**Figure 9.1:** Experimental setup: DL - diode laser, TA - tapered amplifier, PZT - piezoelectric actuator, MEMS - micro-electromechanical system (switching input beam between two outputs), DC - dichroic mirror, PBS - polarizing beam splitter, HWP - half wave plate, WP - Wollaston Prism, $D_R$ and $D_L$ - balanced detector inputs, SA - spectrum analyzer, LO - local oscillator, SV - squeezed vacuum, $T_1$ and $T_2$ - temperatures of the non-poled sides of the crystal, $T_A$ - temperature of the active section of the crystal. Blue and red arrows represent 397 nm and 795 nm light respectively. Elements marked by an asterisk (*) are connected to a FPGA-based real-time control system.

Details of the doubly-resonant monolithic frequency converter and its tuning mechanisms are presented in chapter 7. Four degrees of freedom: the temperatures of three sections of the crystal and the pump laser frequency, are used to produce: phase matching, the fundamental and second-harmonic cavity resonance, and constructive interference between forward- and backward-emitted down-conversion light.

A microelectromechanical (MEMS) device switches fundamental power between the seed and LO beams, with only one powered at any given time. When the seed is on, the photocurrent of detector $D_R$ indicates the 795 nm transmission of the cavity, of interest for cavity stabilization and classical gain measurements. When the LO is on, the differential signal $D_R$-$D_L$ indicates one quadrature of the 795 nm field emitted by the cavity,

of interest for the squeezing measurements.

An FPGA-based controller sets the laser current, three thermal degrees of freedom of the monolithic cavity, pump beam phase (controlled by a piezo-electric actuator and with phase swept by $\sim 10\pi$ during each switching cycle) and the MEMS switch. The switching occurs at 10 Hz, with a duty cycle of 50%, and synchronized with the trigger of the sweep of the pump phase, which otherwise would inject noise through the gain's phase dependence. Due to the large resonance bandwidth of 250 MHz and high stability of the thermally-controlled cavity, a very simple feedback strategy suffices to maintain resonance. The FPGA notes the maximum and minimum transmission of the cavity during the pump phase sweep when the seed beam is on, and "walks" the ECDL frequency in steps of 2 MHz every 0.1 s, reversing direction of the steps whenever the detected maximum seed power drops by more than 0.5 % relative to the last step. While only the maximum is used for ensuring the fundamental beam resonance, both maximum and minimum are necessary to calculate the gain, which is controlled using thermal degrees of freedom of the cavity, without losing the lock, in order to optimize cavity parameters for maximum the gain at a given pump power.

Finally, the homodyne detection scheme is employed using local oscillator mode-matched to the seed beam exiting the cavity with at least 98% visibility of the interference obtained on one side of the balanced detector by scanning the local oscillator phase. The balanced detector itself is set to a gain of $10^4$ and bandwidth of 45 MHz (bandwidth refers to the differential output).

## 9.2 Gain

The first step in the OPO characterization was measuring the parametric gain, a phase sensitive amplification of the seed light, as a function of pump power. During this measurement the lock was continuous (seed always on), since there was no need for the local oscillator. The gain is obtained by measuring minimum power $P_{\text{min}}$ (seed deamplified by pump) and maximum power $P_{\text{max}}$ (seed amplified) of the seed exiting the locked cavity on the detector $D_R$ over one period of pump phase modulation (consisting of a few minima and maxima) using the following formula [98].

$$G = \frac{1}{4}\left(\sqrt{\frac{P_{\text{max}}}{P_{\text{min}}}} + 1\right)^2 \tag{9.1}$$

In order to measure maximum gain for a given pump power the central section of the crystal needs to be kept in phase matching temperature, whereas side sections $T_1$ and $T_2$ need to be adjusted in order to maximize first the blue resonance by $T_S = 0.5(T_1 + T_2)$ and then interference between forward and backward generated light by $T_D = T_1 - T_2$. The procedure is identical to that described in detail in chapter 7.

The measurements of the optimized gain for different powers are presented in the Figure 9.2. The expected relation depends on the OPO threshold pump power $P_{\text{th}}$ as follows

$$G(P) = (1 - \mu)^{-2} \tag{9.2}$$

where $\mu = \sqrt{P/P_{\text{th}}}$ and $P$ is pump power.

The data fit the gain vs power dependence for threshold power of 870mW (Fig. 9.2). The threshold is related to the single-pass conversion efficiency $d$ by the following formula (adapted from [98])

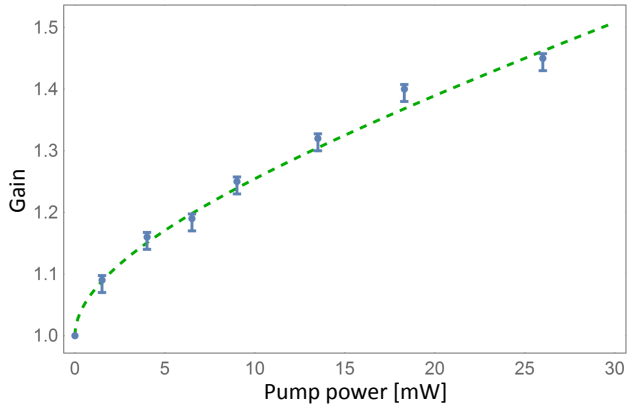


**Figure 9.2:** Points show measured gain as a function of pump power, optimized with crystal side temperatures $T_1$ and $T_2$. The green dashed line correponds to the fitted curve according to Eq. 9.2 with fitting parameter $P_{\text{th}} = 870$ mW.

$$P_{\text{th}} = \frac{T_{\text{P}}}{1 - T_{\text{P}}} \times \frac{T^2}{4bd} \tag{9.3}$$

where $T = 0.14$ is red output coupler transmission, $T_{\text{P}} = 0.31$ is pump input coupler transmission and double-pass enhancement factor is defined as $b = (2 - \frac{T_{\text{P}}}{2})^2$. The equation (9.3) assumes critical coupling of the blue cavity, which means that the roundtrip loss is equal to the input coupler transmission $T_{\text{P}}$, and negligible red intracavity losses. We find that single-pass efficiency $d$ yields 0.106% $\text{W}^{-1}\text{cm}^{-1}$. Originally, we expected the single-pass efficiency of 1% $\text{W}^{-1}\text{cm}^{-1}$, which would correspond to the OPO threshold of 90 mW.

## 9.3 Noise measurements

As shown in Fig 9.3, due to the shape of the detector noise spectrum the best central frequency for squeezing measurement was around 10 MHz.

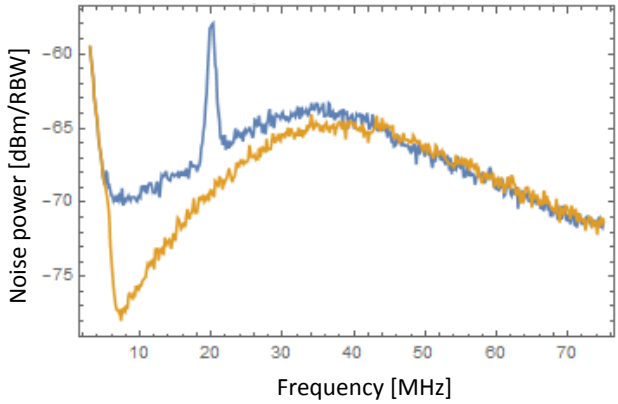


**Figure 9.3:** Noise power spectrum of the detection system. Orange curve shows measurement with the LO off, whereas blue curve represents noise spectrum with the LO on (peak at 20 MHz is due to LO modulation).

A pump-off noise measurement (meaning the difference current between $D_R$ and $D_L$) at the squeezing measurement conditions as a function of the local oscillator power allows us to determine the regime in which the detection system is shot noise limited, and find the electronic (independent of LO power) noise component, that will later be subtracted from the total noise in order to determine squeezing.

The result of this measurement is presented in the figure 9.4. The spectrum analyzer was set to zero span mode with center frequency of 10MHz, video bandwidth (VBW) of 100Hz and resolution bandwidth (RBW) of 3MHz. The data are fitted with a linear function with an offset that can be interpreted as electronic noise, found to be -70.75 dBm/3MHz. From the good agreement of the linear fit with the data we deduce that our system

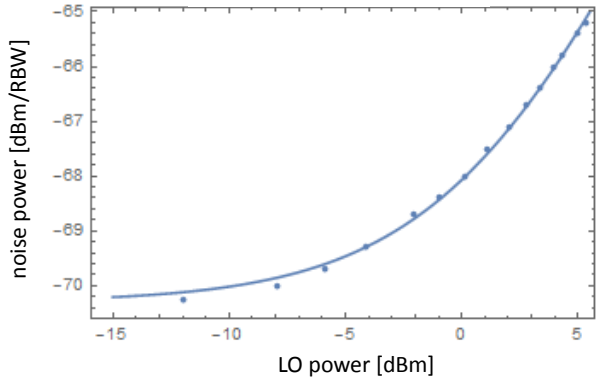


**Figure 9.4:** Points represent noise power as a function of a LO power at center frequency of 10MHz and RBW 3MHz. Solid line represents a fitted linear dependence with offset being equal to electronic noise of the system.

is shot noise limited above 2 mW of the LO power.

## 9.4 Squeezing measurements

Expected squeezing spectrum measured by the spectrum analyzer for $\mu << 1$ can be calculated as [98]

$$S_{-}(\Omega) = 1 - \frac{4\eta\mu}{(1+\mu)^2 + (\frac{\omega}{\Delta\omega})^2} \tag{9.4}$$

where $\omega$ is the detection frequency, $\Delta\omega$ denotes the cavity bandwidth and $\eta = \eta_{\text{det}}\eta_{\text{hom}}^2\eta_{\text{loss}}\eta_{\text{cav}}$ describes the combined effect of all the losses, including cavity escape efficiency $\eta_{\text{cav}}$, homodyne visibility $\eta_{\text{hom}}$, detector efficiency $\eta_{\text{det}}$, and other propagation losses in the squeezed beam $\eta_{\text{loss}}$. We realistically assume $\eta = 0.75$ due to 98% of homodyne visibility, 95% of propagation loss, the cavity escape efficiency of 95% and the

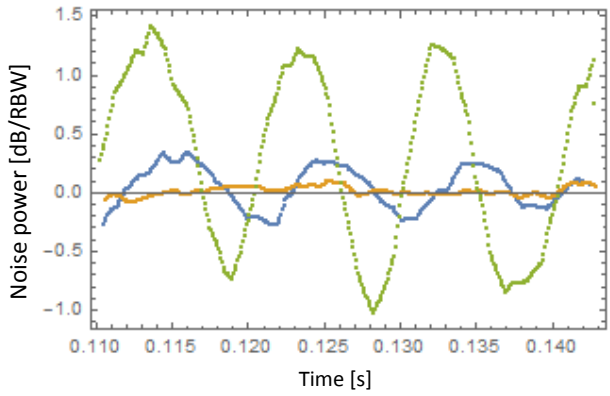


**Figure 9.5:** Green curve represents noise measured by the SA throughout the pump phase sweep with LO power of 2.5 mW and orange curve is the shot noise level (noise with pump switched off) without the absorber. Blue curve is the noise measurement during pump phase sweep with a 50% absorber inserted into the SV beam.

quantum efficiency of the detector (Thorlabs PDB450A with windows removed) given by the manufacturer which yields approximately 90%. At $\Omega \ll 1$, we expect close to 2dB squeezing and antisqueezing for pump power corresponding to the gain value of 1.4. For originally expected threshold of 90 mW we would expect 5.6 dB of squeezing.

We measure the squeezing and antisqueezing by modulating the phase between LO and pump beams, using the PZT (see Fig. 9.1) and recording on the spectrum analyzer how the noise varies with time. In order to directly measure the proportionality factor between the measurement with the spectrum analyzer and the squeezing spectrum as defined above we block the squeezed vacuum beam and record the squeezing spectrum for the vacuum state, which is equal to one (see orange curve in Fig. 9.5).

The data obtained yield around 1 dB of squeezing and 1.2 dB of antisqueezing at a frequencies small compared to the cavity bandwidth

(green curve in Fig. 9.5). Subtracting the electronic noise, this result corresponds to 1.6 dB of squeezing and 1.7 dB of antisqueezing.

Finally, an effect of inserting a 50% neutral density filter into the supposed squeezed vacuum light was recorded (see blue curve in Fig. 9.5), in order to make sure that generated state is a squeezed vacuum state, and not amplified and deamplified light leaking through the MEMS switch into the cavity. The insertion of the filter into the SV beam is expected to reduce the squeezing (and antisqueezing) level from 1 dB to 0.5 dB and without adding any offset in the noise vs time dependence. No significant offset noise level change is observed, and the drop in squeezing is slightly bigger than anticipated, possibly due to filter introducing small misalignment of mode-matched squeezed vacuum and LO beams.

## 9.5 Summary

We demonstrated 1.6 dB of squeezing from a doubly resonant monolithic cavity, which is an key step in developing an efficient, compact, portable and vibration-insensitive source of atom resonant squeezed light for various quantum optics experiments, with the use of two crystals (see Fig. 5.1), one for second harmonic generation, and the second one, a squeezer, pumped by the first one (so that only one fiber input for 795 nm pump light is necessary). We show that the third order photo-Kerr effect we observe in the ppRKTP does not cause significant increase in quantum noise, and therefore the material is suitable for generating squeezed light via spontaneous parametric downconversion.

# Chapter 10

# Conclusions and outlook

This thesis has described various results related to OPOs optimized for interaction with atoms. To begin with, we found the output of a multimode OPO for arbitrary subthreshold gain in the form of analytic Bogoliubov transformations. In contrast to previous works [48, 52], we avoided the quantum reservoir theory by posing the problem directly in the time domain. To study the time-domain structure, we calculated the second-order intensity correlation function. At higher gains the results show evidence of coherence increased beyond the cavity ring-down time due to stimulated spontaneous parametric down-conversion.

At low gain and high finesse we found that our model is well approximated by the calculation of [49], which yields a $G^{(2)}(T)$ with an envelope of a double exponential multiplied by a comb structure with a period equal to the cavity round trip time.

As we have shown experimentally in chapter 4, the comb structure in the $G^{(2)}(T)$ is absent if only a single mode of the OPO output is present, which can be achieved thanks to the atomic filter that transmits only the cavity mode containing frequency-degenerate photon pairs from a broadband sub-threshold OPO output. We demonstrated that the Faraday anomalous dispersion optical filter we employed preserves non-classical continuous-variable features, e.g. squeezing or non-gaussianity thanks to its high 70% peak transmission. The filter strongly suppresses all other

non-degenerate cavity modes, ensuring high spectral purity of 98% of the transmitted photon pairs which is an important feature for reliable discrete-variable detection and heralding applications.

The OPO filtering scheme described here served as one of the elements of the experiments performed by Federica Beduini. She demonstrated a new technique for the reconstruction of a temporal two-photon wavefunction of a squeezed vacuum state (degenerate mode of the OPO output), using the interference of the measured two-photon state with a coherent ancillary [99]. In contrast to common tomographic procedures [100], this method required only three measurement settings to obtain both the real and imaginary parts of the wave function. Another experiment performed with the help of the FADOF filtering technique demonstrated experimentally that photon pairs extracted at random from a polarization -squeezed beam are entangled if they arrive within the squeezing coherence time [19]. However, entanglement monogamy dilutes entanglement with increasing photon density which is reflected in the fact that, counterintuitively, increased squeezing corresponds to reduced bipartite entanglement.

The core of my work during the PhD studies was developing the monolithic doubly resonant OPO (or frequency converter). The proposed design has all the advantages of monolithic source (robustness, stability, low intracavity loss) and simultaneously allows to control multiple resonances for any emission wavelength within the range limited by the nonlinear material properties, increasing the efficiency of the frequency conversion (or lowering the threshold of the optical parametric oscillator).

The invention, although originally developed for quantum optical experiments involving interaction of squeezed light with a BEC, is in the process of being patented, as it has a potential to be commercially useful. For example, a monolithic second harmonic generator made of Stochio-

metric Lithium Tantalate and pumped by a semiconductor red diode laser could serve as cheap and easy to integrate source of coherent near UV light, which is difficult to access with standard laser technologies.

Industrial applications of such a UV source include flow cytometers, a technique used in hospitals and research centers for cell counting, drug detection and illness diagnosis. A number of useful and not replaceable probes have excitation peaks at wavelenghts below 350 nm and currently available laser sources at that wavelengths are either large and expensive (frequency tripled NdYAG or He-Cd laser) or do not provide enough power (LEDs). A multiply resonant monolithic frequency converter would be much cheaper, more compact alternative providing enough power for cuvette-based flow cytometry.

We have tested the monolithic cavity according to our design both as a frequency converter for second harmonic generation and as an OPO. Although in the present form the source does not generate enough squeezing to be applied to Faraday probing of the BEC, we have learned important facts that will serve as a base when developing the next generation of the monolith.

The geometric design will probably be kept unchanged since it is a tradeoff between limitations in polishing and optimal focusing conditions. However, in the next generation crystals the periodically poled section could be lengthened to 10 mm in order to increase the efficiency of the nonlinear interaction while still maintaining range of temperature tuning with side sections necessary to always achieve red resonance and constructive forward/backward interference condition. Pump resonance could either be dropped (only keeping the double pass configuration) or realized by adding an external mirror. The cost of having additional loss due to intracavity interface for the blue is negligible compared to crystal absorption, while the benefit of not using piezoelectric actuator as a fourth degree of freedom is crystal safety, as it sometimes causes the

crystals to break due to fatigue.

Finally, we reported what we believe to be a new nonlinear optical effect, observed in the recently-available material Rubidium-doped potassium titanyl phosphate (RKTP). The optical bistability effects in a monolithic cavity RKTP frequency converter show behavior combining the speed of electronic Kerr nonlinearities with the strength of photorefractive effects. At moderate input powers, the effect is sufficiently strong to produce cavity self-locking, i.e., it causes cavity mode-pulling that maintains the cavity peak near resonance even as the laser frequency changes by more than a free spectral range, greatly simplifying the stabilization of the monolithic cavity.

This "photo-Kerr effect" is interesting from the material science point of view, our observations are an invitation for further research as we do not know what causes it microscopically. It represents a fundamentally new entry in the toolkit of nonlinear optics, a fast, strong, optically-adjustable dispersive nonlinearity, which is of basic interest for optical physics, and has the potential to open new possibilities for optical technologies.

# Appendix A

# Fourier transforms for $\Gamma$ and $\Upsilon$

We first compute $\mathscr{F}[d(\omega)d(-\omega)](T)$, the Fourier transform of $d(\omega)d(-\omega)$, where $d$ is given in Eq. (3.15). We denote $x \equiv (1+r_1^2r_2^2e^{2r})/(2r_1r_2e^r)$ and $y \equiv (1+r_1^2r_2^2e^{-2r})/(2r_1r_2e^{-r})$. In the below-threshold regime we are considering, $r < r_{\text{th}} = -\log(r_1r_2)$ so that $d(\omega)$ is always finite. We find

$$d(\omega)d(-\omega) = \frac{1}{4r_1^2r_2^2}\frac{1}{x-\cos(\omega\tau)}\frac{1}{y-\cos(\omega\tau)} \tag{A.1}$$

Since $d(\omega)d(-\omega)$ is an even periodic function with a period of $2\pi/\tau$ we can write

$$d(\omega)d(-\omega) = \sum_{k=0}^{\infty} F(k)\cos(k\omega\tau) \tag{A.2}$$

Where

$$F(k) = \frac{2}{\pi}\int_0^{\pi} d(\omega)d(-\omega)\cos(k\omega\tau)d\omega \tag{A.3}$$

The Fourier transform is then the sum of Dirac delta functions:

$$\mathscr{F}[d(\omega)d(-\omega)](T) = \sum_{k=-\infty}^{\infty} F(|k|)\delta(T-k\tau) \tag{A.4}$$

The $F(k)$ can be expressed in terms of hypergeometric functions

$$\begin{aligned} F(k) &= \frac{2}{4r_1^2 r_2^2}\frac{1}{(x-y)(1+x)(1+y)} \\ &\times\left[(1+x)\frac{{}_3F_2\left(\{\frac{1}{2},1,1\},\{1-k,1+k\};\frac{2}{1+y}\right)}{\Gamma(1-k)\Gamma(1+k)}\right. \\ &\left.-(1+y)\frac{{}_3F_2\left(\{\frac{1}{2},1,1\},\{1-k,1+k\};\frac{2}{1+x}\right)}{\Gamma(1-k)\Gamma(1+k)}\right]. \end{aligned} \tag{A.5}$$

It follows immediately that the Fourier transform of $d(\omega)d(-\omega)e^{in\omega\tau}$ is

$$\mathscr{F}[d(\omega)d(-\omega)e^{in\omega\tau}](T) = \sum_{k=-\infty}^{\infty} F(|k|+n)\delta(T-k\tau). \tag{A.6}$$

Now in order to compute $\{\mathscr{F}[\Gamma](T)\}^2$ and $\{\mathscr{F}[\Upsilon](T)\}^2$, let us use the following trick. For a moment, let's assume that the bandwidth of the downconversion is finite, i.e. replace squeezing amplitude $r$ by a function $r\mathrm{rect}(\omega/\omega_{\mathrm{bw}})$ where

$$\mathrm{rect(x)} = \begin{cases} 1, & \text{if } |x| < 1/2 \\ 0, & \text{otherwise} \end{cases} \tag{A.7}$$

later we will apply to the final expressions the limit $\omega_{\mathrm{bw}} \to \infty$ returning to the situation with the infinite bandwidth. In that case the functions $\Gamma_{\mathrm{bw}}(\omega)$ and $\Upsilon_{\mathrm{bw}}(\omega)$ yield

$$\Gamma_{\mathrm{bw}}(\omega) = \mathrm{rect}(\omega/\omega_{\mathrm{bw}})\Gamma(\omega) \tag{A.8}$$

$$\Upsilon_{\mathrm{bw}}(\omega) = \mathrm{rect}(\omega/\omega_{\mathrm{bw}})\Upsilon(\omega) \tag{A.9}$$

Therefore, if we write $*$ for convolution we find

$$\{\mathscr{F}[\Upsilon_{\mathrm{bw}}](T)\} = \frac{\omega_{\mathrm{bw}}^2}{\sqrt{2\pi}}\{\mathscr{F}[\Upsilon](T)\} * \mathrm{sinc}\left(\frac{\mathrm{T}\omega_{\mathrm{bw}}}{2\pi}\right) \tag{A.10}$$

Knowing that

$$\{\mathscr{F}[\Upsilon](T)\} = t_1^2 \sinh(r)^2(1-r_1^2r_2^2)\sum_{k=-\infty}^{\infty}\delta(T-k\tau)F(|k|) \tag{A.11}$$

we arrive to

$$\begin{aligned}\{\mathscr{F}[\Upsilon_{\mathrm{bw}}](T)\}^2 &= t_1^4\sinh(r)^4(1-r_1^2r_2^2)^2 && \text{(A.12)}\\ &\quad\times\left[\sum_{k=-\infty}^{\infty}\mathrm{sinc}\left(\frac{(\mathrm{T}-\mathrm{k}\tau)\omega_{\mathrm{bw}}}{2\pi}\right)\mathrm{F}(|\mathrm{k}|)\right]^2. && \text{(A.13)}\end{aligned}$$

Now let's notice that for $k \neq l$

$$\lim_{\omega_{\mathrm{bw}}\to\infty}\mathrm{sinc}\left(\frac{(\mathrm{T}-\mathrm{k}\tau)\omega_{\mathrm{bw}}}{2\pi}\right)\mathrm{sinc}\left(\frac{(\mathrm{T}-\mathrm{l}\tau)\omega_{\mathrm{bw}}}{2\pi}\right) = 0 \tag{A.14}$$

and

$$\lim_{\omega_{\mathrm{bw}}\to\infty}\left[\mathrm{sinc}\left(\frac{\mathrm{T}\omega_{\mathrm{bw}}}{2\pi}\right)\right]^2 = \delta(T) \tag{A.15}$$

in the sense of a weak limit, i.e.

$$\lim_{\omega_{\mathrm{bw}}\to\infty}\int_{\infty}^{\infty}dT\,f(T)\left[\mathrm{sinc}\left(\frac{\mathrm{T}\omega_{\mathrm{bw}}}{2\pi}\right)\right]^2 = f(0) \tag{A.16}$$

for any continuous function $f$ with a compact support. It follows that:

$$\begin{aligned}\{\mathscr{F}[\Upsilon](T)\}^2 &= t_1^4\sinh(r)^4(1-r_1^2r_2^2)^2 && \text{(A.17)}\\ &\quad\times\sum_{k=-\infty}^{\infty}\delta(T-k\tau)F(|k|)^2 && \text{(A.18)}\end{aligned}$$

An analogous argument leads to

$$\begin{aligned}\{\mathscr{F}[\Gamma](T)\}^2 &= t_1^4 \sinh(r)^2 \sum_{k=-\infty}^{\infty} \delta(T-k\tau) \\ &\quad \times \left[(1+r_1^2 r_2^2)\cosh(r)F(|k|)\right. \\ &\quad \left. -r_1 r_2 F(|k|+1) - r_1 r_2 F(|k|-1)\right]^2 .\end{aligned} \tag{A.19}$$

# Appendix B

# Monolith temperature/piezo control

The key element of the system for controlling the monolith four degrees of freedom in both second harmonic generation and squeezing experiments was a reconfigurable NI PCI-7833R FPGA (Field Programmable Gate Array) board, drawn schematically in Fig. B.1. The dark blue part is used for controlling and optimizing degrees of freedom of a single cavity (it can be duplicated if a setup consists of two crystals), whereas the light blue part is used for driving the squeezing measurement experiment.

The temperature measurement of the three sections of the crystal was performed using a 8-channel data acquisition device (Measurement and Computing USB-TEMP), capable of measuring the resistance of 100 kΩ thermistors embedded in glass lower plate supporting the crystal (see Fig. 6.5 A and B) with 0.1 Ω precision.

The heating was implemented using digital outputs of the FPGA which generated a 100 Hz TTL signals with variable duty-cycles, converted to DC with the help of heating circuits (HC) in Fig. B.2, and passed through the thin ITO heating resistors (visible in Figures 6.6 and 6.5 A and B).

The heating circuits, as shown in Fig.B.2, consist of an operational amplifier, with a feed forward containing a low-pass filter with a time-constant of $\tau = 10$ ms. The relation between input and output voltage

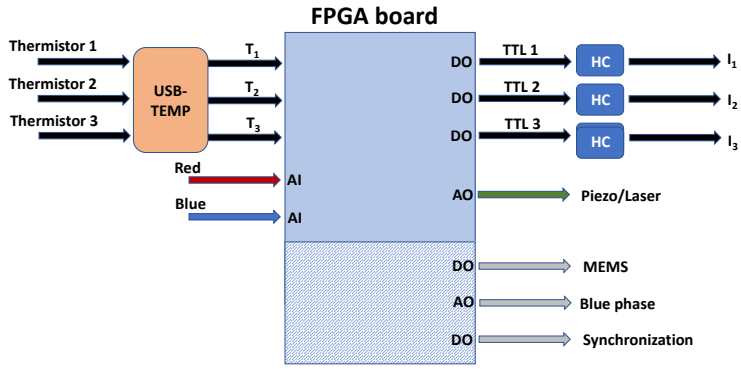


**Figure B.1:** The control system of the monolith. DO- digital output, AI - analog input, AO - analog output, HC - heating circuit, USB-TEMP - multichannel resistance measuring device.

of the HC at a frequency $\omega$ yields

$$V_{\mathrm{OUT}} = \frac{R_2}{R_1}\frac{1}{1+i\omega R_2 C}V_{\mathrm{IN}} \tag{B.1}$$

where the symbols of the elements are indicated in Fig. B.2. The purpose of the heating circuits was to provide strong constant heating current proportional to duty cycle of the TTL generated by the FPGA, thus avoiding generation of an RF signal. The duty-cycle was adjusted by the FPGA basing on the thermistor reading (with the use of a PID loop).

The fourth condition necessary to control the monolith was fulfilled either by adjusting the voltage fed to the piezoelectric actuator pressing the crystal or laser current determining its wavelength. In the SHG experiment, due to strong optical bistability, a simple PI loop maintained red cavity close to resonance (97% of power), using the red transmission signal ("Red" input in Fig. B.1). The generated blue power ("Blue" input) was used for finding the optimum temperature setpoints of side

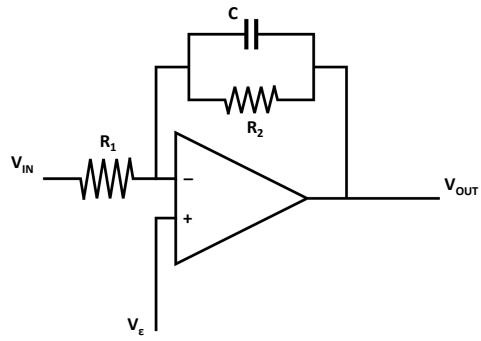


**Figure B.2:** Heating circuit made of resistors $R_1 = 1$ kΩ and $R_2 = 10$ kΩ and capacitor $C = 1$ μF.

temperatures $T_1$ and $T_2$ in order to maximize the blue resonance and interference condition. The program was capable of moving slowly the setpoints without losing the lock until the maximum blue emission was achieved.

During the squeezing experiment, when the monolith served as an OPO, the output "Piezo/Laser" controlled the laser current. The red resonance maintaining method using the cavity transmission amplified/deamplified by interaction with pump, is explained in chapter 9. In this experiment, the gain, calculated from the fluctuations of the "Red" signal, was used instead of "Blue" signal to determine the side temperatures' setpoints (controlling blue resonance and forward/backward interference). Additional outputs were employed for experiment synchronization, triggering the spectrum analyzer, applying phase ramp to the blue and controlling the MEMS that was switching the experiment between gain measurement and squeezing measurement periods.

# Appendix C

# Tapered Amplifier

In order to generate a high optical power at 795 nm, we implemented a tapered amplifier system based on the TA chip from Eagleyard Photonics, able to generate up to 2 W of power.

The system, shown in Fig. C.1 was modeled on a similar setup described in [101]. The seed light was continuous-wave 795nm distributed Bragg reflector (DBR) laser diode.

A key element of the system was a protective box containing the TA chip, two movable aspheric lenses, a temperature sensor and a Peltier element for cooling the chip. The box protected the chip from dust that could easily damage it and facilitated high current (up to 4 A) connection. The design was adapted from a design made by Cesar Cabrera.

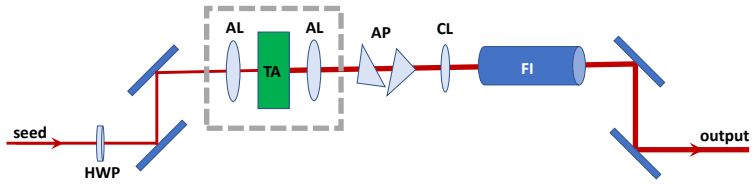


**Figure C.1:** Tapered amplifier setup. HWP- half-wave plate, AL - aspheric lens, AP - anamorphic prisms, FI - Faraday isolator

The output beam shaping was realized with a cylindrical lens astigmatism correction, and a anamorphic prism pair transform the beam from elliptic into circular in order to mode-match into the fiber. None of the elements are placed perpendicular to the beam before the Faraday isolator, as it the TA chip is very sensitive to backreflection. The overall useful power was 30%, due efficiency of the beam shaping elements, Faraday isolator and fiber coupling.

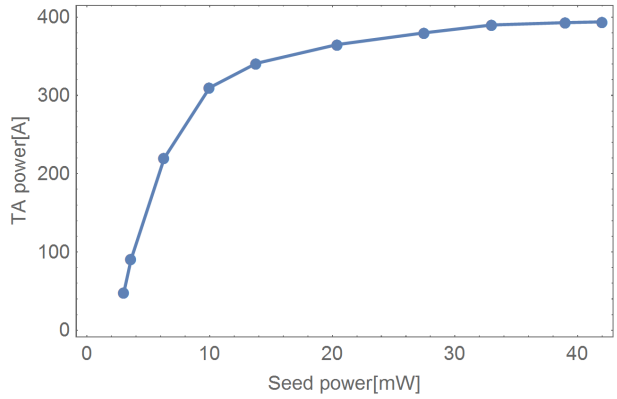


**Figure C.2:** Dependence of power generated by the TA on seed power for 1.5 A of the TA current.

Figure C.2 presents dependence of the generated TA power on the power of the seed for 1.5 A of TA current. A reasonable working point was found to be 10 mW of seed power, as for higher power the TA output saturates. Figure C.3 displays dependence of the generated power on the TA current for seed power of 10 mW.

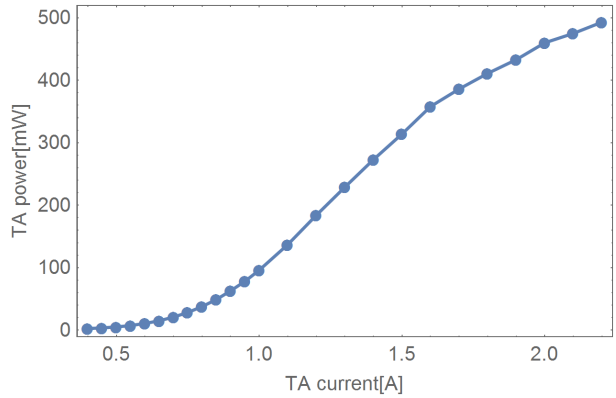


**Figure C.3:** Dependence of power generated by the TA on the current for 10 mW of seed power.

# Bibliography


[1] J. A. Giordmaine and R. C. Miller, "Tunable coherent parametric oscillation in linbo$_3$ at optical frequencies," Phys. Rev. Lett. **14**, 973–976 (1965).

[2] L.-A. Wu, H. J. Kimble, J. L. Hall, and H. Wu, "Generation of squeezed states by parametric down conversion," Phys. Rev. Lett. **57**, 2520–2523 (1986).

[3] F. Wolfgramm, A. Cerè, F. A. Beduini, A. Predojević, M. Koschorreck, and M. W. Mitchell, "Squeezed-light optical magnetometry," Phys. Rev. Lett. **105**, 053601 (2010).

[4] F. Wolfgramm, C. Vitelli, F. A. Beduini, N. Godbout, and M. W. Mitchell, "Entanglement-enhanced probing of a delicate material system," Nat Photon **7**, 28–32 (2013).

[5] V. G. Lucivero, R. Jiménez-Martínez, J. Kong, and M. W. Mitchell, "Squeezed-light spin noise spectroscopy," Physical Review A **93**, 053802 (2016).

[6] H. Vahlbruch, M. Mehmet, K. Danzmann, and R. Schnabel, "Detection of 15 db squeezed states of light and their application for the absolute calibration of photoelectric quantum efficiency," Phys. Rev. Lett. **117**, 110801 (2016).

[7] T. Eberle, S. Steinlechner, J. Bauchrowitz, V. Händchen, H. Vahlbruch, M. Mehmet, H. Müller-Ebhardt, and R. Schnabel, "Quantum enhancement of the zero-area sagnac interferometer topology for gravitational wave detection," Phys. Rev. Lett. **104**, 251102 (2010).

[8] J. C. Matthews, X.-Q. Zhou, H. Cable, P. J. Shadbolt, D. J. Saunders, G. A. Durkin, G. J. Pryde, and J. L. O'Brien, "Towards

practical quantum metrology with photon counting," npj Quantum Information **2**, 16023 (2016).

[9] M. D. Reid and P. D. Drummond, "Quantum correlations of phase in nondegenerate parametric oscillation," Phys. Rev. Lett. **60**, 2731–2733 (1988).

[10] Z. Y. Ou, S. F. Pereira, H. J. Kimble, and K. C. Peng, "Realization of the einstein-podolsky-rosen paradox for continuous variables," Phys. Rev. Lett. **68**, 3663–3666 (1992).

[11] F. Wolfgramm, A. Cerè, and M. W. Mitchell, "Noon states from cavity-enhanced down-conversion: high quality and super-resolution," J. Opt. Soc. Am. B **27**, A25–A29 (2010).

[12] E. Pomarico, B. Sanguinetti, N. Gisin, R. Thew, H. Zbinden, G. Schreiber, A. Thomas, and W. Sohler, "Waveguide-based opo source of entangled photon pairs," New Journal of Physics **11**, 113042 (2009).

[13] J. Fekete, D. Rieländer, M. Cristiani, and H. de Riedmatten, "Ultranarrow-band photon-pair source compatible with solid state quantum memories and telecommunication networks," Phys. Rev. Lett. **110**, 220502 (2013).

[14] F. A. Beduini and M. W. Mitchell, "Optical spin squeezing: Bright beams as high-flux entangled photon sources," Phys. Rev. Lett. **111**, 143601 (2013).

[15] I. Afek, O. Ambar, and Y. Silberberg, "High-noon states by mixing quantum and classical light," Science **328**, 879–881 (2010).

[16] M. W. Mitchell and F. A. Beduini, "Extreme spin squeezing for photons," New Journal of Physics **16**, 073027 (2014).

[17] T. Inagaki, K. Inaba, R. Hamerly, K. Inoue, Y. Yamamoto, and H. Takesue, "Large-scale ising spin network based on degenerate optical parametric oscillators," Nat Photon **10**, 415–419 (2016). Article.

[18] S. Braunstein and A. Pati, *Quantum Information with Continuous Variables* (Springer, 2010).

[19] F. A. Beduini, J. A. Zielińska, V. G. Lucivero, Y. A. de Icaza Astiz, and M. W. Mitchell, "Macroscopic quantum state analyzed particle by particle," Phys. Rev. Lett. **114**, 120402 (2015).

[20] A. Ourjoumtsev, R. Tualle-Brouri, J. Laurat, and P. Grangier, "Generating optical Schrödinger kittens for quantum information processing," Science **312**, 83–86 (2006).

[21] N. Bruno, A. Martin, P. Sekatski, N. Sangouard, R. T. Thew, and N. Gisin, "Displacement of entanglement back and forth between the micro and macro domains," Nat Phys **9**, 545–548 (2013).

[22] O. Morin, K. Huang, J. Liu, H. Le Jeannic, C. Fabre, and J. Laurat, "Remote creation of hybrid entanglement between particle-like and wave-like optical qubits," ArXiv e-prints (2013).

[23] U. L. Andersen and J. S. Neergaard-Nielsen, "Heralded generation of a micro-macro entangled state," Phys. Rev. A **88**, 022337 (2013).

[24] A. I. Lvovsky, R. Ghobadi, A. Chandra, A. S. Prasad, and C. Simon, "Observation of micro-macro entanglement of light," Nat Phys **9**, 541–544 (2013).

[25] H.-J. Briegel, W. Dür, J. I. Cirac, and P. Zoller, "Quantum repeaters: The role of imperfect local operations in quantum communication," Phys. Rev. Lett. **81**, 5932–5935 (1998).

[26] M. A. Rowe, D. Kielpinski, V. Meyer, C. A. Sackett, W. M. Itano, C. Monroe, and D. J. Wineland, "Experimental violation of a bell's inequality with efficient detection," Nature **409**, 791–794 (2001).

[27] M. Koschorreck, M. Napolitano, B. Dubost, and M. W. Mitchell, "Sub-projection-noise sensitivity in broadband atomic magnetometry," Phys. Rev. Lett. **104**, 093602 (2010).

[28] M. Koschorreck, M. Napolitano, B. Dubost, and M. W. Mitchell,

"Quantum nondemolition measurement of large-spin ensembles by dynamical decoupling," Phys. Rev. Lett. **105**, 093602 (2010).

[29] B. Dubost, M. Koschorreck, M. Napolitano, N. Behbood, R. J. Sewell, and M. W. Mitchell, "Efficient quantification of non-gaussian spin distributions," Phys. Rev. Lett. **108**, 183602 (2012).

[30] R. J. Sewell, M. Napolitano, N. Behbood, G. Colangelo, and M. W. Mitchell, "Certified quantum non-demolition measurement of a macroscopic material system," Nat Photon **7**, 517–520 (2013).

[31] S. L. Christensen, J.-B. Béguin, E. Bookjans, H. L. Sørensen, J. H. Müller, J. Appel, and E. S. Polzik, "Quantum interference of a single spin excitation with a macroscopic atomic ensemble," Phys. Rev. A **89**, 033801 (2014).

[32] F. Wolfgramm, X. Xing, A. Cerè, A. Predojević, A. M. Steinberg, and M. W. Mitchell, "Bright filter-free source of indistinguishable photon pairs," Opt. Express **16**, 18145–18151 (2008).

[33] A. Predojević, Z. Zhai, J. M. Caballero, and M. W. Mitchell, "Rubidium resonant squeezed light from a diode-pumped optical-parametric oscillator," Phys. Rev. A **78**, 063820 (2008).

[34] A. Predojevic, M. Koschorreck, M. Napolitano, F. Wolfgramm, B. Dubost, Y. de Icaza Astiz, N. Behbood, A. Cere, and M. W. Mitchell, "Quantum-enhanced measurements of atomic spin," in "2009 CONFERENCE ON LASERS AND ELECTRO-OPTICS AND QUANTUM ELECTRONICS AND LASER SCIENCE CONFERENCE (CLEO/QELS 2009), VOLS 1-5," (IEEE, 345 E 47TH ST, NEW YORK, NY 10017 USA, 2009), pp. 2194–2195. Conference on Lasers and Electro-Optics/Quantum Electronics and Laser Science Conference (CLEO/QELS 2009), Baltimore, MD, JUN 02-04, 2009.

[35] D. Rieländer, K. Kutluer, P. M. Ledingham, M. Gündoğan, J. Fekete, M. Mazzera, and H. de Riedmatten, "Quantum storage of heralded single photons in a praseodymium-doped crystal,"

Phys. Rev. Lett. **112**, 040504 (2014).

[36] M. Mehmet, S. Ast, T. Eberle, S. Steinlechner, H. Vahlbruch, and R. Schnabel, "Squeezed light at 1550 nm with a quantum noise reduction of 12.3 db," Opt. Express **19**, 25763–25772 (2011).

[37] J. S. Neergaard-Nielsen, B. M. Nielsen, C. Hettich, K. Mølmer, and E. S. Polzik, "Generation of a superposition of odd photon number states for quantum information networks," Phys. Rev. Lett. **97**, 083604 (2006).

[38] O. Morin, K. Huang, J. Liu, H. Le Jeannic, C. Fabre, and J. Laurat, "Remote creation of hybrid entanglement between particle-like and wave-like optical qubits," Nat Photon **8**, 570–574 (2014).

[39] H. Jeong, A. Zavatta, M. Kang, S.-W. Lee, L. S. Costanzo, S. Grandi, T. C. Ralph, and M. Bellini, "Generation of hybrid entanglement of light," Nat Photon **8**, 564–569 (2014).

[40] A. Lamas-Linares, J. C. Howell, and D. Bouwmeester, "Stimulated emission of polarization-entangled photons," Nature **412**, 887–890 (2001).

[41] S. Ast, M. Mehmet, and R. Schnabel, "High-bandwidth squeezed light at 1550 nm from a compact monolithic ppktp cavity," Opt. Express **21**, 13572–13579 (2013).

[42] H. Yonezawa, K. Nagashima, and A. Furusawa, "Generation of squeezed light with a monolithic optical parametric oscillator: Simultaneous achievement of phase matching and cavity resonance by temperature control," Opt. Express **18**, 20143–20150 (2010).

[43] J. A. Zielińska and M. W. Mitchell, "Theory of high gain cavity-enhanced spontaneous parametric down-conversion," Phys. Rev. A **90**, 063833 (2014).

[44] J. A. Zielińska, F. A. Beduini, V. G. Lucivero, and M. W. Mitchell, "Atomic filtering for hybrid continuous-variable/discrete-variable quantum optics," Opt. Express **22**, 25307–25317 (2014).

[45] K. Dechoum, P. D. Drummond, S. Chaturvedi, and M. D. Reid,

"Critical fluctuations and entanglement in the nondegenerate parametric oscillator," Phys. Rev. A **70**, 053807 (2004).

[46] C. Fabre, E. Giacobino, A. Heidmann, and S. Reynaud, "Noise characteristics of a non-degenerate optical parametric oscillator-application to quantum noise reduction," Journal de Physique **50**, 1209–1225 (1989).

[47] R. W. Boyd, *Nonlinear Optics, Third Edition* (Academic Press, 2008), 3rd ed.

[48] M. J. Collett and C. W. Gardiner, "Squeezing of intracavity and traveling-wave light fields produced in parametric amplification," Physical Review A **30**, 1386 (1984).

[49] Y. Lu and Z. Ou, "Optical parametric oscillator far below threshold: Experiment versus theory," Physical Review A **62**, 033804 (2000).

[50] Z. Y. Ou and Y. J. Lu, "Cavity enhanced spontaneous parametric down-conversion for the prolongation of correlation time between conjugate photons," Phys. Rev. Lett. **83**, 2556–2559 (1999).

[51] C. W. Gardiner and M. J. Collett, "Input and output in damped quantum systems: Quantum stochastic differential equations and the master equation," Phys. Rev. A **31**, 3761–3774 (1985).

[52] C. Gardiner and C. Savage, "A multimode quantum theory of a degenerate parametric amplifier in a cavity," Optics Communications **50**, 173 – 178 (1984).

[53] A. Predojević, Z. Zhai, J. M. Caballero, and M. W. Mitchell, "Rubidium resonant squeezed light from a diode-pumped optical-parametric oscillator," Phys. Rev. A **78**, 063820 (2008).

[54] Y. Jeronimo-Moreno, S. Rodriguez-Benavides, and A. B. U'Ren, "Theory of cavity-enhanced spontaneous parametric downconversion," Laser Physics **20**, 1221–1233 (2010).

[55] M. Patel, J. B. Altepeter, Y.-P. Huang, N. N. Oza, and P. Kumar,

"Independent telecom-fiber sources of quantum indistinguishable single photons," New Journal of Physics **16**, 043019 (2014).

[56] M. R. Sprague, P. S. Michelberger, T. F. M. Champion, D. G. England, J. Nunn, X. M. Jin, W. S. Kolthammer, A. Abdolvand, P. S. J. Russell, and I. A. Walmsley, "Broadband single-photon-level memory in a hollow-core photonic crystal fibre," Nat Photon **8**, 287–291 (2014).

[57] O. Morin, C. Fabre, and J. Laurat, "Experimentally accessing the optimal temporal mode of traveling quantum light states," Phys. Rev. Lett. **111**, 213602 (2013).

[58] J. A. Zielińska, F. A. Beduini, N. Godbout, and M. W. Mitchell, "Ultranarrow Faraday rotation filter at the Rb $D_1$ line," Opt. Lett. **37**, 524–526 (2012).

[59] F. Wolfgramm, Y. A. de Icaza Astiz, F. A. Beduini, A. Cerè, and M. W. Mitchell, "Atom-resonant heralded single photons by interaction-free measurement," Phys. Rev. Lett. **106**, 053602 (2011).

[60] P. Palittapongarnpim, A. MacRae, and A. I. Lvovsky, "A monolithic filter cavity for experiments in quantum optics," Review of Scientific Instruments **83**, 066101 (2012).

[61] W. Kiefer, R. Löw, J. Wrachtrup, and I. Gerhardt, "Na-faraday rotation filtering: the optimal point," Scientific reports **4** (2014).

[62] C. M. Caves, "Quantum-mechanical noise in an interferometer," Phys. Rev. D **23**, 1693–1708 (1981).

[63] M. Gajdacz, P. L. Pedersen, T. Mørch, A. J. Hilliard, J. Arlt, and J. F. Sherson, "Non-destructive faraday imaging of dynamically controlled ultracold atoms," Review of Scientific Instruments **84**, 083105 (2013).

[64] A. Smith, B. E. Anderson, S. Chaudhury, and P. S. Jessen, "Three-axis measurement and cancellation of background magnetic fields

to less than 50 $\mu$g in a cold atom experiment," Journal of Physics B: Atomic, Molecular and Optical Physics **44**, 205002 (2011).

[65] Y. Liu, S. Jung, S. E. Maxwell, L. D. Turner, E. Tiesinga, and P. D. Lett, "Quantum phase transitions and continuous observation of spinor dynamics in an antiferromagnetic condensate," Physical review letters **102**, 125301 (2009).

[66] F. Kaminski, N. S. Kampel, M. P. Steenstrup, A. Griesmaier, E. S. Polzik, and J. H. Müller, "In-situ dual-port polarization contrast imaging of faraday rotation in a high optical depth ultracold 87 rb atomic ensemble," The European Physical Journal D-Atomic, Molecular, Optical and Plasma Physics **66**, 1–8 (2012).

[67] M.-S. Chang, C. Hamley, M. Barrett, J. Sauer, K. Fortier, W. Zhang, L. You, and M. Chapman, "Observation of spinor dynamics in optically trapped rb 87 bose-einstein condensates," Physical review letters **92**, 140403 (2004).

[68] E. M. Bookjans, C. D. Hamley, and M. S. Chapman, "Strong quantum spin correlations observed in atomic spin mixing," Physical review letters **107**, 210406 (2011).

[69] Y. Kawaguchi, N. T. Phuc, and P. B. Blakie, "Finite-temperature phase diagram of a spin-1 bose gas," Phys. Rev. A **85**, 053611 (2012).

[70] R. J. Sewell, M. Koschorreck, M. Napolitano, B. Dubost, N. Behbood, and M. W. Mitchell, "Magnetic sensitivity beyond the projection noise limit by spin squeezing," Phys. Rev. Lett. **109**, 253605 (2012).

[71] S. de Echaniz, M. Koschorreck, M. Napolitano, M. Kubasik, and M. Mitchell, "Hamiltonian design in atom-light interactions with rubidium ensembles: A quantum-information toolbox," Physical Review A **77**, 032316 (2008).

[72] D. J. Wineland, J. J. Bollinger, W. M. Itano, and D. J. Heinzen,

"Squeezed atomic states and projection noise in spectroscopy," Phys. Rev. A **50**, 67–88 (1994).

[73] N. Korolkova, G. Leuchs, R. Loudon *et al.*, "Polarization squeezing and continuous-variable polarization entanglement," Physical Review A **65**, 052306 (2002).

[74] M. W. Mitchell and F. A. Beduini, "Extreme spin squeezing for photons," New Journal of Physics **16**, 073027 (2014).

[75] D. J. Wineland, J. J. Bollinger, W. M. Itano, F. L. Moore, and D. J. Heinzen, "Spin squeezing and reduced quantum noise in spectroscopy," Phys. Rev. A **46**, R6797–R6800 (1992).

[76] I. Breunig, B. Sturman, A. Bückle, C. S. Werner, and K. Buse, "Structure of pump resonances during optical parametric oscillation in whispering gallery resonators," Opt. Lett. **38**, 3316–3318 (2013).

[77] S. Ast, A. Samblowski, M. Mehmet, S. Steinlechner, T. Eberle, and R. Schnabel, "Continuous-wave nonclassical light with gigahertz squeezing bandwidth," Opt. Lett. **37**, 2367–2369 (2012).

[78] S. Ast, M. Mehmet, and R. Schnabel, "High-bandwidth squeezed light at 1550 nm from a compact monolithic ppktp cavity," Opt. Express **21**, 13572–13579 (2013).

[79] J. U. Fürst, D. V. Strekalov, D. Elser, A. Aiello, U. L. Andersen, C. Marquardt, and G. Leuchs, "Low-threshold optical parametric oscillations in a whispering gallery mode resonator," Phys. Rev. Lett. **105**, 263904 (2010).

[80] H. Vahlbruch, A. Khalaidovski, N. Lastzka, C. Gräf, K. Danzmann, and R. Schnabel, "The geo 600 squeezed light source," Classical and Quantum Gravity **27**, 084027 (2010).

[81] H. Vahlbruch, M. Mehmet, S. Chelkowski, B. Hage, A. Franzen, N. Lastzka, S. Goßler, K. Danzmann, and R. Schnabel, "Observation of squeezed light with 10-db quantum-noise reduction," Phys. Rev. Lett. **100**, 033602 (2008).

[82] G. D. Boyd and D. A. Kleinman, "Parametric interaction of focused gaussian light beams," Journal of Applied Physics **39**, 3597–3639 (1968).

[83] F. Steinlechner, P. Trojek, M. Jofre, H. Weier, D. Perez, T. Jennewein, R. Ursin, J. Rarity, M. W. Mitchell, J. P. Torres *et al.*, "A high-brightness source of polarization-entangled photons optimized for applications in free space," Optics express **20**, 9640–9649 (2012).

[84] A. Zukauskas, V. Pasiskevicius, and C. Canalias, "Second-harmonic generation in periodically poled bulk rb-doped ktiopo4 below 400 nm at high peak-intensities," Opt. Express **21**, 1395–1403 (2013).

[85] G. Lindgren, A. Zukauskas, V. Pasiskevicius, F. Laurell, and C. Canalias, "Studies of sub-millisecond domain dynamics in periodically poled rb-doped ktiopo4, using online in situ second harmonic generation," Opt. Express **23**, 20332–20339 (2015).

[86] S. Tjörnhammar, V. Maestroni, A. Zukauskas, T. K. Uždavinys, C. Canalias, F. Laurell, and V. Pasiskevicius, "Infrared absorption in ktp isomorphs induced with blue picosecond pulses," Opt. Mater. Express **5**, 2951–2963 (2015).

[87] V. Berger, "Second-harmonic generation in monolithic cavities," J. Opt. Soc. Am. B **14**, 1351–1360 (1997).

[88] W. Wiechmann, T. Fukui, H. Masuda, and S. Kubota, "Refractive-index temperature derivatives of potassium titanylphosphate," Optics Letters **18**, 1208–1210 (1993).

[89] D. A. Parthenopoulos and P. M. Rentzepis, "Three-dimensional optical storage memory," Science **245**, 843 (1989).

[90] F. T. S. Yu and S. Jutamulia, *Optical Signal Processing, Computing, and Neural Networks* (John Wiley & Sons, Inc., New York, NY, USA, 1992), 1st ed.

[91] G. P. Agrawal, *Nonlinear Fiber Optics* (Academic Press, 2013).

[92] S. Schmitt, J. Ficker, M. Wolff, F. König, A. Sizmann, and G. Leuchs, "Photon-number squeezed solitons from an asymmetric fiber-optic sagnac interferometer," Phys. Rev. Lett. **81**, 2446–2449 (1998).

[93] X. Li, P. L. Voss, J. E. Sharping, and P. Kumar, "Optical-fiber source of polarization-entangled photons in the 1550 nm telecom band," Phys. Rev. Lett. **94**, 053601 (2005).

[94] D. Nolte, *Photorefractive Effects and Materials*, Electronic Materials: Science & Technology (Springer US, 2013).

[95] K. Kato and E. Takaoka, "Sellmeier and thermo-optic dispersion formulas for ktp," Appl. Opt. **41**, 5040–5044 (2002).

[96] P. Günter and J. Huignard, *Photorefractive Materials and Their Applications 3: Applications* (Springer, 2007).

[97] C. Liljestrand, F. Laurell, and C. Canalias, "Periodic poling of Rb-doped $KTiOPO_4$ by coercive field engineering," Optics Express **24**, 14682–14689 (2016).

[98] A. Predojević, "Rubidium resonant squeezed light from a diode-pumped optical parametric oscillator," Ph.D. thesis, ICFO-Institut de Ciéncias Fótoniques and Departement de Física Aplicada y Simulación en Ciencias de Universidad Politécnica de Catalunya (2009).

[99] F. A. Beduini, J. A. Zielińska, V. G. Lucivero, Y. A. de Icaza Astiz, and M. W. Mitchell, "Interferometric measurement of the biphoton wave function," Physical review letters **113**, 183602 (2014).

[100] R. Adamson, L. Shalm, M. Mitchell, and A. Steinberg, "Multiparticle state tomography: Hidden differences," Physical review letters **98**, 043601 (2007).

[101] J. C. Kangara, A. J. Hachtel, M. C. Gillette, J. T. Barkeloo, E. R. Clements, S. Bali, B. E. Unks, N. A. Proite, D. D. Yavuz, P. J. Martin *et al.*, "Design and construction of cost-effective tapered

amplifier systems for laser cooling and trapping experiments," American Journal of Physics **82**, 805–817 (2014).